# Nanoorganization and device fabrication (carbon nanotubes) by vertical Porous Anodic Alumina Templates

Bernd Marquardt

ÉCOLE POLYTECHNIQUE

THÈSE

Présentée pour obtenir le grade de

DOCTEUR DE L'ECOLE POLYTECHNIQUE

Spécialité: Physique

par

Bernd MARQUARDT

# Nanoorganization and device fabrication (carbon nanotubes) by vertical Porous Anodic Alumina Templates

## Organisation nanométrique de composant (nanotubes de carbone) utilisant des membranes verticales d'alumine anodique poreuse

Soutenue le 17/12/2009 devant le jury constitué de :

| | |
|---|---|
| D. BUTTARD | **Rapporteur** |
| S. MATEFI-TEMPFLI | **Rapporteur** |
| C.-S. COJOCARU | **Examinateur** |
| P. LEGAGNEUX | **Examinateur** |
| V. MATHET | **Examinateur** |
| S. ROUSSET | **Examinateur, Président du jury** |
| M. CHATELET | **Directeur de Thèse** |

LABORATOIRE DE PHYSIQUE DES INTERFACES ET COUCHES MINCES, CNRS UMR 7647
ÉCOLE POLYTECHNIQUE

**Résumé:** Cette thèse est dédiée à l'étude des membranes verticales d'Alumine Anodique Poreuse (AAP) et leur application pour l'organisation nanométrique et la fabrication de composants. L'objectif principal a été de développer une méthode d'anodisation d'Al permettant une fabrication réproductible des AAPs qui rend possible la réalisation des nano-structures poreuses complexes et l'organisation de nano-matériaux. La fabrication des AAPs, et donc l'anodisation, a été étudiée profondément à partir de différents substrats sur lesquels une couche d'Al a été déposée au départ. Nous avons pu contrôler précisément la vitesse de fabrication d'AAP. Des AAPs ont été fabriquées utilisant de très forts acides à basse température, ce qui a permis à réaliser des diamètres de pores d'environ 4.2 nm et des densités de pores jusqu'à $7.2*10^{11}cm^{-2}$. En plus, une méthode unique a été développée pour le traitement de la couche barrière au fond des pores appliquant une décroissance exponentielle de la tension d'anodisation. Cela permet le contrôle et la variation de l'épaisseur de la couche barrière et, en même temps, le contrôle de l'uniformité et de la distribution de cette épaisseur. En se basant sur les résultats fondamentaux concernant la fabrication des AAPs, nous avons pu établir une technique d'électrodéposition dans des AAPs qui permet le dépôt de particules de Ni d'une taille variable (d'environ 10 nm à 2.5 µm) à différentes densités souhaitées dans une gamme de $2.3\ 10^9\ cm^{-2}$ to $7.1 \times 10^{10}\ cm^{-2}$ dans des AAPs avec un diamètre de pores de 40 nm. La croissance des NTCs a été étudiée dans des AAPs aussi bien que sur des surfaces structurées par des AAPs. La variabilité de la densité des particules de catalyseur implique la possibilité de la variation de la densité des NTC. Cela nous a permis la réalisation des échantillons d'émission de champ à partir des NTCs, avec lesquelles on a pu obtenir une émission de champ de 1 $mA/cm^2$. Qui plus est, nous avons démontré la faisabilité d'une structure multi-couche poreuse à partir d'une gravure anisotrope utilisant des AAPs comme masque de gravure. Cela pourrait permettre d'envisager de nouveaux composants "bottom-up" comme un transistor vertical à base des NTCs ou des nanofils de Si.

Mots Clés: membranes d'alumine anodique poreuse, NTC, anodisation, électrodéposition, masque de gravure, ICP

**Abstract:** This thesis is devoted to the study of vertical Pourous Anodic Alumina templates (PAA) and the application thereof for nanoorganization and device fabrication. Our principle objective was to develop an anodization method of Al that allows a reproducible fabrication of PAA offering the possibility to create complex porous nanostructures as well as the organization of nanomaterials. The PAA fabrication, i.e. the anodization process, has been studied in detail on various substrates on which initially an Al layer has been deposited. We have been able to control the fabrication rate of PAA precisely. PAAs have been fabricated using highly acidic anodization acids at low temperature, by which pore diameters down to 4.2 nm and pore densities up to $7.2*10^{11}cm^{-2}$ could be obtained. Further, we have developed a unique approach to control the barrier layer at the pore bottom of PAA applying an exponential anodization voltage decrease. This allows to vary and to control precisely the thickness of the barrier layer including the possibility to control the uniformity and distribution of the barrier layer thickness. Based on the fundamental control of PAA fabrication, we have been able to develop an electrodeposition technique inside PAA that allowed us to deposit Ni-particles of adjustable size (from about 10 nm to 2.5 µm) at predetermined deposition densities in the range of $2.3\ 10^9\ cm^{-2}$ to $7.1 \times 10^{10}\ cm^{-2}$ inside PAA with a pore diameter of 40 nm. The CNT growth was studied inside PAA and on PAA patterned surfaces. The variability of the deposited growth catalyst particles allowed us to vary the density of grown CNTs. This was the basis for the fabrication of CNT field emission samples, by which field emission of 1 $mA/cm^2$ has been realized. Last but not least, we have demonstrated that PAA can be used as etching mask for multilayer structures allowing to create nanoporous multilayers by anisotropic etching. This might open the way for new bottom-up devices like a vertical transistor based on CNTs or Si-nanowires.

Key-words: porous anodic alumina templates, CNT, anodization, electrodeposition, etching mask, ICP

## Remerciements

Je n'aurais jamais pu effectuer et finir ma thèse sans le support et l'aide de multiples personnes. D'une part, j'ai pu profiter de l'expérience scientifique du LPICM, notamment de l'équipe NANOMADE. D'autre part, et aussi important, j'ai eu la chance de travailler dans une ambiance chaleureuse et de vivre une « vie scientifique » au sein du laboratoire pendant ces années.
Je souhaite remercier vivement tous ceux qui ont contribué à cela.

Tout d'abord, je tiens à remercier Stéfan Matéfi-Tempfli et Denis Buttard d'avoir accepter d'être rapporteur et d'avoir investi leur temps. De même, je remercie Véronique Mathet, Pierre Legagneux et Costel Cojocaru pour avoir participé au jury de ma thèse et Sophie Rousset pour avoir été la présidente du jury de ma thèse.

Je voudrais remercier Bernard Drévillon de m'avoir accepté au sein de son laboratoire et pour tout son support, sa motivation et son bonheur.

Je tiens à remercier Didier Pribat pour m'avoir intégré dans son équipe NANOMADE et pour toutes les discussions et projets que j'ai pu avoir avec lui. J'ai compris qu'il m'a appris des tas de choses, et je le remercie vivement pour sa bonne foi et pour l'énergie qu'il a transférée.

Je remercie Marc Châtelet pour avoir été mon directeur de thèse et pour tout son support. Il a toujours été à l'écoute de tous mes problèmes et il était toujours prêt à investir son temps pour trouver une solution. Je ne sais vraiment pas comment j'aurais pu effectuer ma thèse sans son support et son aide. Juste pour donner un exemple: comment aurais-je pu trouver un appartement sans avoir Marc comme garant français ? Honnêtement, son caractère amical et son bonheur me manqueraient.

Je remercie Costel Cojocaru pour tous ses conseils et ses explications. Il m'a familiarisé avec le monde des nanotubes et nanofils, notamment avec la croissance de ces nanoéléments, et il était toujours prêt à investir son temps.

Je tiens à remercier Laurence Corbel et Chantal Geneste pour leur aide. Sans ce duo, je n'aurais jamais pu récupérer mon badge, passer des commandes et aller aux conférences. Des choses qui me semblaient compliquées devenaient simples grâce à leur support.

Un grand merci à Leo Caristan, Gary Rose, Eric Paillassa et Frédéric Liège pour leur support et leur aide. Leo, qui m'a aidé à résoudre de multiples problèmes techniques et qui a rendu possible la construction de porte-échantillons, Gary, qui a passer son temps pour la préparation de logiciels, Eric et Frédéric pour toute leur aide concernant des problèmes de réseau et d'ordinateurs.

Je remercie à tous mes collègues avec lesquelles j'ai pu travailler pendant ma thèse. Laurent Eude, Gowtham et Hee Jin Jeong, qui ont créé une ambiance chaleureuse dès mon entrée dans l'équipe et avec lesquels j'ai pu discuter amicalement et profondément. De tels collègues, chacun un vrai type, donnent des taches de couleur au travail quotidien, sans parler des moments à Fréjus, Bordeaux et en Corée que j'ai pu partager avec Laurent ! Je remercie Kihwan Kim, Emmanuel Lefeuvre, Yi Yin Yu et Geunsang Cho pour leur grande aide et leur sympathie. Laurent Baraton et Changseok Lee qui ont contribué à une ambiance sympathique. Anh Quoc LeQuang pour les discussions vives et pour son expérience qu'il a partagée. Mes combattants doctorants Gaëlle Lehoucq, Laurent Kroely, Oumkelthoum Mint Moustapha, Rosa Antonelli et Anirban Dhar avec lesquels j'ai pu m'échanger sur des problèmes divers. Sung Hoon Lim, Amaël Caillard, Arnaud-Julien Guilley, Erik Johnson, Marc Chaigneau, Pavel Bulkin, Tatjana Novikova, Laurent Philippe, Jean-Eric Bourrée, Yvan Bonnassieux, Pere Roca i Cabarrocas pour leur sympathie, présence, aide et bonheur. Je tiens à remercier particulièrement Jean-Eric qui était présent dans un « cas d'urgence » pour ne pas me laisser travailler seul. Ce sont des choses qu'on n'oublie jamais.

Pendant ma thèse, j'ai eu la chance de pouvoir travailler en collaboration, entre outre, avec le LSI, l'IEF et Thales.
Je tiens à remercier Travis Wade du LSI pour son aide et pour le temps que j'ai pu passer avec lui. J'ai toujours apprécié son style de travail, et ça me faisait plaisir de travailler avec lui.

Je remercie Véronique Mathet, José Palomo, David Bouville, Cédric Villebasse et toute l'équipe du IEF pour leur support et leurs explications.

Je remercie vivement Pierre Legagneux et son équipe pour le support, les explications et l'équipement que j'ai pu utiliser à Thales. J'ai toujours senti une amicalité et une ambiance particulièrement chaleureuse pendant mes « séjours » à Thales. Pour cela, je voudrais remercier Gaëlle Lehoucq, Paolo Bondavalli, Pierrick Guiset, Nicolas Lesech, Laurent Gangloff et Stéphane Xavier. Quant à Stéphane, je tiens à le remercier tout particulièrement. Son aide m'a accompagné pendant toute ma thèse, et je ne peux pas compter les heures qu'il a passé en salle blanche pour moi. Sa gentillesse, la perfection de son travail et son amitié étaient géniales. De même, je remercie Didier Thenot pour son aide. J'ai bien apprécié le support de Didier, qui était toujours prêt à dépanner l'ICP et à discuter sur des effets bizarres de gravure.

# Contents

# Introduction

For the application of nanomaterials in industrial device fabrications, a very important step is the cost effective ordered arrangement of nanomaterials which allows an easy handling of these materials in industrial processes, like contacting or stable positioning. Templates with an ordered arrangement of nanopores are of strong interest for the device fabrication in the nanotechnology since they can be used as a support for nanomaterials [1] like carbon nanotubes (CNTs) or nanowires, which are promising materials for nanodevice applications.

Porous Anodic Alumina (PAA) templates offer a wide range of interesting properties in this respect. PAA templates with pores arranged in a perfect hexagonal order and with adjustable pore diameter, pore density, thickness and thus aspect ratio can be achieved by a simple anodization process of an aluminium sheet in acid. These main parameters of PAA templates can be varied in a wide range by only changing the anodization conditions of the aluminium, like the anodization acid, the anodization voltage, the anodization duration and the acid temperature.

The possibility of an easy variation of the main template parameters goes along with low costs for both the anodization process and the basic material, aluminium. Besides, as aluminium is a well known material in the semiconductor industry, PAA membranes can be integrated in common production processes, and the surface area of PAA templates can be adapted as one wants: by keeping the anodization current density and the anodization voltage constant, in principle the anodization can be carried out on any desired aluminium surface.

The obvious application potential of PAA, of course, has led to an intensive research activity on PAA during the last decade. With improved control of the PAA fabrication, the interest in applications of PAA concerning the organization of nanoelements and the realization of nanodevices was sparked. In 2000 [2], a homogenous electrodeposition of Ni nanowires has been demonstrated for the first time, and recently, electrodeposition of various nanowires [3,4,5,6] and nanotubes [7] has been demonstrated; this PAA based nanowire growth has been shown to be especially interesting for magnetic and electronic measurements [8,9] and as well has been used for complex nanoarchitectures on electrodes [10]. Besides, PAA membranes have been also used as templates for CVD growth of carbon nanotubes (CNTs) [11] and silicon nanowires (SiNWs) [12]: in 2006, the first single wall CNTs

(SWCNTs) have been grown in PAA membranes [13], and sophisticated contacting methods [14,15] and CNT junctions [16] have been realized. The template based CNT and SiNW growth has been applied for a wide range of devices [17] and transport measurements [18,19]: this is proving that this PAA technique is promising for future nanotechnology devices.

Apart from the organization of nanomaterials by growth or deposition inside PAA, PAA membranes exhibit also interesting properties for the structuring of surfaces up to the use as etching mask [20,21]. The use of PAA as etching mask might replace the very cost intensive high resolution lithography steps.

Still, a variety of other fields in which the use of PAA offers interesting possibilities could be mentioned, like e.g. the use for like filtration or biofunctionalization [22].

However, although already many different applications of PAA have been demonstrated, still the fabrication process of PAA and the further processing steps must be improved before PAA can be used for a reliable fabrication of nanodevices and thus be applied by the semiconductor industry. Since the anodization itself is a complicated physical-chemical process which depends on many external factors, the know-how about the control of these factors is basically important for any further application of PAA. In addition, the huge variety of possible applications of PAA make it necessary to observe in detail the feasibility of each following processing step and thus to be able to focus on the most promising pathways in future device development.

In this work, we therefore, in a first step, investigated in detail the formation process of PAA in respect to the fabrication rate, the order and a possible pre-treatment of PAA before a subsequent use in an application. In addition, we studied the conditions for the fabrication of very small pores, which are of special interest for nanodevice applications. This investigation is described in chapter I.

Based on the results obtained in chapter I, we investigated possible further processing steps after the anodization in respect to future device fabrications.

In chapter II, we investigated the electrodeposition inside PAA. Namely the control of the uniformity of the electrodeposition and the precise control of the amount of deposited material has been the subject of the investigations of chapter II, always in respect to possible further applications.

In chapter III, the CNT growth on PAA fabricated with the fundamental understanding of the previous chapters has been studied, including the field emission measurements of PAA patterned CNTs.

In chapter IV, the use of PAA as etching mask has been analyzed. In this chapter, we show the feasibility of etching processes via a PAA mask and develop the fabrication process of a porous multilayer structure.

# Chapter I

# Porous Anodic Alumina Templates (PAA)

# I. Porous Anodic Alumina Templates (PAA)

## I.1 Introduction

PAA has been studied over more than a century. In 1970, O'Sullivan and Wood [23] made an important step towards the understanding of the fabrication process of PAA during the anodization, describing in detail the mechanism of PAA formation.
Masuda and co-workers achieved a real breakthrough for the use of PAA in nanotechnology applications, as, in 1995, they invented the two step anodization process for the PAA fabrication which leads to a perfectly ordered porous structure with a hexagonal pore lattice and perfectly parallel, vertical pores [24].
Since, there has been a huge progress in the control of the fabrication of PAA. In 1998, Li et al. demonstrated perfectly ordered PAA membranes with interpore distances from 50 nm to 420 nm, which corresponds to pore diameters of about 25 nm and 210 nm, respectively [25]. Recently, PAA structures with pore diameters from 7 nm to over 300 nm have been demonstrated [26].

At the same time, the investigations on PAA membranes have shown the high compatibility of PAA with future nanodevices. However, until today, PAA has been used essentially for fundamental research applications and the reproducibility of PAA and the resulting devices still have to be improved. For that purpose, it is important to get a very good understanding of the fabrication process of PAA, as, for further reliable device applications, the fabrication rate, the order and other main parameters of PAA, like the barrier layer at the bottom of the pores in PAA, must be perfectly controlled. This investigation of PAA is presented in the following of chapter I and thus presents the basis of the other chapters, as it provides the fundamental understanding and control of PAA fabrication.

# I.2 The formation process of PAA

## I.2.1 The anodization process of aluminium

Aluminium, as all other metals except gold, reacts at room temperature with oxygen and forms a metal oxide, which is energetically favourable, as can be quantified by the Gibb's free energy change (Δ G):

$4\ Al + 3\ O_2 \rightarrow 2\ Al_2O_3$ : Δ G = -1582 kJ/mol

Generally, metals thus form a metal oxide on the surface which, in most of the cases and also for alumina, itself is inert to oxygen and therefore protects the metal from further oxidation.

Aluminium shows an especially high affinity for oxygen, and the aluminium oxide formed at the aluminium surface exhibits very high corrosion and electrical resistance. Thus, in general, the oxidation of aluminium is stopped after the formation of a very thin oxide layer with thicknesses in the order of some nm, depending on the oxidation potential and temperature of the environment.

In an anodization process, a positive potential is applied on the Al (by regulating either the applied voltage or the effective current through the Al), so that an electric field is established which assists the migration of oxygen ions or oxidizing ions through the established metal oxide surface layer and thus increases the thickness of the aluminium oxide. Generally, anodization processes are realized in electromechanical cells in aqueous environment, in which the aluminium is set as an anode and a highly inert counter electrode, like gold, platinum or graphite, is set as a cathode. This leads mainly to the following reaction at the Al surface:

$$2Al^{3+}+6OH^{-}\rightarrow Al_2O_3+3H_2O$$

with the following basic reactions at the two electrodes:

$6H_2O+6e^{-}\rightarrow 3H_2+6OH^{-}$ (at the cathode)

$2Al\rightarrow 2Al^{3+}+6e^{-}$ (at the anode)

As it can clearly be seen by the reaction, the oxide layer $Al_2O_3$ is formed only if Al is in contact to the oxidizing ions, i.e. that the oxidation takes place only as long as the applied anodization voltage creates an electric field which is strong enough to move the participating ions across the oxide layer. This oxide layer is usually called barrier layer, as it serves as oxidation barrier for the anodization, and as protecting layer against other corrosions. In general, the thickness of the oxide layer $d_{bl}$, is proportional to the applied anodization voltage $U_{anod}$:

$d_{bl} = k \times U_{anod}$

with k=constant, where k depends on the anodization solution and anodization parameters like temperature. For the standard conditions used in the literature and as well in this work, k is in the order of 1.1-1.5 nm/V.

Thus, under standard anodization conditions, a thick barrier layer is formed at the surface of the Al. This anodization technique has been adapted for already over 100 years for the industrial production of corrosion resistant Al. This anodization technique therefore is called “barrier-type anodization”.

However, in aqueous environments which are acidic and can etch aluminium and aluminium oxide, the anodization conditions are different: in this case, in addition to the formation process of alumina, the dissolution of alumina at the interface “alumina”-“anodization solution” takes place. We are therefore in the situation of two concurring processes: the dissolution at the interface “alumina”-“anodization solution” and the alumina formation at the “aluminium”-“alumina” interface, to which the $OH^-$ ions migrate as they are driven by the applied electric field. At this point, it has to be mentioned that the dissolution as well is supported by the electric field, as the $Al^{3+}$ ions, which migrate through the barrier layer, are dissolved into the anodization solution when they reach the interface “alumina”-“anodization solution”. Therefore, in the case of acidic, aluminium etching anodization environment, a complex anodization process with field assisted alumina formation and alumina dissolution takes place, which has not yet been described until today in a perfectly concluding theoretical way.

However, as this process leads to very interesting anodization results, like the formation of porous alumina membranes, today at least a good understanding of the mechanism of this process, which is called “porous-type anodization”, has been

achieved. This mechanism of pore formation and the entire anodization process of the porous-type anodization is the subject of the following paragraph.

### I.2.2 The mechanism of the pore formation

The formation process of porous alumina is the result of a complex interaction between the formation and dissolution of alumina in the acidic environment under application of an electric field. To get a good understanding about the formation process, it is reasonable to start from a “virgin” Al sheet and to investigate the progress of anodization from the beginning oxidation up to the established pore growth. This will be done by the example of a constant voltage anodization, as this is a very common anodization technique and as the constant voltage anodization is rather simple and therefore suited for the investigations of the anodization.
The mechanism of the pore formation is mostly based on two physical processes: The stress inside the $Al_2O_3$ formed at the surface of the Al, and the field assisted dissolution.
The stress inside the formed $Al_2O_3$ is created due to a variety of physical effects. The most important of those is the volume expansion. Generally, the volume expansion ratio, i.e. the ratio between the volume of the initial Al and the finally formed $Al_2O_3$ layer (or better: oxidized layer), depends on the anodization conditions and shows values between 1 and 2 [25]. This wide range reflects the different effects, which influence the volume expansion and depend on the anodization conditions. Of course, due to the incorporation of oxygen ions inside the Al, the volume increases. But in addition, depending on the anodization current, point defects are created inside the formed oxide layer as ions move across the oxide layer [27]. Moreover, different ions, namely of the acidic anodization solutions, can be incorporated as impurities inside the oxide layer, and even the electrostatic field [32] imposes local stress inside the oxide layer, as the oxide acts as a dielectric material between the Al metal and the anodization solution, which implies the formation of local charges close to the respective interfaces and thus creates an electrostatic force inside the rigid alumina which produces stress inside the layer.

The second effect, the field assisted dissolution, is a well known effect since the beginning of research on alumina formation [28,23]. This effect describes the

dissolution of positively charged Al ions at the interface “alumina”-“anodization solution”. The positively charged Al ions generally cross (*beginning form the Al-alumina interface*) the alumina layer and finally are dissolved in the anodization solution and there become neutral due to charge exchange with negatively charged $OH^-$ or $O^{2-}$ ions. Moreover, it has also been supposed [23] that the electric field weakens the bonds of the $Al_2O_3$ and thus decreases the activation energy of the dissolution of Al in the solution. This leads to an effective etching of the alumina layer during the anodization process. The etching rate hereby depends strongly on the aggressiveness of the anodization solution and on other parameters like the ambient temperature or the anodization current.

The effective mechanism for the pore formation has been discussed largely in the literature [23,29,30,31]. In the following, the common principle of the mechanism, which has been verified today, will be discussed. The discussion hereby is illustrated by a typical current-time graph of such constant voltage anodization and by a schematic drawing showing the development of alumina at the surface of the Al during the anodization process (Fig. I.1).

At the very beginning of the anodization process *(Fig. I.1, [1])*, the voltage is applied to the “blank” Al with just some nm of native alumina at the surface. Thus, the initial current is very high *(Fig. I.1, [1])*, as there is a very low resistance between the conducting Al and the anodization acid in which the counter electrode is positioned. This leads to a sudden oxidation of the Al surface, and a thick, insulating alumina layer is formed, which induces a current breakdown of the anodization current *(Fig. I.1, [2])*.

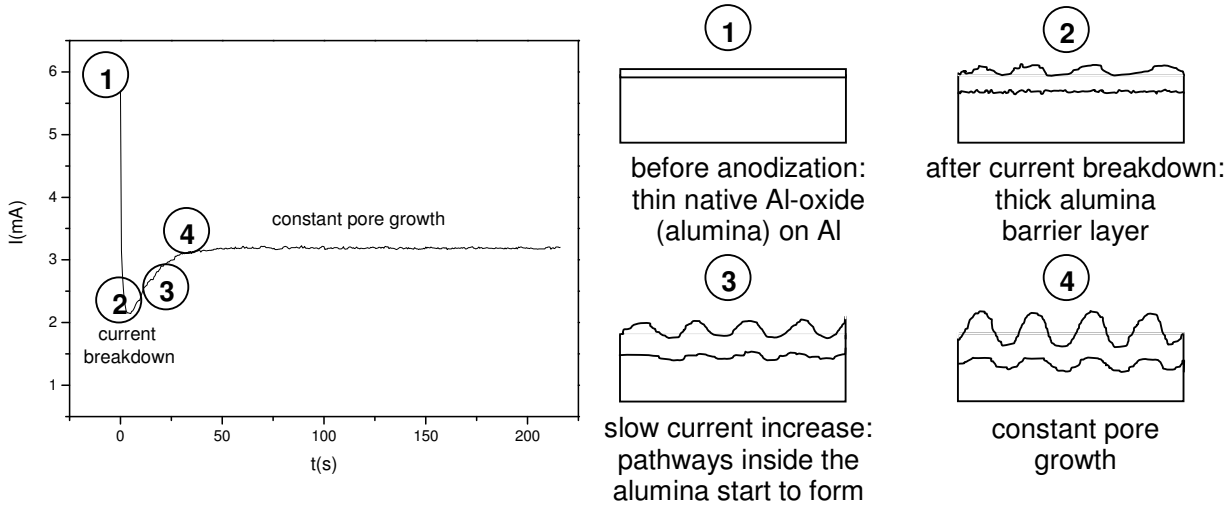


*Fig. I.1: Current-time plot of the anodization process and schematics of the anodization process.*

The anodization comes along with volume expansion and stress in the formed $Al_2O_3$. Thus, starting from a perfectly smooth Al surface, the sudden anodization of the Al leads to a rough $Al_2O_3$ surface with statistically dispersed thickness maxima *(Fig. I.1, [2])*. In this state, the oxide is still film-like and supposed as a barrier type alumina. With ongoing anodization, the density of these thickness maxima increases, but still thin areas between these maxima are present *(Fig. I.1, [3])*. The applied electric field therefore is strongly concentrated in these thin areas, which preferentially supports the ion transfer through the thin alumina in these areas and weakens the Al-O bonds. At this point, the field assisted dissolution of alumina becomes important. In these areas, an effective etching of alumina takes place and leads to small, etched pathways between the thickness maxima *(Fig. I.1 [3] and [4])*. These pathways again allow an anodization current, and the dissolution and the formation of alumina become coexisting processes: Namely at the bottom of the pathways the electric field is very high and the curvature of the alumina at the bottom of the pathways additionally weakens the Al-O bonds, thus leading to dissolution, whereas in all areas, in which the Al is in electrical contact with the anodization solution, alumina is formed. Thus, around the bottom of these pathways, the oxide formation is faster than the dissolution (as here, the electric field is lower), and at the bottom, precisely in the curvature, an equilibrium between the dissolution and formation of alumina is established. In this state, a real pore growth takes place *(Fig. I.1, [4])*, during which the Al is oxidized in depth by creating a porous alumina structure. Such porous

alumina structure consists thus of pores, whose “height” depends on the anodization duration (the longer the anodization, the longer the pores) and an alumina layer at the pore bottom, called barrier layer, which separates the Al of the sample from the interior of the pores, i.e. during the anodization from the anodization acid.

### I.2.3 Ordered PAA membranes: Principles

The previous paragraph has shown the main principles of the formation of porous alumina: the volume expansion and stress during the oxidation of Al, combined with the field-assisted dissolution of alumina, leads to an equilibrium state between the dissolution and the formation of alumina, in which a vertical pore growth inside the Al substrate takes place.

The ordered PAA structure is a consequence of the formation mechanism itself: At all pore bottoms, $Al_2O_3$ is formed from Al, leading to a respective volume expansion and stress in the material around all pore bottoms. As the stress is equal in all pore-bottoms, there is an equal, isotropic lateral stress in the alumina which is formed at the pore bottom. This isotropic stress around all pores influences the pore growth in a manner, that, during the formation process, the pores are getting positioned in equidistant locations. Therefore, the pores form a “closely packed structure” that is well known in many domains. This structure is a hexagonal one, with one pore equidistantly surrounded by six other ones.

However, this argumentation is only valuable, if the anodization starts on a perfectly flat Al surface. Only in this case, there is a real random distribution of the thickness maxima of the initially formed alumina layer, which leads to statistically dispersed pores which then can be “moved” in equidistant manner, i.e. form a closely packed structure. If the Al surface itself is rough at the beginning, the apparition of thickness maxima of the alumina is predetermined, for the peaks of the surface are much faster oxidized. Thus, the pores start to grow at predetermined positions and the distances between them are too different to be adjusted to a perfectly ordered structure.

The hexagonally ordered pore structure, of course, cannot appear from the beginning of the anodization process, as only the stress during the established pore growth can lead to the ordered structure. Therefore, at the surface, the PAA structure is not yet ordered, but getting increasingly ordered by increasing depth. In a side view of a PAA structure, it can be clearly observed that the pores change their direction at

the beginning of the anodization, i.e. close to the surface, and later become straight. This effect is undesirable for further applications, as the pore diameter and direction are not constant over the length of the pores. This problem has been solved by Masuda et al. in 1995 [24] by the “2 step anodization”. In this anodization technique a first anodization is carried out starting from a perfectly flat Al surface. This first anodization is done until the pores are well straight, and the entire alumina structure formed during this first anodization is then etched by a selective etchant which etches alumina without etching Al (e.g. by “chromic acid”, a mixture of 1.7 wt % $CrO_3$ and 6 wt % $H_3PO_4$, commonly etched at 60 °C). This leads to an Al surface on which there are the imprints of the pore bottoms of the porous structure fabricated during the first anodization. A following second anodization starting from this surface produces pores which start preferentially from the imprints on the surface, which are already hexagonally ordered. Thus, a perfectly ordered, straight porous PAA structure can be obtained.

The main parameters like the cell size (also: cell diameter), the pore size (also: pore diameter) and the barrier layer of ordered PAA are shown in Fig. I.2.

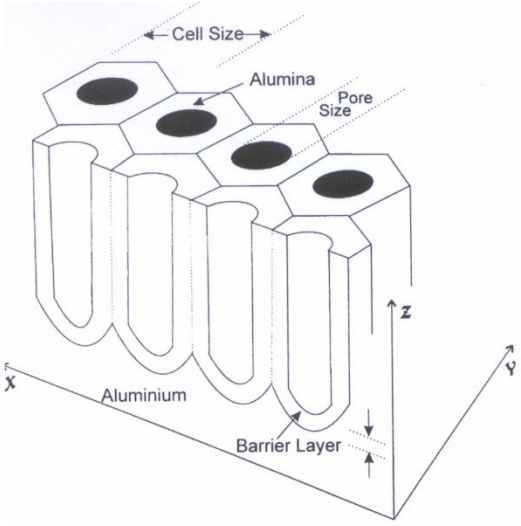


*Fig. I.2: Schematic 3D illustration of ordered PAA.*

## I.2.4 Influence of the anodization parameters on the PAA structure

The anodization process for the fabrication of PAA structures is very sensitive for a wide range of parameters. Both the formation with resulting volume expansion and the dissolution depend strongly on the applied conditions, and thus it is a real challenge to control the equilibrium state between these two, on which the PAA formation process is based. The most significant parameters for the anodization are the anodization voltage and the anodization acid. But also the temperature of the anodization acid, the electrode area of the counter electrode and the agitation of the anodization acid during the anodization have an influence on the anodization. In the following, the main parameters which influence the anodization will be discussed.

The main parameters of the PAA structure like the pore diameter $d_p$, the cell diameter $d_c$ and the barrier layer $d_{b.l.}$ are directly proportional to the applied anodization voltage $U_{anod.}$. The pore density is also directly proportional to $U_{anod}$. Furthemore, the oxide at the pore bottom (the barrier layer) becomes thicker with increasing anodization voltage and thus also the pore walls and the pore diameter (and therefore the density lowers). Consequently, the detailed control of the PAA fabrication is a complicated subject.

It has been shown in early publications [24, 25] that the pore diameter increases linearly with increasing anodization voltage (Fig. I.3).

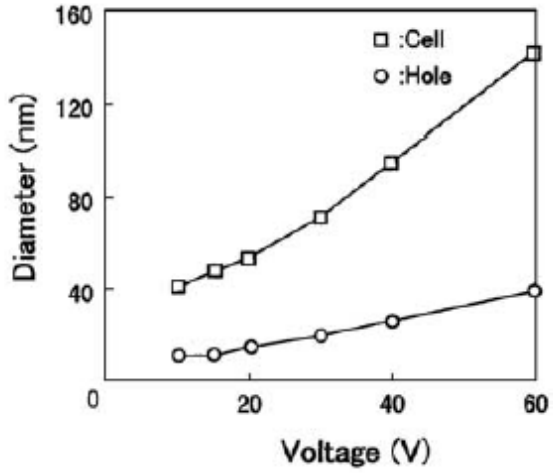


*Fig. I.3: Dependance of the hole diameter and of the cell diameter on the applied anodization voltage.*

However, in order to get an ordered PAA structure, the voltage and the used anodization acid depend on each other, as the anodization current and the equilibrium state depend on the aggressiveness and pH of the used acid. This especially influences the volume expansion rate and the incorporation of defects in the fabricated alumina and thus influences strongly the order of the PAA structure. A volume expansion rate (volume expansion from Al to $Al_2O_3$) of 1.4 [25] or 1.2 [32] has been suggested to be the optimized one for ordered PAA fabrication, and the influence of the current density has been proven [33]. Thus, the anodization acid has to be adapted to the applied anodization voltage. For very high anodization voltages, only slightly etching acids with relatively high pH are used, and with decreasing anodization voltages, more aggressive anodization acids have to be chosen. Apart from the described argumentation, stronger acids also lead to higher etching ratios at the pore bottom and thus create stronger curvatures of the pore bottoms, which also is favourable for the creation of small pores at low anodization voltages.

Commonly, there are three types of acid used for the fabrication of PAA by anodization: sulfuric acid ($H_2SO_4$) (from ~5 V to ~30 V), oxalic acid ($H_2C_2O_4$) (from ~20 V to ~ 80 V) and phosphoric acid ($H_3PO_4$) (from ~ 70 V to 250 V), but recently, higher anodization voltages with very low acidic anodization solutions have been realized [34]. For all different cases, there is always an optimized anodization voltage for each acid, at which the PAA structure with the best order is obtained. For instance, in case of a solution of 0.3 M oxalic acid, the anodization voltage of 40 V has been shown to be the best adapted for ordered pore growth, in case of a 0.3 M sufuric acid, 25 V [31,25].

The temperature, of course, influences largely the chemical reactions of the anodization process. In general, the anodization rate increases with increasing temperature, but also the order of PAA is influenced by the temperature [35]. However, the optimized temperature always depends on the anodization acid and until today, very few systematic investigations on the optimization of the temperature have been done.

Rather experimental parameters, which influence the PAA fabrication, will be discussed in the following experimental section.

# I.3 Results and discussion

## I.3.1 The anodization setup

For the experiments in this work, special setups have been designed for the anodization of Al surfaces. In Fig. I.4, images of the setups are shown. The idea of these setups is to allow anodization of such Al surface without the need of lithography steps, i.e. to give the possibility to isolate a defined area of the Al surface which then is exposed to the anodization solution. One important feature of the setups is thus to provide the possibility to mount a sample with Al surface and to allow the anodization at a reproducible surface area. Besides, during the anodization, bubbles are produced close to the surface of the sample. These bubbles must be removed from the sample surface in order to avoid an insulation of some surface areas. Thus, the sample must be mounted with the surface at the top, so that the bubbles can be removed by heavy stirring above the sample.

Two different setups (Fig. I.4, [Setup A and Setup B]) have been designed for this work, corresponding to two different anodization surfaces. The first one allowed the anodization of a surface of 0.38 $cm^2$, the second one the surface of 11 $cm^2$. The first one was rather adapted for small test samples, the second one for the anodization of 2” wafers.

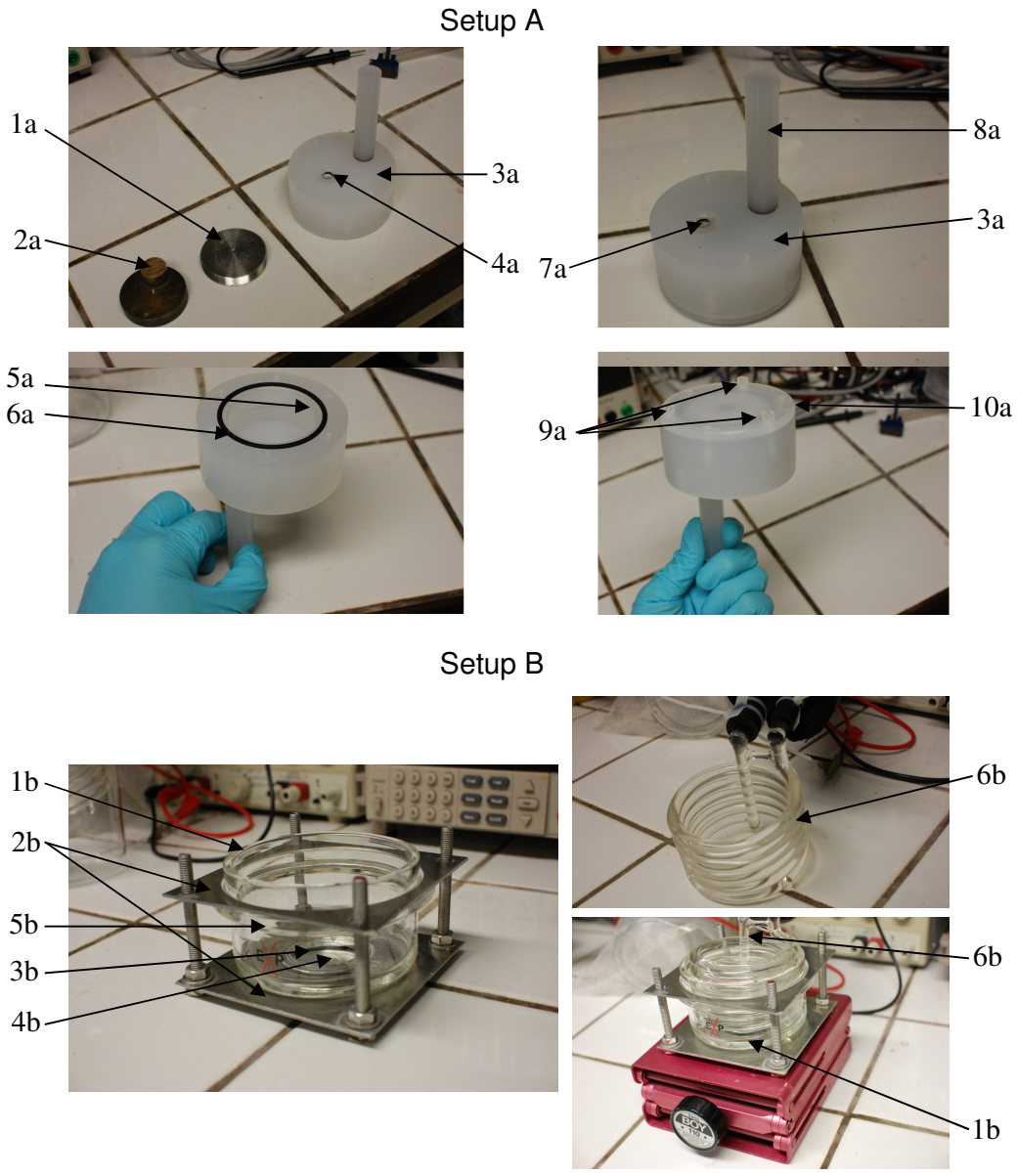


*Fig. I.4: The anodization setups used in this work: Setup A is used for small samples (0.38 cm²), setup B is used for 2" wafers (with 11cm² open area).*

In the figures, the elements of the setups are referenced in the following way:
1a: screw inside the sampleholder in order to fix the Co-plate with the sample
2a: Co-plate on which the sample is positioned and which is pressed against the o-ring 4a by the screw 1a
3a: sampleholder
4a: o-ring which is pressed on the surface on the sample
5a: thread for the screw 1a
6a: o-ring at the bottom of the sampleholder which insulates the sampleholder
7a: sample inside the sampleholder
8a: channel for the electrical contact of the copper plate 2a
9a: screws at the back of the sample holder which press the cover plate 10a on the o-ring 6a
10a: cover plate

1b: two-side open glass beaker
2b: steel setup which presses the glass beaker on the o-ring 3b
3b: o-ring at the downer open end of the glass beaker 1b and which is positioned between the sample 4b and the glass beaker 1b
4b: sample
5b: flange of the glass beaker 1b
6b: glass coil

The two setups are designed following two different concepts: The first one (Fig. I.4, [Setup A]) includes a teflon sampleholder (Fig. I.4, [3a]), in which the sample is mounted in following steps: first, the sample is fixed on a copper plate (Fig. I.4, [2a]) by silver paste, then this Co-plate (Fig. I.4, [2a]) is put and fixed inside the sampleholder (Fig. I.4, [3a]) wherein a screw (Fig. I.4, [1a]) presses the Co-plate (Fig. I.4, [2a]) with the mounted sample (Fig. I.4, [7a]) against the o-ring (Fig. I.4, [4a]), then the sampleholder is closed at the bottom by a cover plate (Fig. I.4, [10a]), which is pressed by three screws (Fig. I.4, [9a]) against the o-ring (Fig. I.4, [6a]) at the bottom of the sampleholder. The sampleholder (Fig. I.4, [3a]) itself is put in a beaker containing the anodization acid. This beaker is put into a double-walled thermobeaker whose temperature is controlled by an external cooler.

In case of the second sampleholder (Fig. I.4, [Setup B]), an open glass beaker (Fig. I.4, [1b]) is directly pressed on the sample (Fig. I.4, [4b]) with a connecting o-ring (Fig. I.4, [3b]) in between. The pressure is realized by a steel setup (Fig. I.4, [2b]), that consists of two steel plates connected by four screws. The sample (Fig. I.4, [4b]) is fixed on the lower steel plate by silver paste, and the upper steel plate is screwed versus the lower one, while said upper plate presses on the flange (Fig. I.4, [5b]) of the glass beaker (Fig. I.4, [1b]). A glass coil (Fig. I.4, [6b]) is then put in the beaker, and an external cooler is connected to the coil.

In both cases, the temperature of the cooler is controlled by an external thermocouple which is positioned inside the anodization acid. The agitation of the anodization solution is done by a stirrer consisting of a glass bar, and the rotation speed is controlled by an electric motor and its power supply. As counter electrode, a graphite plate is used whose surface always has been significantly larger than the anodized surface.

All anodization has been done in the potentiostatic mode, i.e. the anodization voltage is fixed at a defined value and the anodization current is measured by an amp meter. We used the programmable power supply “Itech Electronic IT6834”, so that the voltage could be varied over the anodization duration following any function.

## I.3.2 The formation rate of PAA

The formation rate of PAA, i.e. the rate, in which the thickness of PAA increases on the Al sample, is fundamental for any kind of application using PAA as a membrane. Namely for applications like the use of PAA as etching mask, which is discussed in the chapter IV, the thickness of the PAA membrane must be precisely controllable.

Basically, the thickness of PAA is controlled by the anodization time. However, this time control is not evident, as the formation rate of PAA changes during the anodization and as the anodization rate depends on the pre-treatment of the sample before the beginning of the anodization. These effects will be discussed in this chapter.

Of course, directly after the application of an electric field, the formation rate of PAA changes as long as the pore growth is not yet in the equilibrium state. This is evident from the current-time plot of the anodization which is represented in Fig. I.1. Besides, this non-linearity of the formation rate of PAA is not the same for the first and the second anodization. This can be understood in view of the comparison of the current-time plots of the first and second anodization (Fig. I.5). The minimum of the second anodization current is much less important than the first anodization one, and the constant current value is reached much faster. Besides, it is obvious that the plateau of the anodization current does not show a constant current like in case of the first anodization, but a slight decreasing current. This will be discussed later in this paragraph.

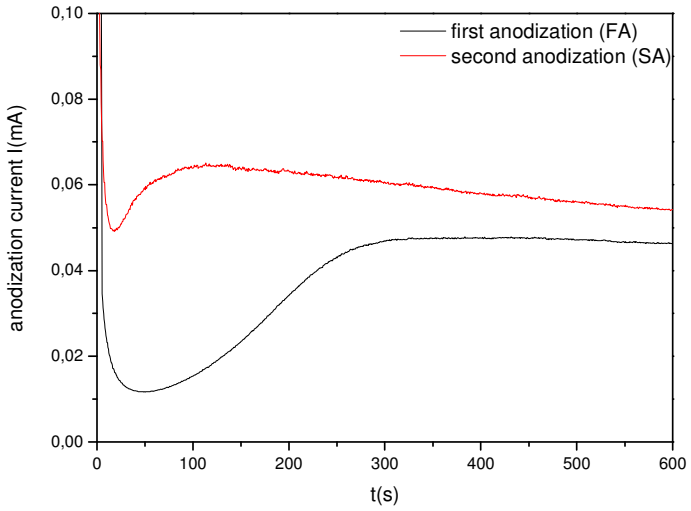


*Fig. I.5: Current-time plot of the first and second anodization, done on the same sample under identical conditions.*

In Fig. I.6, the different behaviours for the first and the second anodization are obvious: while for the first anodization, the formation rate is increasing during the first 7 min before the rate becomes constant, in case of the second anodization, the formation rate increases fast for short anodization times and then is approximately constant, showing a slight decrease. In addition, the formation rate during the second anodization is in general higher than during the first anodization. These differences can be explained by the current-time plot for both cases shown in Fig. I.5.

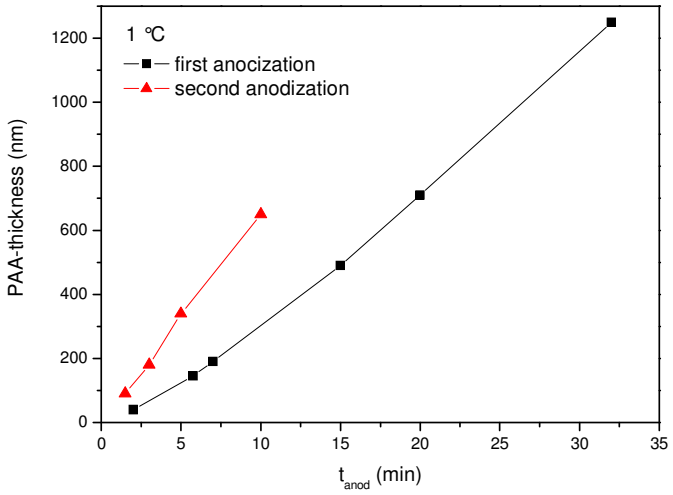


*Fig. I.6: Formation of PAA during the first and the second anodization. The anodization has been done at 40 V in 0.3 M oxalic acid at 1 °C.*

The formation rate when the constant value of the current is reached is different for the first and the second anodization, the second anodization leads to a 'constant' formation rate which is about 1.4 times higher than the constant formation rate of the first anodization. This effect must be due to the imprints made during the first anodization, which first of all simplify the start of the pore growth and thus lead to a faster stabilization of the formation. On the other hand, the straight pores seem to influence the formation rate, probably because the migration of the ions through the straight pores is much easier than in case of the crooked ones of the first anodization. PAA structures fabricated by a first anodization step also show much smaller pore diameters at the surface than those for the second anodization, since at the beginning of the first anodization, a thick alumina layer is formed in which slowly pathways are developed. This again contributes to the difference of the formation rate between the first and the second anodization in the sense that during the second anodization PAA is formed faster.

However, there is one more difference between the second and the first anodization: During the first anodization, the constant anodization current of the plateau is nearly constant while during the second anodization, the current decreases with the time. For this reason, the formation rate of the PAA also decreases slightly with the time (see Fig. I.6), which is not the case for the first anodization (at least not in the range shown in Fig. I.6. For very high thicknesses (>3 µm), this effect starts for the first

anodization as well since also here, like explained above, the pore depth starts to make the ion transport through the pores slower.

In addition to the effect of a non-linear formation rate during the anodization process, the temperature of the anodization acid plays an important role for the formation rate. This is evident and will not be discussed in detail in this chapter. However, the strong temperature dependence implies a precise control of the temperature, which itself makes it necessary to keep the sample for some time in the anodization acid before starting the anodization, until the anodization temperature is constant. In this work, we found that this delay time before the beginning of the anodization has a very strong influence on the anodization rate. This effect has so far not been reported in literature and illustrates very well the difficulties in getting reliable results, e.g. for the formation rate, about the PAA formation process.

The effect is shown in Fig. I.7 and Fig. I.8, showing the thickness of a PAA membrane obtained after 10 min of anodization after a certain “dipping time”, i.e. delay time, in which the sample has been inside the solution before the anodization. In Fig. I.7, the variation of the dipping time at an anodization bath temperature of 5 °C is shown. Obviously, the anodization becomes slower with increasing dipping time. The most reasonable explanation of the effect seems to be the thickened oxide layer which is formed while the Al is exposed to the solution. This reason, however, implies that the formation rate of alumina under these conditions is higher than the dissolution rate. We believe, that a thicker oxide is formed which makes the creation of pathways in order to initialize the pore growth more difficult and which hinders the ionic transport inside the pore.

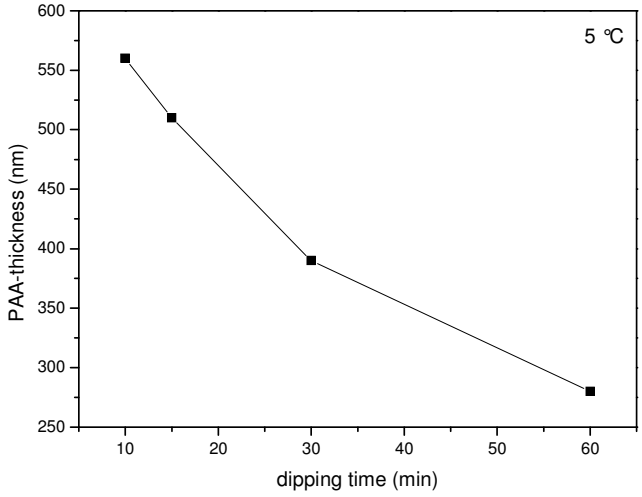


*Fig. I.7: PAA-thickness after 10 min anodization at 40 V in 0.3 M oxalic acid versus dipping time for an anodization bath temperature of 5 °C.*

The interpretation, that at 5 °C in 0.3 M oxalic acid without applying an anodization voltage the formation rate of alumina is higher than the dissolution rate, of course, is only valuable for these specific conditions.

Therefore, the same dipping time variation has been done at 25 °C without changing the other anodization parameters. The result is shown in Fig. I.8.

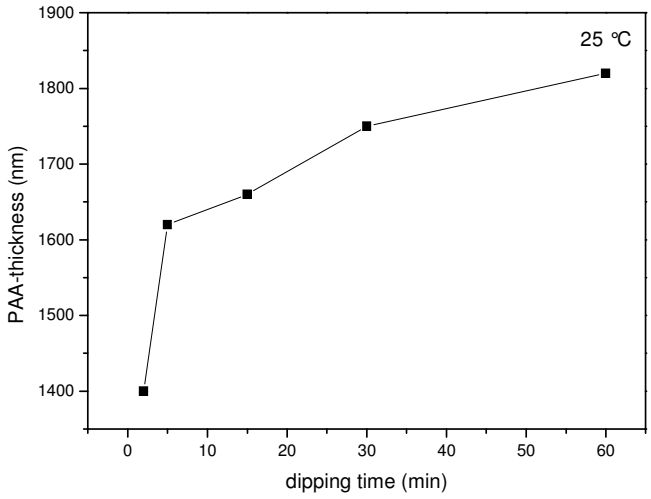


*Fig. I.8: PAA-thickness after 10 min anodization at 40 V in 0.3 M oxalic acid versus dipping time for an anodization bath temperature of 25 °C.*

In this case, the effect is inversed in comparison to the case of 5°C: The PAA thickness increases with increasing dipping time. Following the explanation given above, this indicates, that at 25 °C and without applying an anodization voltage, the formation rate of alumina is lower than the dissolution rate, which reduces effectively the thickness of the protecting oxide at the Al surface.

The above discussed results show clearly that for any formation rate determined under specific anodization conditions, the dipping time should always be referred. Besides, it illustrates, that for any reliable analysis and investigation of PAA formation, the dipping time must be kept constant during any series. The comparison between the PAA formation at different temperatures therefore is difficult, as the time, during which the sample must be in the solution until a constant temperature is obtained, depends on the difference of the room temperature and the anodization bath temperature. In any case, it is obvious that the anodization already starts as soon as the sample is put inside the solution, and not only with the application of the anodization voltage.

Although the comparison of the formation rate of different anodization conditions comes along with the mentioned difficulties, a summary of formation rates for the second anodization for different anodization conditions is given in Fig. I.9. Here, the dipping time has always been fixed to 25 min.

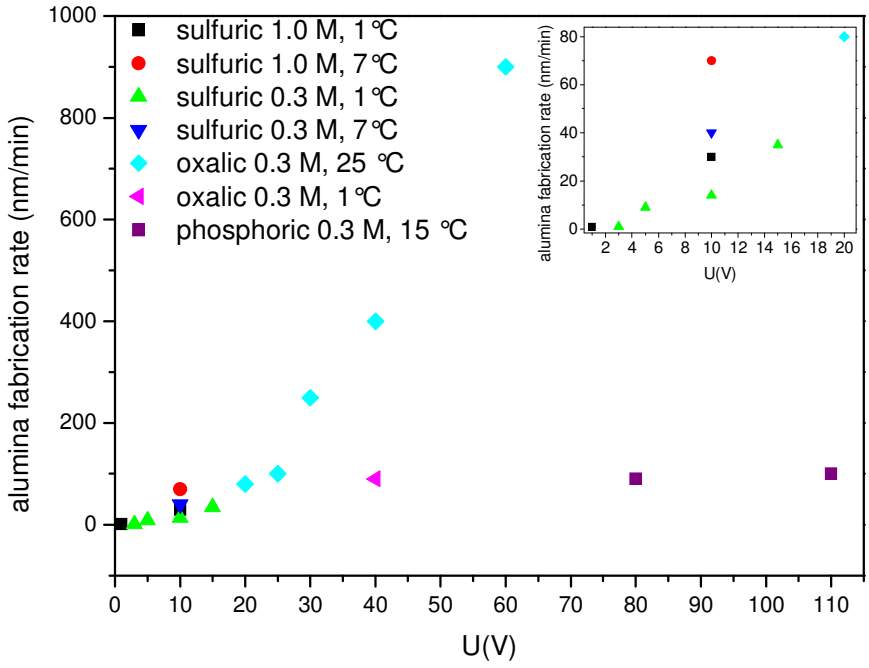


*Fig. I.9: Influence of the anodization acid and temperature on the formation rate of the second anodization.*

In principle, it is shown that the formation rate depends strongly on the applied voltage, the acid and the temperature. With increasing acid concentration, the formation rate increases due to the higher etching and oxidizing behaviour. The temperature is shown to have a very strong influence (the formation rate for 0.3 M oxalic at 25 °C is about 4 times higher than at 1 °C), which shows the importance of a very precise control of the temperature. At this point, it should be mentioned that the formation rate is only a very simple method to show the difference in the anodization conditions. A different formation rate always refers to a completely different equilibrium state between the dissolution and the formation of alumina, which is also important for the anodization process itself, for instance for treatments like the one described in section I.3.5.

### I.3.3 The dependence of the order of PAA on the anodization conditions

For most applications of PAA, in which the PAA is formed on the basis of a thin film Al layer, it is important to obtain a highly ordered PAA structure by only using a very thin layer for the first anodization, i.e. to get to a well ordered PAA structure without creating a thick PAA layer during the first anodization. This is especially important if a relatively thick ordered PAA structure is needed like for the use of PAA as etching mask (see chapter IV).

As the deposition of thick high quality Al layers (>2 µm), without oxygen or other impurities inside, is a challenge which affords expensive equipment, the need of a method to realize “fast” (in terms of thickness) an ordered PAA structure is of high interest.

Thus, the knowledge of the conditions, under which the order in PAA is obtained very quickly, is of great importance. However, until today, only few studies have focused on this point [35, 36].

Therefore, in this work, we have compared the order of PAA by top views on PAA structures prepared after a first anodization at different temperature and time. The goal hereby was to investigate, if rather a higher temperature leads to more flexible pore growth in terms of lateral movement of the pores and thus leads quickly to a well ordered structure or if rather a low temperature anodization leads to very slow growth and thus a “faster” (in terms of thickness) ordered organization of the pores.

For this reason, we compared the order of PAA (fabricated by a second anodization) after a first anodization at 25 °C at different times with the order of PAA (fabricated by a second anodization) after a first anodization at 5 °C at different times. For both cases we used 0.3 M oxalic acid as anodization bath. For each first anodization we fabricated under the respective conditions of the first anodization test samples for a measurement of the thickness of this PAA. Thus, we were able to compare different states of organization with different thicknesses for the first anodization.

In Fig. I.10, some examples are given for the anodization at 5 °C and at 25 °C. In the SEM images (using an Hitachi S4800 FEG), a topview on PAA surfaces fabricated by a second anodization is shown. The conditions of the previously realized first

anodization (FA) is mentioned on each image, indicating the thickness of the PAA that is formed during the first anodization and the duration of the first anodization.

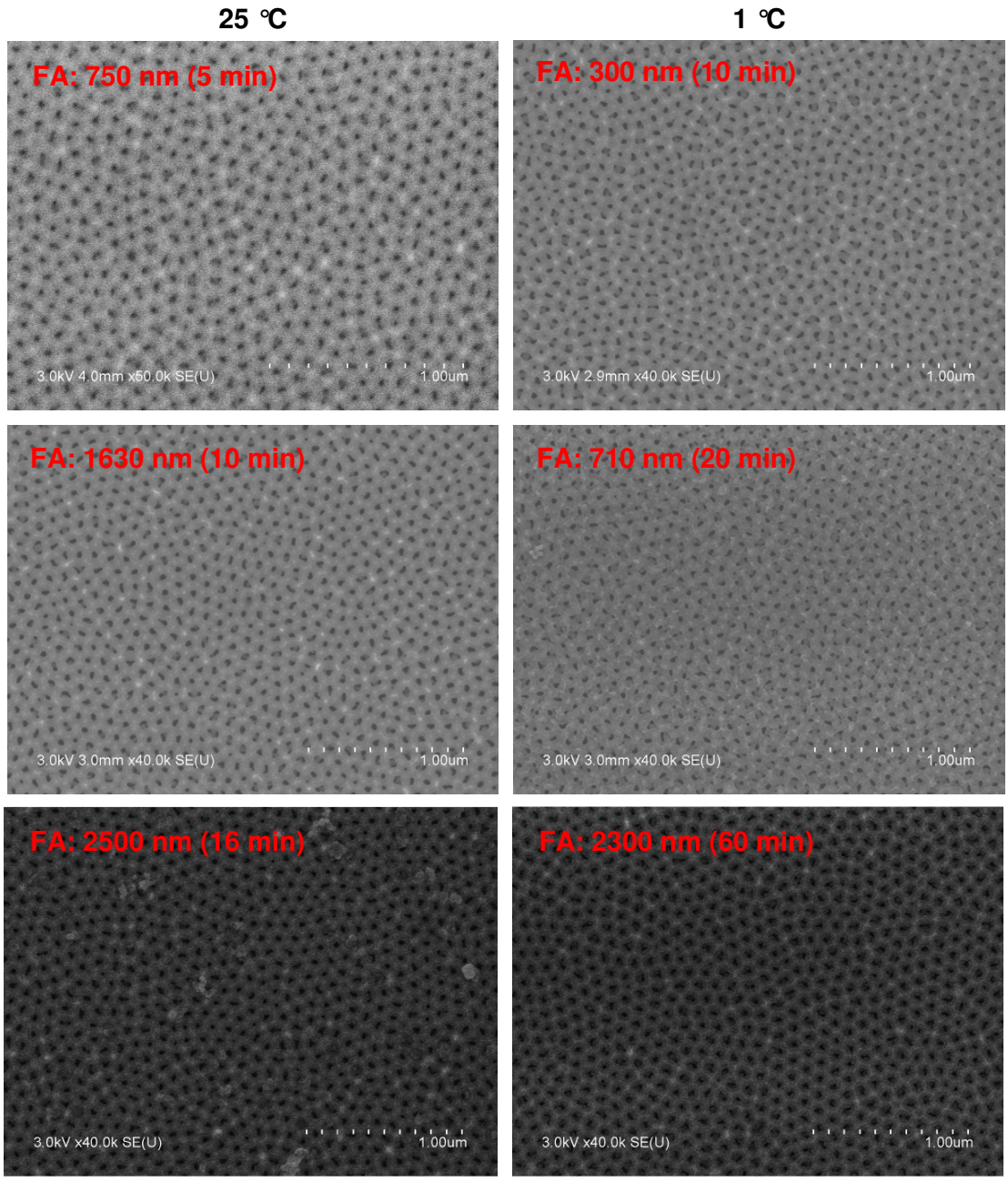


*Fig. I.10: Order of PAA fabricated by a second anodization of 5 min after first anodization steps (FA) with different temperature and duration conditions.*

The analysis of those figures shows that there is a remarkable difference between the anodization at 25 °C and 1 °C: While in the case of 25 °C, there is nearly no ordered domain after a first anodization of 750 nm thickness, in case of 1 °C, ordered

domains are well present after a first anodization of 710 nm thickness. By strongly increasing the anodization time of the first anodization, in both cases, only a slight improvement of the order could be obtained. It has been reported that a very good order has been obtained after 16 h for the first anodization, which, of course, cannot be realized in case of thin film Al. Therefore, it seems reasonable to choose a compromise between a very good order and a short first anodization. For this goal, the anodization at 1 °C is far better adapted than the one at 25 °C, and it can be concluded that the slow pore growth at lower temperatures leads much “faster” (in terms of thickness) to a good order in PAA than the high mobility at higher temperatures.

Obviously, with increasing duration of the first anodization, the order of the PAA structure of the second anodization is improved, which can be verified by the bigger domain size of ordered pores.

### I.3.4 PAA with ultra small pore diameter

With increasing research activity and a resulting improved control of the fabrication of PAA structures, the interest for the use of PAA in nano-applications has sparked. For this goal, however, PAA structures with very small pore diameters are of strong interest, as especially nano-devices in the order of some nm would mean a breakthrough for new generation applications. One possible application could be the use of PAA for interconnectors, if in each pore one conducting nanoelement can be placed and these nanoelements then can be contacted in parallel. Such application would need a very high pore density and thus a very small pore diameter.

Therefore, one goal in this work has been the reduction of the pore size of PAA, also in respect of a future organization of nanoelements like SWCNTs in a manner, that these very small nanoelements with diameters of a few nm can be embedded in pores with pore diameters in the same order of magnitude. This is the reason why we have tried to decrease the pore diameter as small as possible, trying to determine the lower limit of the pore diameter and the upper limit of the pore density of PAA. This study therefore was namely carried out to investigate how far new applications of PAA, like the provision of channels of very high density for the fabrication of a new generation of interconnectors could be realized.

Generally, as it has been seen before, the pore diameter of the PAA depends on the applied anodization voltage, whereas the diameter is proportional to the applied voltage in a wide range. However, as already discussed, in order to obtain the equilibrium state between the formation and dissolution of alumina, which is necessary for the pore growth, the anodization acid must be adapted to the applied voltage.

The usually used standard acids are phosphoric ($H_3PO_4$), oxalic ($H_2C_2O_4$) and sulphuric ($H_2SO_4$) acid, where sulphuric is the strongest one and adapted for the smallest pore diameter of the PAA structure. However, the smallest pore diameter achieved so far is about 7 nm, where the anodization has been done at 6 V in 0.1 M sulphuric acid at 3 °C [26]. Recently, another approach for decreasing the pore diameter has been demonstrated using a very cold anodization solution. Highly ordered PAA has been reported with 14 nm pore diameter, prepared at 25 V in 0.3 M sulphuric acid at -15 °C [37]. However, no smaller pore diameters have been reported so far by this technique.

In this work, we focused on the effect that acids with increasing aggressiveness imply a stronger curvature of the pore bottom of PAA structures. As basic investigation, we have studied the influence of the temperature on the pore growth at very low anodization voltages in highly concentrated acids. Further, different types of strong acids and concentrations of these acids were tested. By this, we tried to find highly aggressive anodization solutions and to adapt the applied anodization voltage in a way that ordered pore growth can take place. The fundamental principle of this study consists in the fact that the formation and dissolution process depends on the applied anodization voltage and the anodization solution. By combining strongly aggressive anodization solutions with low voltage, we have found anodization conditions for the ordered growth of very low diameter PAA. We often use the term “aggressiveness” for the description of the anodization solution in its effect on the Al or alumina, being aware that this “aggressiveness” is a complex interaction of different specific properties of the respective solution. In fact, many additional parameters like the mobility of the ions inside the anodization solution, the etching behaviour of the solution and also the surface interactions between the solution and the sample are important.

### I.3.4.1 Influence of the concentration of the sulphuric acid on the PAA formation

A 0.1 M or 0.3 M sulphuric acid solution is commonly used for the fabrication of small diameter PAA. In a first series, sulphuric acid solutions with different concentrations have been tested for very low anodization voltages. The result for each anodization has been controlled by SEM top-view images on PAA fabricated in a second anodization step (see Fig. I.11). The PAA formation rate is strongly different for the 3 different acid concentrations. In order to obtain a comparable order in all different cases, a very long first anodization step of 4 h was applied for the first anodization. Thus (see also section I.3.3), as the order acquired after a very long first anodization step does not vary too much with still increasing first anodization time, the orders of the samples fabricated under these conditions can be correctly compared.

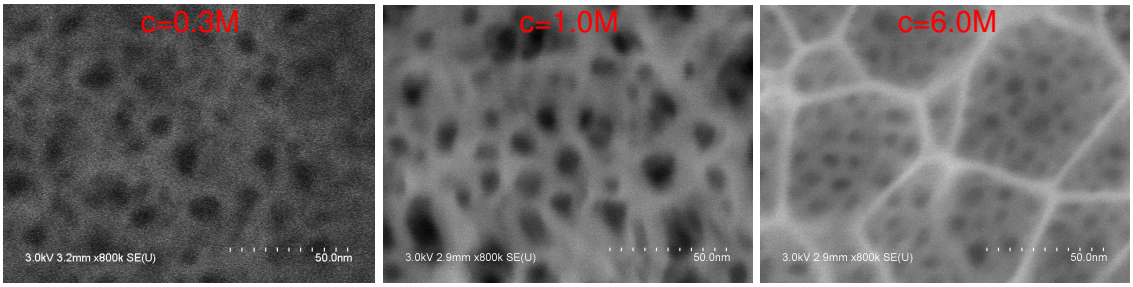


*Fig. I.11: SEM top view on PAA samples fabricated at 1 °C and at 1 V for different concentrations c of the sulphuric acid.*

In this series, the influence of the concentration of the acid is straightforward. At low acid concentration, only very dispersed pore growth can be observed. This indicates that with this concentration, no real field assisted etching and formation of alumina take place, and there is neither a strong etching nor a uniform structure at the surface. However, with increasing concentration of the anodization acid (at 1.0 M), the etching effect at the surface can be clearly seen. However, there is no real pore growth, and the surface of the PAA is strongly etched and not uniform. Obviously, in this case no steady pore growth with a stable equilibrium state is reached during the anodization. By even higher concentrations (6.0 M), the strong aggressiveness of the solution causes a sufficiently strong etching of the oxide (barrier layer), so that the field assisted dissolution and the formation of the alumina reach an equilibrium state. The

curvature of the pore bottom due to the strong etching behaviour of the solution leads to a real pore growth, which can be observed by the good order of the pores seen at the surface. The bright lines on the surface of the 6.0 M sample result from the etching of the PAA itself at the surface, which leads to tip-like etching lines on the surface, but which does not influence the PAA structure itself.

### I.3.4.2 Influence of different acids on the PAA formation

In the previous section I.3.4.1, it has been shown that the most uniform pore growth with very at 1 V can be achieved at 1 °C in 6.0 M sulphuric acid. In order to investigate the smallest possible pore diameter and the highest possible pore density, based on results obtained with the 6.0 M sulphuric acid, we have studied the PAA formation at 1 °C at very low voltages in different anodization acids and compared the effective pore diameter and pore densities for the best adapted acids with the results obtained for the 0.3 M sulphuric acid, which is the standard anodization acid used for small pores in PAA.

The choice of the different anodization acids was motivated by the idea to increase the aggressiveness of the anodization solutions in comparison to the 6.0 M sulphuric acid. We therefore added different amounts of nitric acid ($HNO_3$) or hydrochloric acid (HCl).

Some results for different anodization solutions are reported in Fig. I.12.

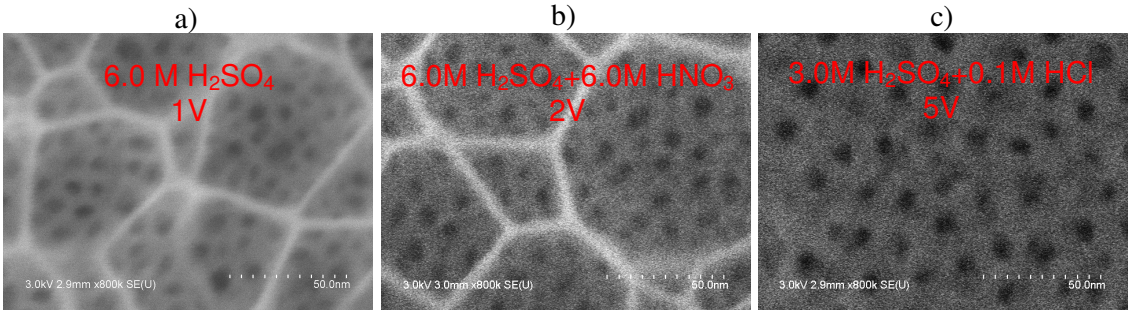


*Fig. I.12: Influence of acids nature on the pore growth*

In case of the addition of nitric acid, a strong acid which however does not etch alumina or Al strongly, the addition of even high amounts of nitric acid (6.0 M) did not lead to a significant change of the PAA structure (see Fig. I.12 b). By adding nitric acid in different concentrations to different concentrations of sulphuric acid, we could not observe in any case a significant change of the PAA structure.

In contrast, by adding hydrochloric acid to the sulphuric acid, significant differences could be observed. By adding 0.1 M hydrochloric acid to the sulphuric acid, the pore diameter, the pore density and the order of the PAA changed. These differences are based on the strong etching behaviour of hydrochloric acid towards Al, which changes the dissolution rate of Al into the anodization acid significantly. The best results in terms of the pore density and the order have been obtained by the addition of 0.1 M hydrochloric acid (see Fig. I.12 c). For lower concentrations, the effect was less significant. For higher concentrations, too strong etching hindered the pore growth and etched very fast high thicknesses of the Al layer of the sample.

In order to quantify the influence of the hydrochloric acid on the PAA formation, in Fig. I.13, the pore diameter and the pore density are plotted for a wide range of anodization voltages in the case of 6.0 M $H_2SO_4$ and 6.0 M $H_2SO_4$+0.1 M HCl. This is compared with respective measurements on PAA fabricated in 0.3 M sulphuric acid. At this point it should be mentioned that the incertitude of the measurements of the pore diameter and the pore density is not comparable: While the pore diameter is measured for several single pores, the density is measured by counting the number of pores in a large surface. Thus, the incertitude of the measurement of the pore diameter is much higher than the one of the measurement of the pore density.

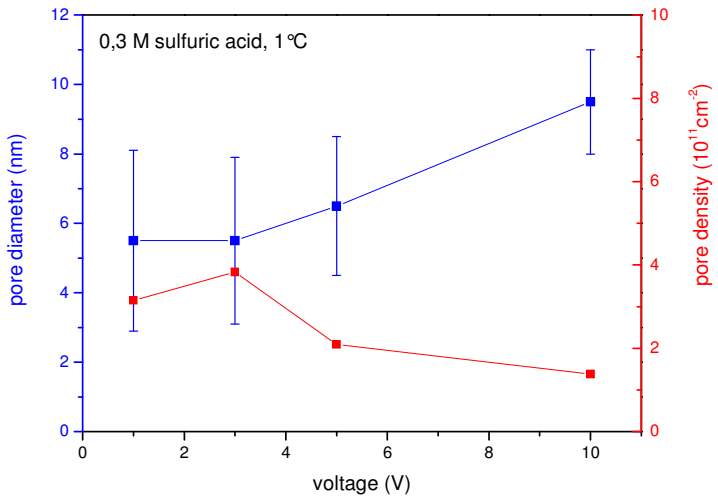

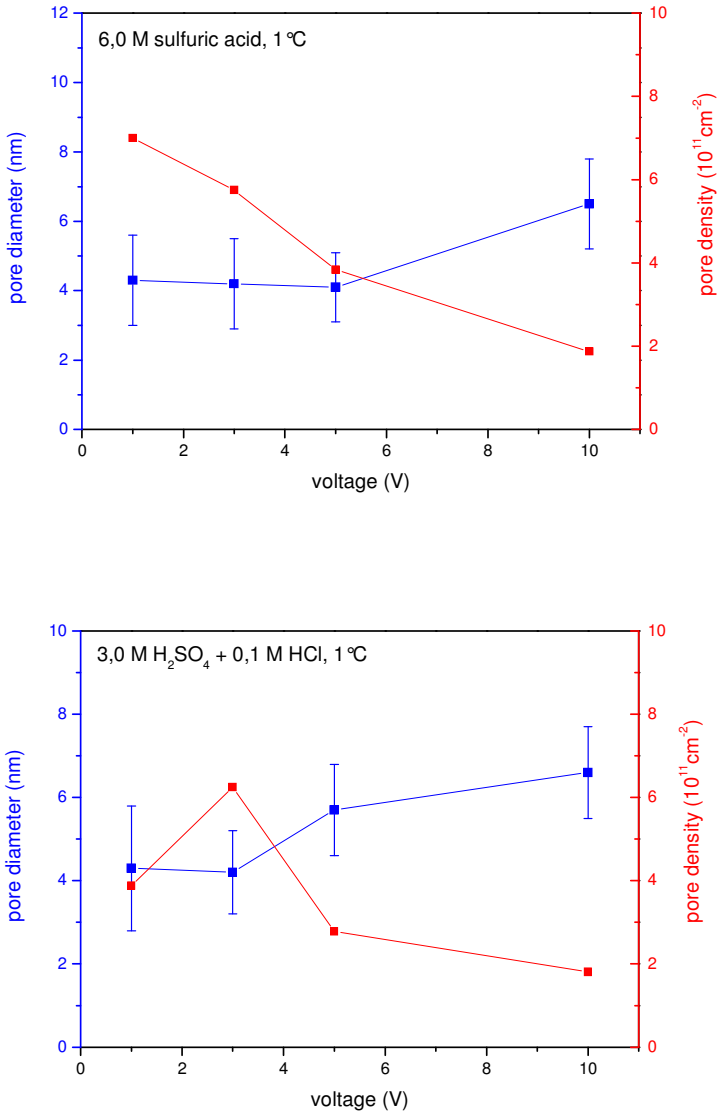


*Fig. I.13: Pore diameter and pore density variation versus the anodization voltage for different anodization acids.*

The results in fig I.13 show very well the effect of the increase of the concentration of sulphuric acid and the effect of the addition of hydrochloric acid.

The error bars for the pore diameter give the degree of homogeneity of the pore diameter distribution over the sample. A homogenous pore diameter distribution indicates a real equilibrium state during the anodization process and thus straight pores. The average pore diameter is important for further applications, as it determines the size of the nanochannels inside the PAA.

The density is namely important in respect to applications of PAA for high-density applications like of interconnectors, as mentioned above.

For 0.3 M sulphuric acid, the pore diameter distribution is considerable for small pore diameters (<10 nm). Although the average pore diameter still decreases for very low voltages, the distribution of the pore diameter is in the order of the pore diameter itself for diameters below 10 nm.This means that in this case, no steady anodization state with ordered, straight pores is attained, for there is no valuable equilibrium between the dissolution and formation process of alumina during the anodization process, but only random structures of oxidized Al at the surface of the sample.

For 6.0 M sulphuric acid, the pore diameter is increasing with increasing voltage and the pore diameter distribution does not depend on anodization voltages below 5 V. However, this pore distribution still remains much smaller than in the case of 0.3 M sulphuric acid. For very low voltages (from 1 V to 5 V), it is remarkable that the pore diameter is far smaller than in the case of the 0.3 M sulphuric acid, indicating the importance of the aggressiveness of the anodization solution for the realization of small pores.

Interestingly, for higher anodization voltages, the pore diameter is larger in case of the mixture of 6.0 M sulphuric with 0.1 M hydrochloric acid than in case of the pure 6.0 M sulphuric acid. However, in both cases the same minimum pore diameter is obtained. Although, with the addition of hydrochloric acid, well ordered PAA structures with pore diameters around 4 nm can be achieved, the variation of the pore diameter at 1 V is much higher than for pure sulphuric acid. This is also reflected by the pore density: the density decreases during the decrease of the voltage from 3 V to 1 V. This shows, that although some pores with a very small pore diameter have been created, also a high amount of pores of larger pore diameter has been created, which then results in a lower density of the pores, since the presence of large diameter pores reduces the number of pores per surface unit.

In contrast to this, the pore density increases continuously in the 6.0 M sulphuric acid with decreasing voltage. This indicates that the pore walls become thinner by lowering the voltage to very small values, as the variation of the pore diameter remains more or less constant during the variation of the voltage.

In summary, very high concentrated sulphuric acid seems to be the best adapted anodization solution for the fabrication of a high density and small pore diameter PAA.

The highest density of $7.0*10^{11}$ $cm^{-2}$ has been obtained at 1 V for 6.0 M sulphuric acid. However, the addition of hydrochloric acid allows to obtain very small pore diameter of about 4 nm with relatively thick pore walls, which could also be advantageous for applications as the pores are better insulated from each other.
Thus, from our study, solutions for different types of very small pore diameter PAA have been given and the smallest pore diameter so far reported for PAA has been obtained.

### I.3.4.3 Temperature influence on the on the PAA formation

Like the anodization acid, the anodization temperature plays an important role for the chemical processes like formation and etching of the alumina since the thermal energy is important for the specific reactions. Thus, it is namely important to study the fabrication of small pore diameter PAA for different temperatures. For this study, we have focused on anodization in 6.0 M sulphuric acid at 1 V, realizing every time a first anodization step of 60 min before realizing the second anodization step. The surface of PAA after the second anodization step is shown in Fig. I.14 .

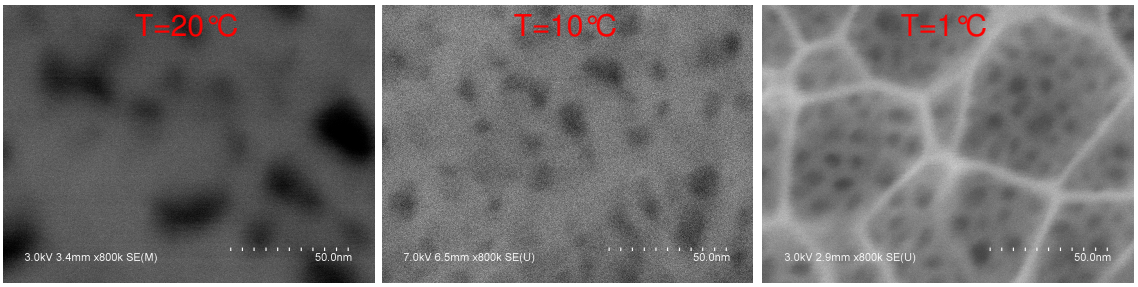


*Fig. I.14: SEM top view images of PAA showing the influence of the temperature T on the formation of PAA at very low voltage (1 V).*

Obviously, at 20 ℃, there is no ordered porous structure. Only at very low temperatures, a well ordered PAA structure can be obtained, This effect is surprisingly strong. In common anodization conditions, as demonstrated in I.3.3, the effect of the temperature does not influence very much the order of the porous structure if the first anodization has been sufficiently long. However, this strong effect of the temperature probably is due to the very high etching potential of the 6.0 M sulphuric acid. Thus, in order to get a porous structure by applying very low anodization potentials, the anodization conditions like the anodization acid and the anodization temperature have to be adjusted very precisely, as in this range, the

equilibrium between the formation and the dissolution of alumina is very critical and the low potential only slightly supports the field assisted dissolution and the field-driven diffusion of ions through the barrier layer to form alumina.
As a result of this section, the formation of very low pore diameter PAA in highly acidic anodization solution will be optimized at very low temperatures.

### I.3.5 The barrier layer

The barrier layer, as already described in I.1.2, is always present at the pore bottom of any PAA structure fabricated by anodization on Al. The thickness of the barrier $d_{b.l.}$layer is directly proportional to the applied anodization voltage:
$d_{b.l.}=k*U_{anod}$
with k depending on the anodization conditions. In oxalic acid at room temperature, k is about 1.4.
This barrier layer, consisting of alumina, separates the interior of the pores from the Al underlayer. As alumina is a highly resistive, hard material and acts as a diffusion barrier, the barrier layer insulates very well the interior of the pore from the Al underlayer.
Although the barrier layer therefore offers the advantage that materials deposited inside the pores are protected of the diffusion into the Al even at high temperatures, in the majority of applications, this barrier layer induces difficulties for the use of PAA in applications. The electric contact of nanoelements inside the pores with the substrate is highly resistive and therefore not adapted for device applications. For other applications, like the use of PAA as etching mask, the barrier layer hinders the direct access through the pores to the underlayers of the sample. Moreover, the thickness of the barrier layer varies statistically from one pore to the next all over the surface, so that the barrier for each pore is of slightly different thickness.
Thus, the control of the barrier layer, i.e. both the uniformity and the thickness, is very important for a multiplicity of applications. Thus, several approaches to remove or weaken the barrier layer have been studied elsewhere [38,39,40]. The mentioned methods are commonly the anodization on a conducting underlayer, usually Ti or Si, and the reduction of the anodization voltage at the end of an anodization in order to diminish the barrier layer thickness which is proportional to the applied anodization

voltage. One original method is also to inverse the anodization voltage at the end of the anodization in order to dissolve the alumina of the barrier layer [40]. However, all mentioned analysis of the removal of the barrier layer has so far not led to a technique which allows to obtain a uniform removal or thinning of the barrier layer. Thus, in this work, it was the defined goal to develop a method to obtain a reliable uniformity of a thin barrier layer at the pore bottom. This investigation was carried out by two different approaches: On the one hand, we have realized the anodization of Al which was deposited on a conducting layer in order to obtain pores which are open on the underlayer, on the other hand we have developed a special technique of a controlled voltage decrease at the end of the anodization, which leads to reliable and adjustable uniform thicknesses of the barrier layer.

#### I.3.5.1 Barrier layer removal: Anodization on a conducting underlayer

The anodization of Al deposited on a conducting underlayer offers the possibility to take the electrical contact from the conducting underlayer and thus to anodize the entire Al layer until the interface to the conducting underlayer is reached. Thus, when the Al is completely anodized and an electric field is always applied, the alumina at the pore bottom is dissolved until the conducting underlayer is in contact with the anodization solution. This leads to pores which terminate with open pore bottoms on the conducting underlayer.

However, this technique requires a very good control of the anodization process and a very attentive choice of the underlayer. During the anodization of Al to alumina, a volume expansion takes place and the adhesion of the alumina on the underlayer changes in comparison to the adhesion between the Al and the underlayer. Thus, the underlayer must have a very good adhesion to both materials, otherwise the PAA will peel off as soon as the entire Al sheet is anodized.

Besides, the anodization has to be stopped as soon as the underlayer is reached, as otherwise the entire surface of the underlayer will be oxidized which weakens again the adhesion of the PAA on this layer and by the way forms an oxide layer at the surface of the underlayer which then again forms an effective barrier layer between the interior of the pores and the sample.

In addition to the conventional underlayer materials Ti and Si, we have realized the anodization on TiN as underlayer, which is interesting for later applications, as TiN is

a well known conducting diffusion barrier layer for many materials and thus well adapted for different applications, e.g. for the CVD growth at higher temperatures with metal catalyst deposited on the TiN before growth (see also CVD growth described in chapter III)

We therefore have carried out the entire anodization of an Al sheet on underlayers of different materials. In the following, the results for Ti, TiN and Si as underlayer will be shown (Fig. I.15) and discussed.

a) $Al_2O_3$ on TiN

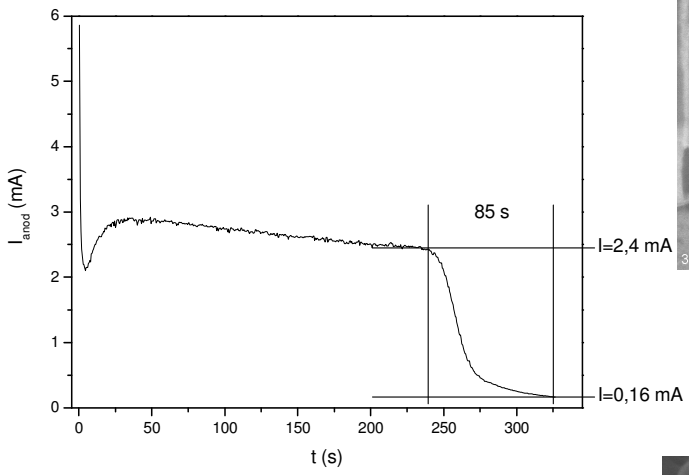


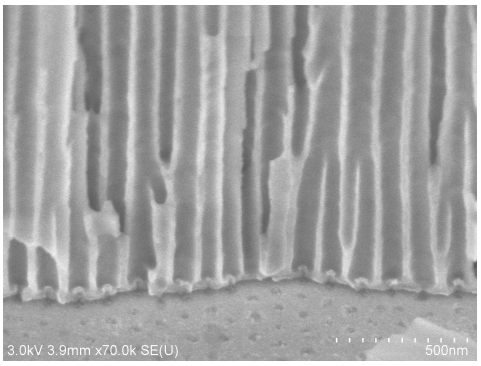


b) $Al_2O_3$ on Ti

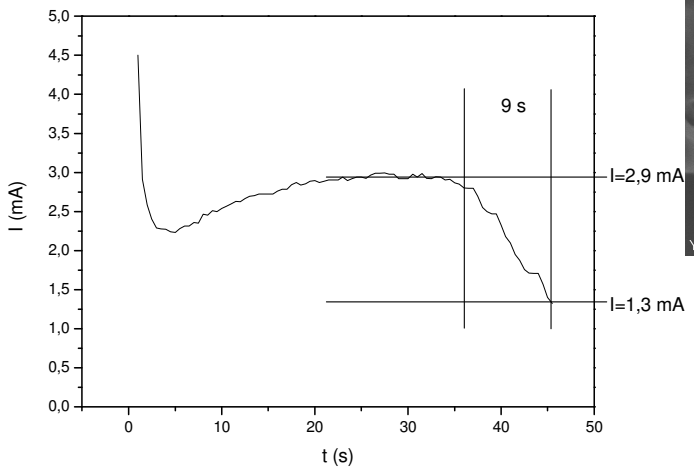


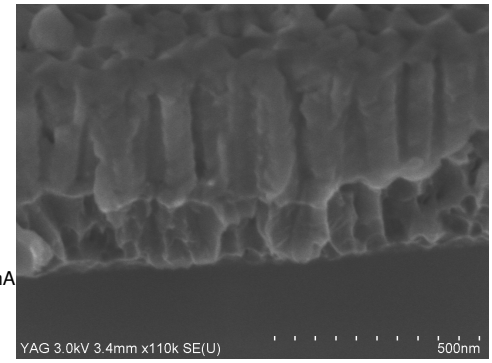

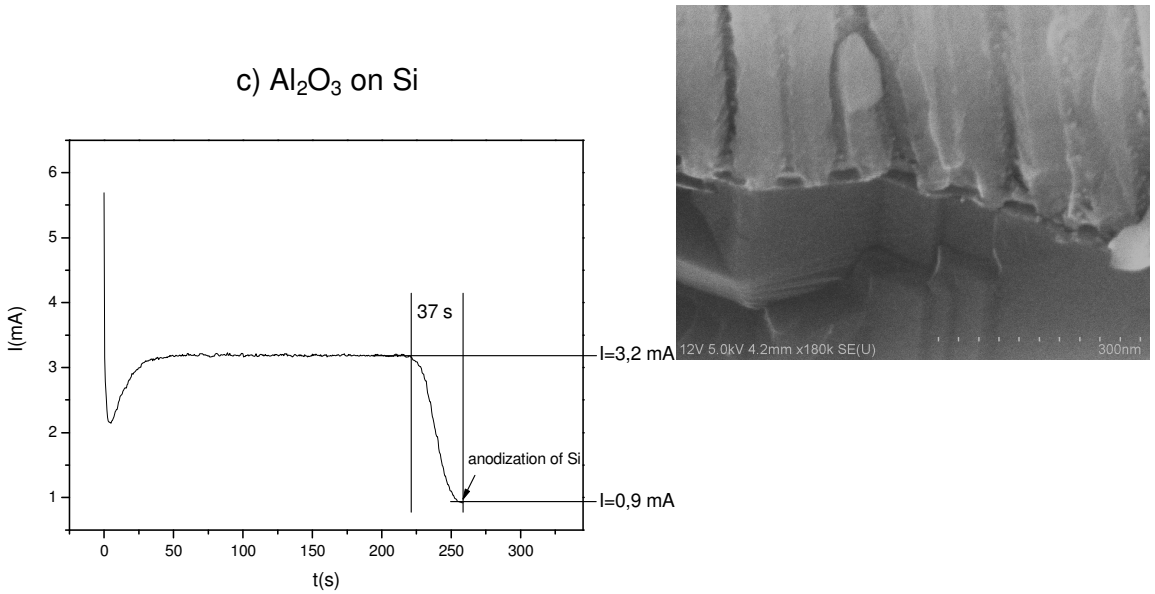


*Fig. I.15: PAA formed by a complete anodization of an Al layer deposited on a) TiN, b) Ti and c) Si. The SEM images show the facets of cleaved samples after the anodization.*

The graphs in Fig. I.15 show very well the anodization behaviour, especially when the pore walls start to touch the interface to the underlayer. In all different cases, there is a current breakdown at the end of the effective pore growth. However, there are important differences between the different underlayer materials.

In case of TiN and Si, the current decreases very strongly as soon as the interface is reached. In different series, we have observed that already at the very beginning of the current decrease, the pores touch the interface at the centre of the pore bottom. Thus, during the decrease, only the barrier layer is removed due to the field assisted dissolution and the remaining Al between the pore walls is oxidized. However, as soon as the gradient of the decrease becomes smaller, the anodization takes place very close to the surface and starts to oxidize the underlayer. The timing for finishing the anodization is very important and depends on the respective underlayer: if the anodization is stopped too early, there is still a thin barrier left at the pore bottom, if it is stopped too late, the membrane peels off from the underlayer or the underlayer is oxidized. We have found, that the only reliable technique to stop the anodization at the ideal moment is to calibrate the percentage of the constant anodization current (the current at the plateau of the I(t) curve) at which the pores are well open on the underlayer and to stop the anodization as soon as this current limit is reached.

Consequently, the current limit is a fixed percentage of the constant anodization current and specific for each underlayer.

In case of Ti, no behaviour like of TiN and Si could be observed. In contrast, there was no real current breakdown, after a strong first decrease (shown in Fig. I.15 b), the current continuously decreased very slowly. The possible result can be observed in the SEM image: as Ti is a very easily oxidizing material, the anodization continues inside the Ti, and the Ti itself is oxidized, reflected by the rough facet seen in the SEM image. The stronger current decrease at the beginning (shown in Fig. I.15 b) is due to the crossing of the interface and the change of the anodized material. Thus, in case of Ti as underlayer, we have not been able to fabricate PAA with open pores on Ti without oxidizing the Ti.

This has been different for both TiN and Si, in both cases the anodization could be stopped right at the interface after the respective calibration described above. However, the pore bottom in both cases is strongly different: On Si, really open pores can be obtained; on TiN, there are voids formed at the pore bottom and the curvature of the pore bottom becomes inversed. This problem could not be solved by longer anodization, in this case the PAA peeled off from the TiN.

Thus, only with PAA on Si, we have been able to open the pores in a way that the underlayer can be directly reached from the interior of the pores without an additional alumina barrier. However, as it will be shown in chapter II, even with a very precise calibration of the current limit at which the anodization is stopped, the Si is slightly oxidized at the pore bottom, which again hinders the direct access to the underlayer from the pores.

To summarize, we have been able to fabricate PAA by anodizing entirely the Al deposited on various underlayers. However, in all cases, it is not possible to create pores which are open on a conducting layer, as either the alumina at the pore bottom is not completely dissolved or the conducting underlayer is oxidized immediately as soon as the pores are open on the underlayer.

#### I.3.5.2 Barrier layer thinning by an exponential voltage decrease

A very interesting alternative to the anodization on a conducting underlayer to remove or to thin the barrier layer is the controlled voltage decrease at the end of the anodization. With this technique, a constant anodization voltage is applied during the

PAA formation and thus determines the main parameters of the PAA, and at the end of the anodization process, the voltage is decreased in order to thin the barrier layer. For the thickness of the oxide at the pore bottom, i.e. the barrier layer, depends on the applied potential, an effective barrier layer thinning takes place and the final thickness of the barrier layer is proportional to the final anodization voltage. However, this decrease cannot be carried out under any conditions.

Generally, the voltage change at the end of the anodization process does not only influence the barrier layer at the pore bottom, but also the pore size, cell size and thus the pore density. Thus, at each step, during the voltage decrease, a new equilibrium state is established with a corresponding specific pore density, a specific anodization current and a specific barrier layer thickness, so that a new porous structure is formed at the pore bottom forming branches with multiple junctions. This effect has already been used for the formation of Y-junctions at the pore bottom and led to interesting PAA structures [41,42], but in general this effect is not desirable as thus, the pore diameter changes and the pores are not straight anymore.

The effect of branching can be suppressed if the voltage decrease is carried out very fast. But, in this case, the decrease can easily become too fast in terms that the thickness of the barrier varies slower than the voltage. This means that the equilibrium state of growth and dissolution, which is self-adjusted in respect of the barrier layer thickness, the anodization acid and temperature and the voltage, cannot be adapted fast enough to the voltage change. Thus, the anodization stops completely during the voltage decrease and the barrier layer thickness corresponds to the anodization voltage at which the effective anodization has been stopped.

Thus, the rate of the voltage decrease must be adapted precisely to the respective anodization conditions in order to continue the anodization until the end of the decrease and to avoid a strongly branched pore structure at the pore bottom. In the literature, some deeper investigations on the behaviour of the anodization current and the branching have been mentioned [43], but so far no systematic study on the function of the voltage decrease has been done which allows to control the uniformity and thickness of the barrier layer at the end of this voltage decrease. The goal in this work was therefore to investigate the anodization current response on the voltage decrease and to establish a voltage decrease function which allows to obtain reliable results on the final barrier layer characteristics. This investigation has been done in oxalic acid at 25 °C after a constant voltage anodization at 40 V.

In preliminary experiments, the response of the anodization current on a stepwise anodization voltage decrease was investigated (Fig. I.16). During this decrease, the voltage has always been changed instantly and then kept constant during this step until it was again decreased instantly down to the value of the next voltage step.

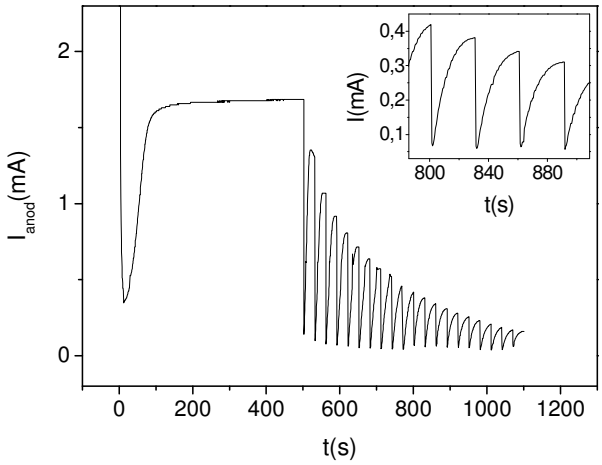


*Fig. I.16: Anodization current during a stepwise anodization voltage decrease.*

After each voltage change, the current first decreases strongly, but then increases until a new equilibrium state is reached. This leads to branched structures shown in Fig. I.17.

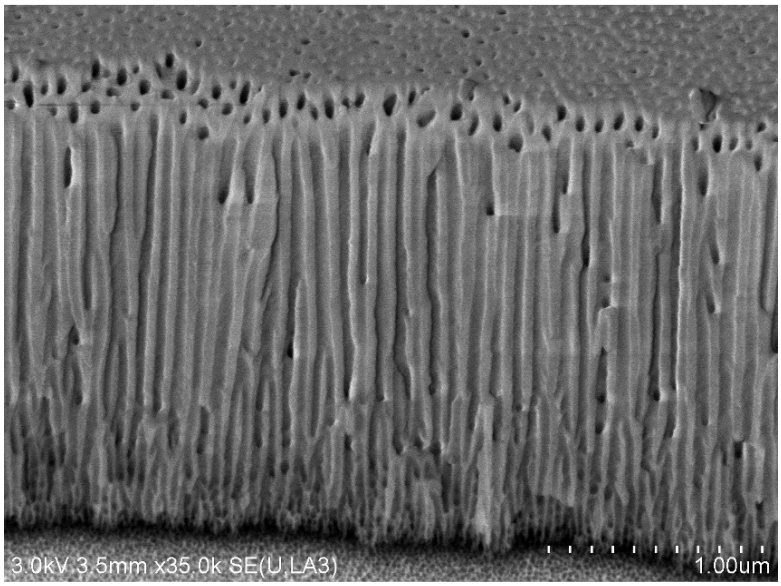


*Fig. I.17: Branched pore bottom after a slow, stepwise voltage decrease.*

In a first series of experiments, the stepwise voltage decrease was smoothened by applying a continuously decreasing function, in order to avoid discrete constant voltage drops. Since the barrier layer thickness and thus the resistance of the electrical circuit is proportional to the applied anodization voltage, the voltage decrease at any particular time should always be proportional to the previously applied voltage. This can be expressed by an exponential decrease function:

$dU/dt = \text{const} \times U \quad \Rightarrow \quad U = U_0 \exp(-\eta t) + U'$

In this function, there are three parameters to be determined: $U_0$, U' and η. While $U_0$ and U' determine the shape of the function in general, and thus depend on the anodization conditions, the time constant η gives the rate of the voltage decrease. The higher the η value, the higher the decreasing rate. Therefore, first $U_0$ and U' of the function must be determined in a way, that the current response follows the voltage response (i.e. ideally is exponential as well), and then, with the time constant η, the rate of the decrease can be adjusted which also influences the pore structure at the pore bottom.

Therefore, first of all, we have determined the parameters $U_0$ and U'. We have decreased manually the anodization voltage down to a final value by observing the anodization current, while we have tried to keep the anodization current in an exponential decay. Then, for the optimization, we have fitted the obtained voltage

values with an exponential voltage decay function and realized an anodization with this smooth exponential voltage decay function.

The voltage-time graph and the current-time graph are shown in Fig. I.18.

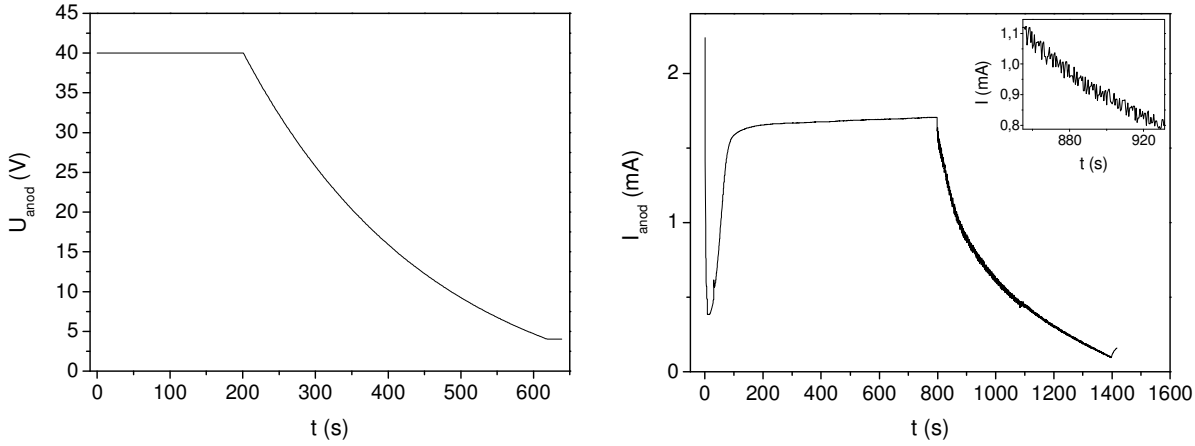


*Fig. I.18: Current-time and voltage-time graph during the voltage decay (anodization in 0.3 M oxalic acid at 24 °C).*

Obviously, the anodization current follows perfectly well the exponential decay of the decreasing voltage. The zoom in the inset shows, that during the decay, the current decreases more or less smooth, which indicates that the anodization process is in permanent non-equilibrium during the decrease and thus indicates the continuous thinning of the barrier layer, which is continuously adapted to smaller thicknesses in order to correspond to the new anodization state. At the end of the voltage decrease, the voltage was kept constant for 20 s. This allows to observe if the anodization has followed the voltage decrease down to the end: if the anodization current increases during these last 20 s at the final lowest anodization voltage, it indicates that still the anodization takes place and that the anodization has been in steady non-equilibrium until the end of the decrease. At the final constant voltage step, the anodization current increases like after each voltage step in Fig. I.16 in order to reach the equilibrium state corresponding to the final anodization voltage. At the beginning of this constant final voltage step, the barrier layer is thicker than in the equilibrium state corresponding to the final anodization voltage, and during the current increase, the thickness of the barrier layer approaches to the thickness corresponding to the equilibrium state corresponding to this final voltage

In order to optimize the values $U_0$ and U', we have varied these values around the fitted ones and carried out the anodization with these different decrease functions at very high decreasing rates, i.e. with very high η. In this optimization, the values for $U_0$ and U' should be determined in a way, that the voltage can be decreased as fast as possible with the anodization current following the decrease as long as possible. In other words, with the optimized function, the voltage is decreased in a way, that the anodization is never in an equilibrium state but allowing the system enough time to adapt to the voltage decrease so that the anodization is not stopped early during the decrease due to a barrier layer which is too thick for the applied voltage. The results of this optimization are reported in Fig. I.19. In this experiment, the voltage has been decreased very fast and we have observed at which voltage the anodization process stopped, i.e. at which voltage the anodization current became zero. The optimized function should allow to reach very fast very low stopping voltages.

The four exponential functions (exp1-4) shown in Fig. I.19 contain the following values for $U_0$ and U':

| | exp1 | exp2 | exp3 | exp4 |
|---|---|---|---|---|
| $U_0$/V | 58,5 | 45 | 50 | 53 |
| U'/V | -18,5 | -5 | -10 | -13 |

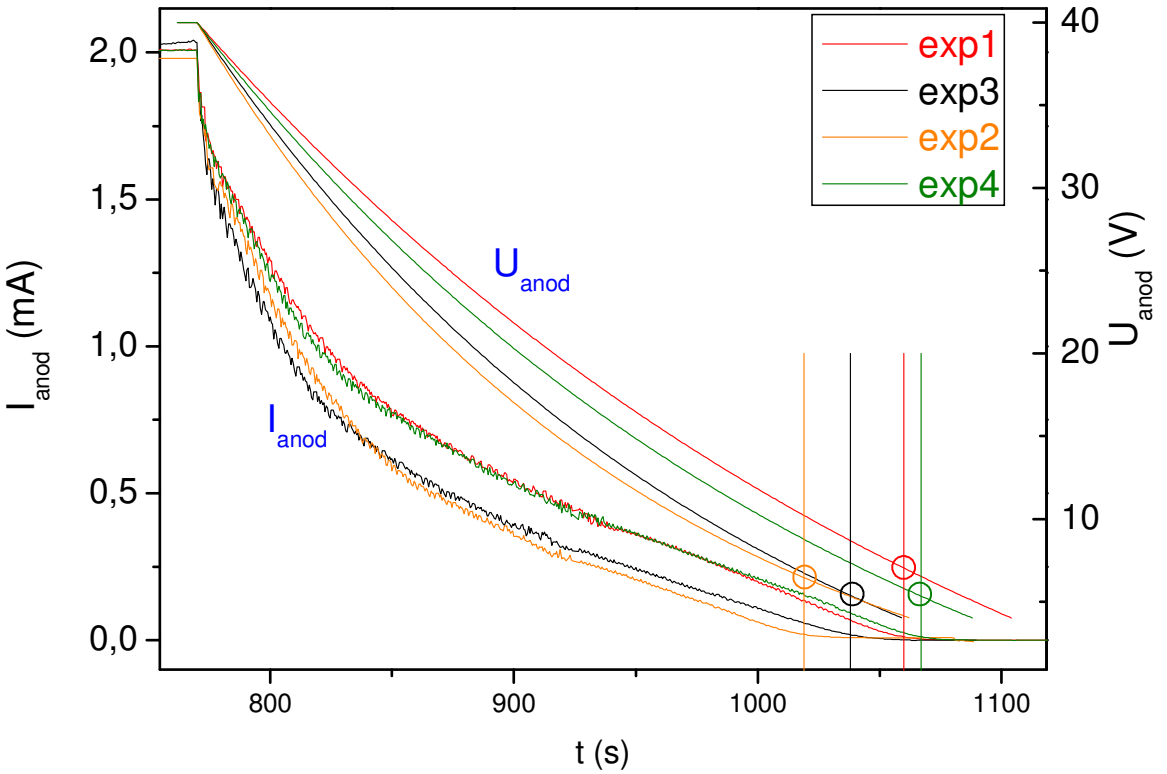


*Fig. I.19: Current- and voltage versus time graphs of the voltage decrease at the end of the anodization for different exponential functions. The circles indicate the voltage values for which the current becomes zero.*

In case of the functions exp1 and exp4, due to the high value of $U_0$ (which is multiplied with the exponential factor), the current decrease is very strong at the beginning and then becomes very smooth. This means, that in this case, after a high current drop at the beginning, the decrease becomes very slow and a lot of branches are formed at the pore bottom.

For smaller $U_0$ values, the decrease is faster, especially at the beginning of the decrease but the anodization is cut early (at high voltages) if $U_0$ is too low (exp2). Exp3 has therefore been determined as the ideal decrease function: The anodization stops at the lowest voltage (5.2 V) after a short decrease of 1035 s. The other functions either lead to a slower decrease at slightly higher stopping voltages (exp4) or to a fast decrease with far higher stopping voltage (exp2) or to a slower decrease with higher stopping voltage (exp1).

Thus, for the further investigation of the influence of η, the function exp3 has been used as optimized function. The effect of the time constant η is shown in Fig. I.20.

Here, the anodization current is reported for different time constants η, where for each described voltage decrease, starting from 40 V, the voltage has been decreased following the function exp3 with different η and finishing at final voltages of 5 V. The final voltage of 5 V has been fixed for each anodization for 20 s, and the current increase, which gives information about the state of the anodization, i.e. about if the anodization has followed the voltage decrease until the end, is reported in a zoom for each current-time graph on the right side in the Fig. I.20.

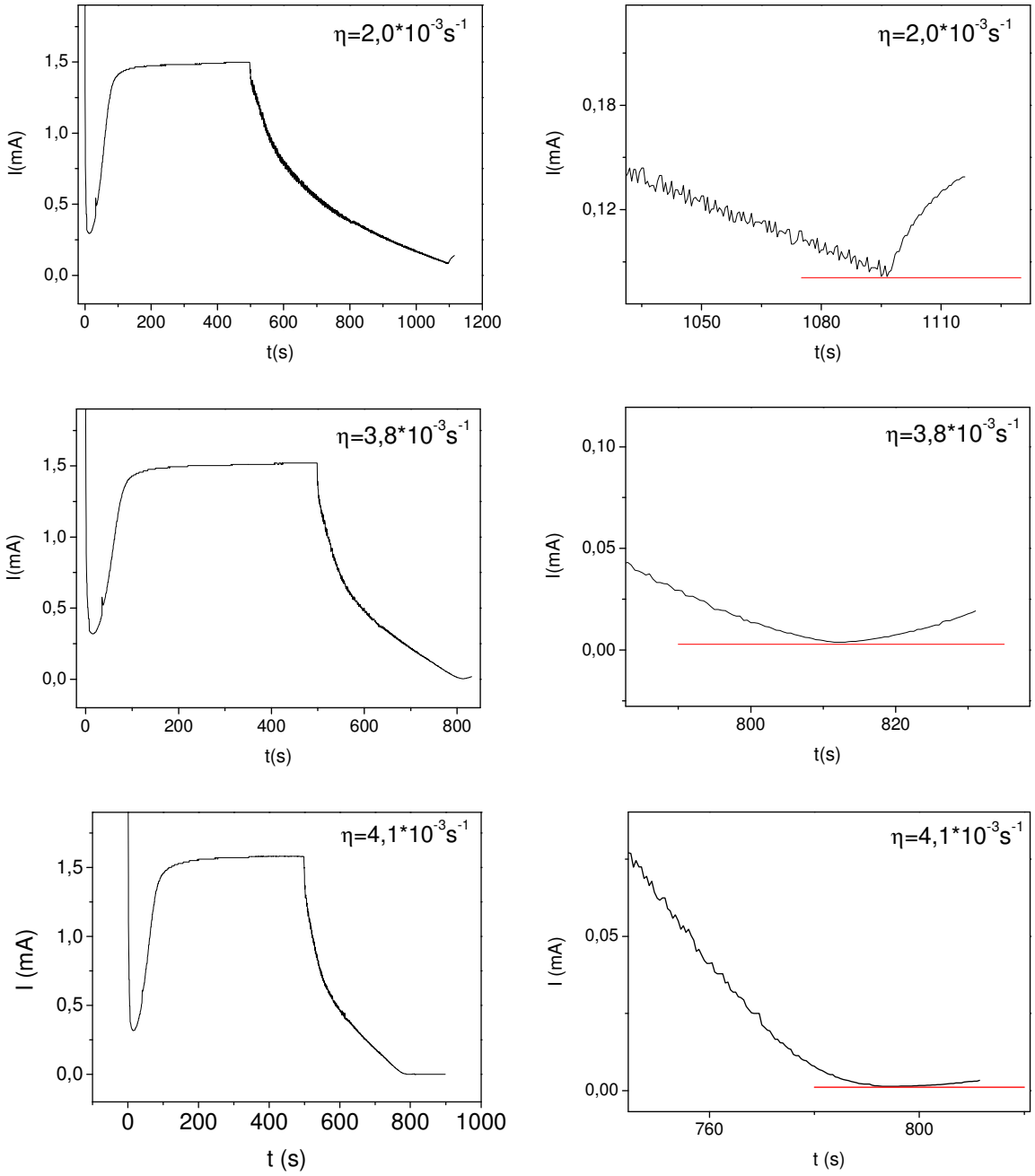


*Fig. I.20: Influence of the time constant η on the current response.*

From the current graphs, it can clearly be seen that with increasing η, the anodization becomes closer to the limit of the decrease rate: the current increase during the constant final voltage step becomes lower with higher η indicating that the difference between the real barrier layer thickness at the beginning of the constant final voltage step and the barrier layer thickness corresponding to the equilibrium state of the final anodization voltage increases with higher η. For $\eta=3.1*10^{-3}\ s^{-1}$, the current nearly does not increase anymore during the 20 s of constant final voltage anodization. However, the fact, that the current still increases, shows that the barrier layer has been thinned until the end of the voltage decrease.

With the optimized voltage decrease function and the variation of η, the barrier layer can thus be thinned to very small thicknesses with different formation of branches at the pore bottom. At this point, it should be mentioned that the thickness of the barrier layer, of course, depends on the final anodization voltage $U_{anod}$ ($d_{b.l.}$ ~ 1.4 x $U_{anod}$ nm/V) and the branching depends on the decrease rate, i.e. the time constant η. In Fig. I.21, the influence of η on the branching at the pore bottom is demonstrated. Both samples have been prepared like in the Fig. I.20, thus at 40 V constant anodization voltage for the pore growth and the final voltage of 5 V.

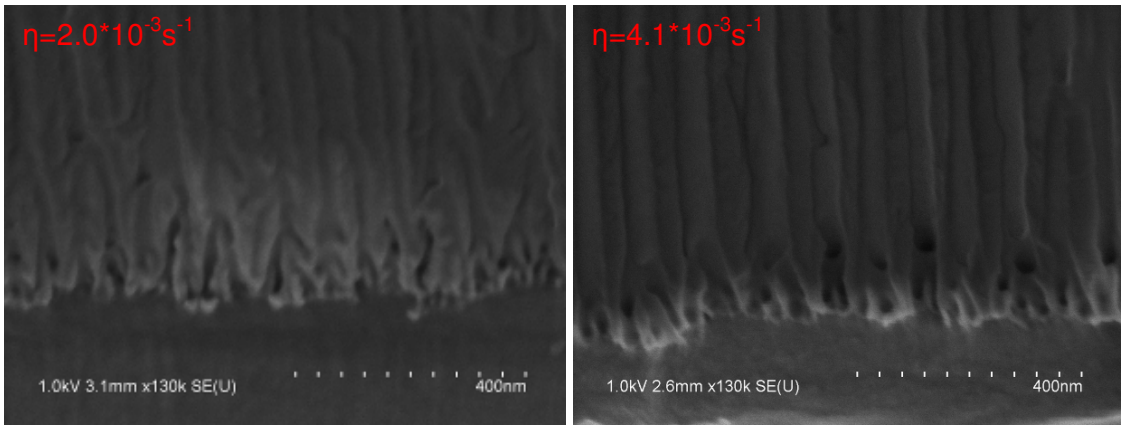


*Fig. I.21: Influence of η on the pore bottom for two η values.*

As already mentioned, the thickness of the barrier layer is not uniform over the sample, but varies slightly statistically over the sample. The thickness at the end of the voltage decrease thus can vary as well. Usually, in case of an anodization in the equilibrium state, the barrier layer thickness variation is proportional to the average thickness. However, this effect can vary in case of the non-equilibrium voltage decrease: in this case, the variation of the barrier layer thickness at the beginning of

the voltage decrease can become important during the decrease, as the anodization is stopped during the decrease as soon as the anodization voltage is too low to overcome the barrier layer, i.e. as soon as the barrier layer is not thinned fast enough during a fast voltage decrease. Thus, if the decrease is carried out close to the fastest limit (like for $\eta=4.1*10^{-3}s^{-1}$), the variation of the barrier layer thickness at the end of the voltage decrease might not be proportional to the average thickness after the thinning process, but higher. This effect has been studied in this work in correlation to the electrodeposition behaviour and will be discussed in chapter II.3.

## I.4 Conclusion

In this chapter, the principles of the formation of PAA have been presented and the investigations, based on the knowledge of these principles, have been shown.

The main investigations in this work concerning the PAA have been realized in respect to future applications, like the use of PAA as etching mask, as support for later electrodeposition or as support for other nanomaterials, preferentially with the goal to realize future device applications.

Therefore, we have studied precisely the growth rate of PAA in order to be able to predict exactly the thickness of PAA, which is important for any kind of application of PAA. In this study, we have observed that the formation rate is not linear from the beginning of the anodization process and that the formation rate depends strongly on the anodization conditions. In order to predict the thickness of PAA, the thickness of PAA can only be deduced from calibration graphs like shown in Fig. I.6-I.8.

Besides, we have shown that the best way to obtain a good ordered PAA structure in thin Al layers is the anodization in two steps at low temperature (T= 1°C). This is the starting point for the development of etching masks based on PAA, which is presented in chapter IV.

Namely in respect to further applications, we have tried to push the pore diameters of PAA to the lowest possible values and to the highest possible pore densities. It has been proven that for this application, the use of highly concentrated acids, namely sulphuric acid, is important. By using 6.0 M sulphuric acid at 1 °C, we have demonstrated the so far lowest realized pore diameter for PAA of about 4.2 nm and a pore density of about $7.2*10^{11}cm^2$.

For a multiplicity of applications, it is important to reduce the barrier layer thickness at the pore bottom as much as possible without creating a branched porous structure at the pore bottom. We have developed a sophisticated voltage decrease function with which the voltage can be decreased in a wide range of decreasing rates down to very low voltages (like down to 4 V, see also paragraph II.3.2) in order to obtain very thin barrier layer thicknesses, which offers new possibilities for device realizations by PAA. The optimized exponential function exp3 developed in paragraph I.3.5.2 has been used in the following work for the voltage decrease.

Thus, with the results given in this chapter, the bases of a variety of improvements of the use of PAA for nanoelements is given.

# CHAPTER II:

# ELECTRODEPOSITION INSIDE PAA

# II. Electrodeposition inside PAA

## II.1 Introduction

Since the early beginning of the investigations of ordered PAA, the electrodeposition has been applied in order to fill the pores of the PAA [44,45]. The electrodeposition offers a very simple method to fill PAA with a multiplicity of different materials. The only request for these materials for the possible deposition by electrodeposition is to be soluble in a solution which does not etch PAA and to form ions which can be deposited inside the PAA by applying a deposition voltage. This allows to form nanomaterials inside PAA whose physical shape is determined by the pore diameter of the PAA, if the pores are filled during electrodeposition in their complete diameter. By varying the main parameters of the PAA, the shape of the nanoelements can thus be adjusted at whish.

Since the PAA is always deposited on conducting Al, the electrodeposition inside PAA can be done by simply applying the deposition potential on the Al which already served as contacting electrode for the anodization. Therefore, the electrodeposition is the consequent electrochemical method which can be used easily after the preparation of the PAA by anodization in the electrochemical anodization bath.

Today, the electrodeposition has been realized in PAA with different materials of different shapes. To give some examples, the ordered deposition of ZnO nanotubes [46], growth catalysts [47,48,49] and different metallic and semiconducting nanowires [50,51] have been realized by electrodeposition.

However, the electrodeposition inside PAA is also a challenging subject for several reasons: the electrical contact taken from the Al at the back of the pores still shows the resistance of the barrier layer which influences the deposition potential, the very high aspect ratio of the pores requires a high mobility and a high concentration of the ions, and finally the deposition in the nm range has to be controlled very precisely.

These challenges have been the subject of this work. The defined goal hereby has been the development of a reliable electrodeposition method, which allows to control the density of filled pores and the amount of deposited material precisely.

# II.2 The electrodeposition method

## II.2.1 The electrodeposition: principles

The electrodeposition of metal is based on the reduction of metal ions ($Me^{z+}$), which are dissolved in an electrolyte, at the surface of the sample, with the following principle reaction:

$Me^{z+}+z^*e^- \leftrightarrow Me$

This reaction from left to right corresponds to the reduction, i.e. electrodeposition, whereas from right to left it corresponds to the oxidation of the metal. The current density for the reducing reaction is called “cathodic current” $j_c$, since the sample surface acts as a cathode, and the oxidation reaction current density is called “anodic current” $j_a$. The ratio between these two currents is mainly determined by the applied potential. Both currents are equal if the Nernst potential is applied on the sample:

$$E_{Nernst} = \frac{RT}{zF} \ln \frac{a_{Me^{z+}}}{a_{Me}}$$

with $a_{Me^{z+}}$ is the chemical activity of the metal ions in the electrolyte

$a_{Me}$ is the chemical activity of the metal at the electrode

*R* is the universal gas constant

*F* is the Faraday constant

*T* is the absolute temperature

An electrodeposition of the metal takes place if an overpotential, i.e. a potential higher than the Nernst potential, is applied to the electrode. This is the case of a perfectly conducting electrode; in case of a resistive electrode, there is a potential drop at the electrode which reduces the effective applied potential for the reduction of the metal ions. Thus, the potential must be adapted to a potential that is sufficiently higher than the Nernst potential for the specific metal.

The deposition is generally realized in the three electrode configuration: The sample is used as cathode, a counter electrode works as anode and a third reference electrode serves as reference for the applied deposition potential. The reference electrode is contacted via a very high resistive voltmeter, so that there is a negligible current flowing through the reference electrode. Thus, the reference electrode

defines a standard potential (e.g. the Ag/AgCl redox potential), to which all applied electrodeposition potentials are referred. Generally, the reference electrode is connected via a salt bridge with the electrolyte, through which no current passes. However, in this configuration, there is still a resistance between the cathode and the reference electrode due to the resistivity of the electrolyte. It is therefore important to position the salt bridge as close as possible to the cathode, and in order to be able to compare the electrodeposition of different samples, the position of the salt bridge in relation to the cathode should always be constant and close to the cathode.
The reference electrode is very important for any electrodeposition, as all potentials in an electrochemical bath depend on the respective interfaces. Thus, only the standard potential of a reference electrode can give a fixed value to which the applied electrodeposition potential can be adjusted. Consequently, the reference electrode allows to apply a reproducible relative potential to the sample.

In general, the electrodeposition is carried out either in potentiostatic or galvanostatic mode. In potentiostatic mode, the electrodeposition is done under given electrodeposition potential, in galvanostatic mode, under fixed electrodeposition current. The galvanostatic mode allows the constant reduction of ions at the cathode, but makes it difficult to control the electrodeposition precisely, as the deposition potential is freely adjusted. Thus, the reduction of any species can take place at the cathode: e.g. after the deposition and thus desaturation of the metal in a solution close to the surface of the cathode, hydrogen can be reduced, forming $H_2$. This will need a high deposition potential, but, since in galvanostatic mode only the current is observed, this higher potential will be automatically chosen.
Thus, in this work, we have always been working in potentiostatic mode.

### II.2.2 Electrodeposition inside PAA: state of the art

The electrodeposition inside PAA implies the electrodeposition on an insulating layer covering the electrode: The resistivity of alumina being approximately $1*10^{12}$ Ω cm, the barrier layer at the pore bottom, which protects the Al from the electrolyte and which has a thickness depending on the voltage (the thickness is given by about $1.3nm/V*U_{anod}$), is a very good insulator.

There are two main approaches in order to overcome this problem given by the insulating barrier layer.

- The first approach consists in the separation of the PAA from the Al by dissolving the Al, the etching of the barrier layer and the subsequent deposition of metal on one facet of the both-side-open-pored PAA or a subsequent mounting of the PAA on a conducting sample [52,53,54]. In this setup, a uniform electrodeposition can be achieved by applying a DC deposition voltage. However, this technique implies the disadvantage of a complex handling of the separated PAA and therefore is not suited for the reliable and easy fabrication of devices.
- The second approach consists in the direct deposition on the barrier layer at the pore bottom. This is the one we follow in this work. Generally, this deposition is carried out under a high overpotential in order to overcome the resistance of the barrier layer. This technique has first been described by Caboni [55], who applied an AC potential for the electrodeposition on porous alumina. The electrodeposition via the AC potential is possible due to the property of the alumina, that is situated on the aluminum, as valve metal [56] which preferentially conducts the current in cathodic direction. The AC deposition under high overpotential has been shown to offer several advantages in comparison to a high-potential DC deposition: In case of the AC deposition, the alumina of the barrier layer, which acts as a dielectric of a capacitor during the application of the high potential, can be discharged and the density of the metal ions in the electrolyte close to the pore bottom is less unsaturated than in the case of the DC electrodeposition. Therefore, the AC electrodeposition inside PAA has been widely investigated [57,58,59]. However, the AC deposition shows some disadvantages: during the positive (potential) half-cycle, some deposited metal is oxidized and there is no delay time giving enough time for the ions after the negative (potential) cycle to diffuse to the pore bottom and thus to maintain always the same ion density at the pore bottom. Therefore, it is difficult to control the deposition rate precisely.

In 2000, Nielsch et al. showed a very uniform deposition of Ni inside PAA by applying a pulsed electrodeposition [60]. They extended this approach to more sophisticated applications [61,62]. In this technique, the AC deposition is replaced by pulses; preferentially, a high negative voltage pulse is followed by a low positive one in order to discharge the barrier layer and finally followed by a delay time in order to assure a constant ion density at the pore bottom. The pulsed electrodeposition has been applied by many other groups [63,64,65,66], showing its potential for a homogenous and controllable deposition.

One crucial effect of the pulsed electrodeposition in all mentioned publications is the high overpotential applied during the electrodeposition. In order to understand the necessity of this high potential (which must also be applied during an AC deposition), the basic electric circuit of the electrodeposition is referred (Fig. II.1).

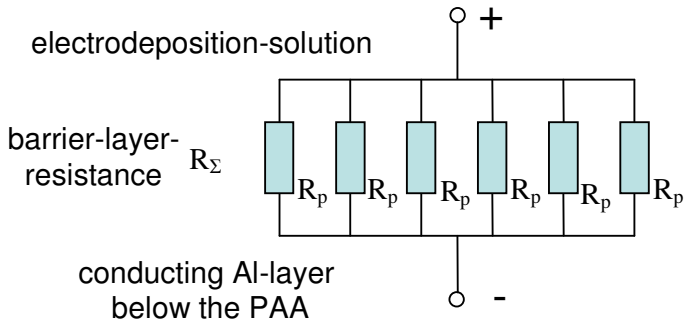


$$R_\Sigma = \left( \Sigma \frac{1}{R_p} \right)^{-1}$$

*Fig. II.1: Basic electric circuit for the electrodeposition*.

Although the resistance $R_p$ of the barrier layer at the pore bottom of each pore is very high, the effective resistance $R_\Sigma$ of a PAA sample is drastically reduced due to the parallel connection of all pores of the PAA structure via the conducting Al layer under the PAA [67]. The parallel connection of the pores in the PAA sample thus is a main property of the PAA electrodeposition.

This implies that, if there is a variation in the parallel connected resistances of the barrier layer at the pore bottoms, the current will mainly pass through those pores which show the lowest resistance. If the potential thus is chosen close to the reduction potential, the deposition will only take place in those pores who exhibit the lowest barrier layer thickness. Only if a very high potential is applied, the resistance of the barrier layer in all pores can be overcome and a homogenous deposition can take place: In those pores in which the barrier layer is thinner, the initial higher current extracts fast the ions from the electrolyte causing an increased resistance in the electrolyte in these pores, which compensates the higher resistance of the thicker barrier layer in other pores. The high deposition potential thus is important for the homogenous deposition. If the barrier layer is thinned by a thinning process at the end of the anodization, e.g. by an anodization voltage decrease (see chapter I) or a wet etching, the potential can be reduced as well. This technique generally has been applied in all above cited publications in order to reduce the necessary value of the deposition potential. However, in all cases, still a strong relative overpotential is

applied, which makes difficult the realization and the control of very low deposition rate, like it is necessary for the deposition of particles with diameters of only a few nm.

### II.2.3 The research on the electrodeposition in this work

The principle goal of our work is to achieve a very good control of the electrodeposition of metal inside PAA in order to pave the way for the research on devices based on PAA. Both for the deposition of catalyst for a subsequent CVD growth of nanoobjects like CNTs or SiNWs and for the direct growth of nanowires inside PAA, the control of the electrodeposition inside PAA is of fundamental necessity.

The investigations first have been focused on the homogenous electrodeposition inside PAA. This work principally has been done by following the pulsed electrodeposition method which has been introduced in the previous section. In this respect, we have developed a PAA preparation and deposition method which allows us to vary the barrier layer thickness and to reduce the variation of the barrier layer thickness over the sample before the electrodeposition. Thus, we have been able to realize a homogenous electrodeposition on different barrier layer thicknesses by only applying a low overpotential. For this investigation, we have realized a barrier layer thinning like described in chapter I, following at the end of the anodization the optimized exponential function for the voltage decrease. By this technique, we were also able to assure a very precise control of the deposition rate in order to achieve a reliable deposition of very small metal catalyst particles inside PAA. We finally have been able to realize a very well homogenous deposition of metal catalysts inside PAA with a particle size down to about 10 nm.

In order to enhance the field of application of the filled PAA samples, we also developed a method to vary the density of the filled pores of the PAA. This has been realized by a new and unique approach, for which we realized a low-overpotential electrodeposition on samples that had been prepared by varying the voltage decrease function which allowed us to control the deposition density in a wide range. Finally, we also investigated the electrodeposition on conducting layers by realizing the electrodeposition on samples which showed a PAA structure with open pores directly on the underlayer.

# II.3 Results and discussion

## II.3.1 The electrodeposition setup

The electrodeposition has been done by using the sample-holders that also had been used for the anodization process. Thus, the sample could be directly transferred to the electrodeposition setup without taking it out of the sample holder. Thus, leakage problems at the interface “Al-alumina-oring” of the sampleholder and pollution of the sample were reduced to a minimum.

For the electrodeposition, a three electrode setup has been used. An Ag/AgCl electrode has been used as reference electrode, and the counter electrode was realized by a graphite sheet.

The electrodeposition setup was a commercial HEKRA PG310 setup. As driving programme, the POTPULSE programme created by HEKRA was used.

The setup has always been used in the potentiostatic mode. This allows a better control of the electrodeposition for the deposition potential is fixed and thus only ions with a reduction potential under the deposition potential can create the electrodeposition current.

For all electrodeposition, the distance between the sample and the reference electrode has been fixed to 2 cm. Due to the geometric shape of the sample-holder and the setup, this distance could not be further reduced. However, this distance has been kept constant for all samples in order to guarantee the best reliable results and to keep the resistance between the reference electrode and the sample as constant as possible. Besides, for all samples, before starting the electrodeposition, the OCP (open circuit potential) was measured, which indicates the potential applied at the sample for which there is no current passing through the sample. For a series of samples, we assured an identical initial OCP in order to start from equal conditions, i.e. equal interface potentials of the interface sample-electrolyte.

The investigations of the electrodeposition have mainly been carried out using the Watts Bath as electrolyte for the Ni deposition. The Watts Bath is a mixture of 300 g/l $NiSO_4$, 45 g/l $NiCl_2$ and 45 g/l $H_3BO_3$ dissolved in water and has been used for more than a century for galvanic deposition of Ni. The important characteristics of the Watts Bath are the high concentration of Ni (~ 1.3 M) and the ph of about 3.2 and the non-alumina-etching behaviour of the boric acid.

Besides, in this work also electrodeposition of Fe, Co and Cu have been realized for different applications. However, as the investigations on the electrodeposition have been done using the Watts Bath and depositing Ni, mainly this deposition is referred in the following chapters.

### II.3.2 Uniform electrodeposition inside PAA

For all samples, before the electrodeposition, the barrier layer has been thinned by an anodization voltage decrease at the end of the anodization, following an exponential function described in I.3.5.2, thus starting from the constant anodization voltage of 40 V. In addition, all samples have been etched for 25 min in 0.3 M $H_3PO_4$ at 30 °C. Without thinning the barrier layer, we have not been able to obtain any deposition inside the pores at any deposition potential.

The pulses of the electrodeposition have been fixed at 5 ms at the negative potential, followed by a delay time of 90 ms. We could observe, that under these conditions, perfectly homogenous deposition could be achieved. The sequence of the 5 ms pulse and the 90 ms delay time is in the following called “sweep”.

With the optimized decrease function exp3 described in I.3.5.2, by controlling the final anodization voltage, the final barrier layer thickness can be adjusted down to very small values. In order to obtain a very uniform dispersion of the barrier layer thickness, we have chosen a very slow decrease function with $\eta=2.0*10^{-3}s^{-1}$. Thus, we could assure that the anodization was always in the equilibrium state during the decrease and therefore the barrier layer thickness only varies in relation to the final average thickness.

The electrodeposition after the voltage decrease must be adapted to the final anodization voltage: The deposition potential must be chosen in respect to the resistance of the barrier layer, in order to realize an overpotential, the potential must be chosen sufficiently high. This requires a specific calibration for each final anodization voltage. For each specific final anodization voltage, a homogenous electrodeposition can be obtained in a range of deposition potentials. In this range, the deposition voltage influences the deposition rate.

In order to show the importance of this calibration and the importance of the slow anodization voltage decrease following the optimized decrease function exp3, an SEM image of an electrodeposition under non-optimized deposition conditions is

shown in Fig. II.2 . For the voltage decrease, the non-optimized function exp1 has been applied. The electrodeposition has been done after a voltage decrease down to 5 V and an electrodeposition at -5.0 V.

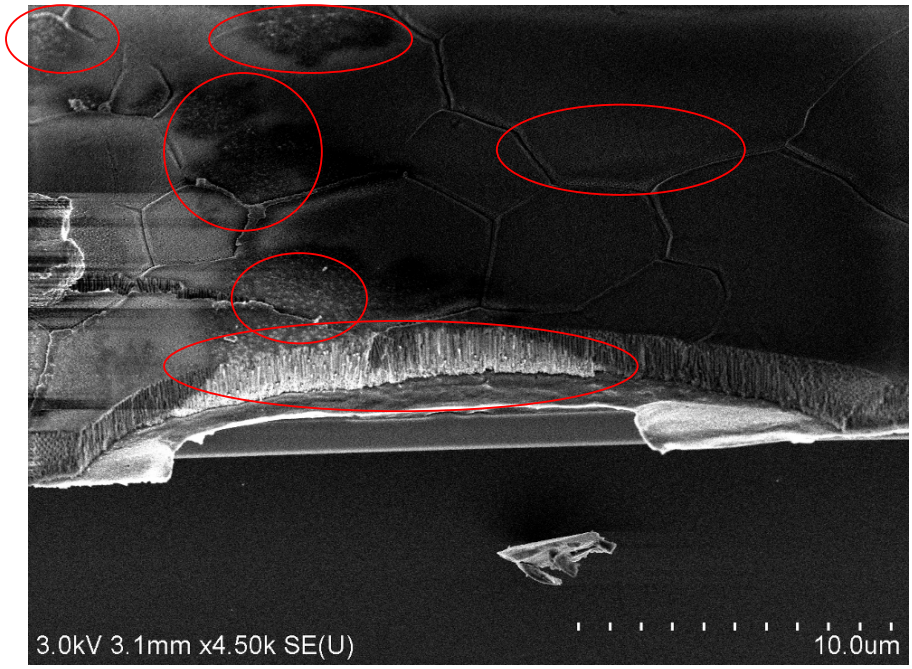


*Fig. II.2: SEM image of a sample after electrodeposition without optimized conditions.*

In the SEM image Fig. II.2, those areas in which Ni has been deposited are marked by red circles. It can clearly be seen that the deposition is not uniform, showing some pores filled up to the surface and leaving some pores without any Ni deposited. Those pores, in which Ni is deposited, are filled completely even producing “Ni-mushrooms” at the surface of the sample while in most of the pores, there is no Ni deposited. The bright dots on the surface as well as the bright lines at the facet of the PAA correspond to deposited Ni.

In order to avoid this effect, the anodization voltage has always been decreased following the optimized anodization voltage exp3 and the electrodeposition potential has been varied in a wide range for different final anodization voltages. Following the optimized voltage decrease and applying the respective calibrated deposition potential, we have been able to obtain a uniform deposition for different barrier layer thicknesses. In Fig. II.3, some results of homogenous electrodeposition for different types of samples are shown.

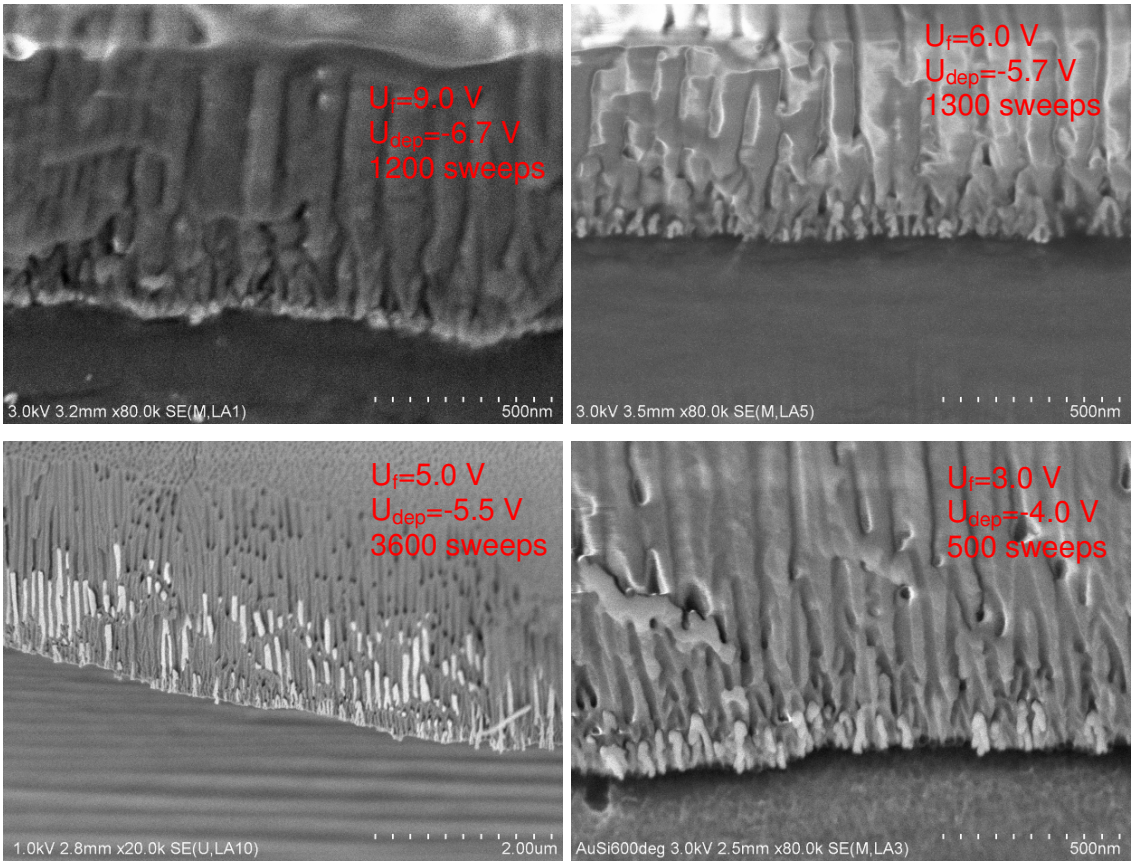


*Fig. II.3: Electrodeposition in PAA structures fabricated with different final anodization voltages $U_f$ and with different electrodeposition potentials $U_{dep.}$with different numbers of sweeps.*

On the one hand, in Fig. II.3 the deposition uniformity on all different barrier layer thicknesses can be observed. On the other hand, it is clearly seen that the deposition rate for the deposition on different barrier layer thicknesses is not comparable. Thus, if a precise control of the deposition rate is required, for each specific barrier layer thickness, the deposition rate must be calibrated for a defined deposition voltage. Then, the size of the deposited metal can be adjusted by varying the number of sweeps of the electrodeposition. In order to be able to control the electrodeposition precisely and thus to be able to deposit very small metal particles inside the pores, the deposition current must be reduced as far as possible, in other words, the overpotential must be decreased as far as possible in order to obtain a homogenous deposition at a low rate. A deeper investigation about this limit deposition potential is given in the section II.3.3.

The variation of the number of sweeps for the electrodeposition of samples that had been fabricated with $U_f$=5V and with $U_{dep.}$= -4.2 V is shown in Fig. II.4. During this electrodeposition, a deposition current of about 1mA/cm² has been measured.

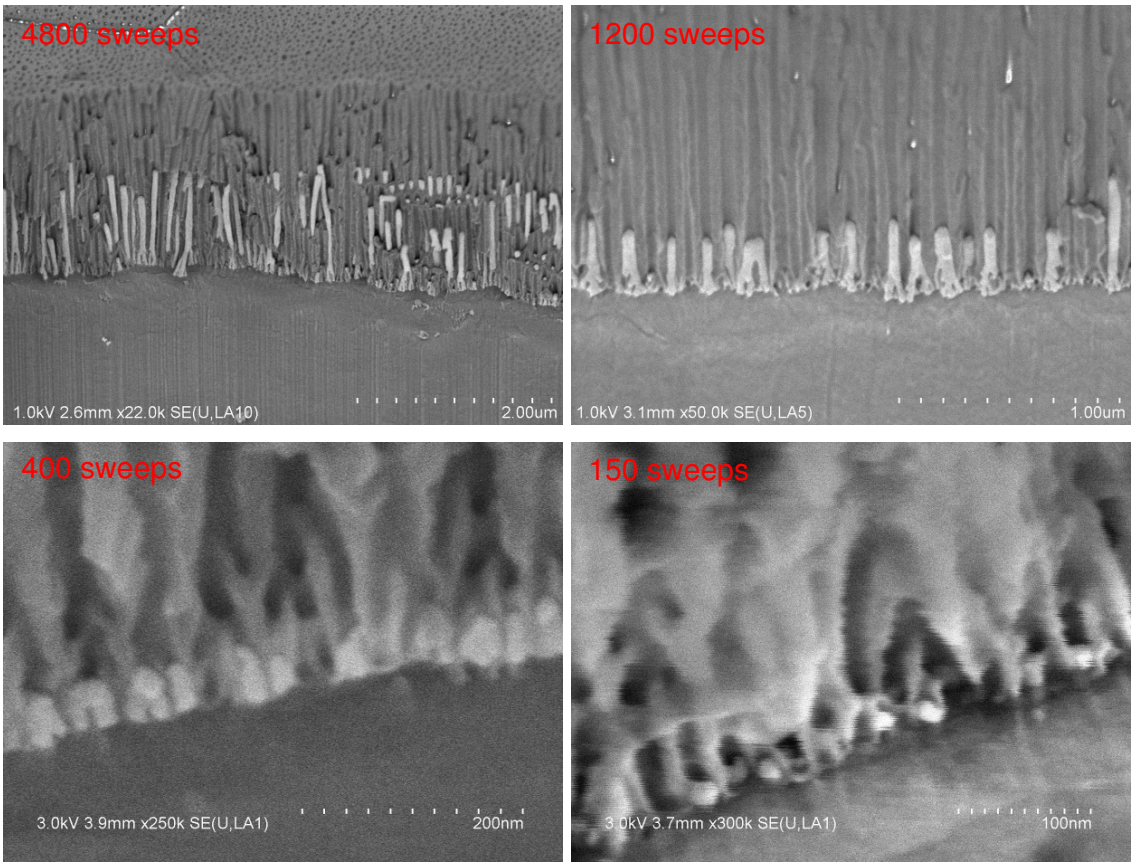


*Fig. II.4: Variation of the number of sweeps of the electrodeposition at -4.2 V at about 1.1mA/cm².*

While in Fig. II.3, the barrier layer thickness on which Ni is deposited is varied, in Fig. II.4, this barrier layer thickness is kept constant and only the number of sweeps is varied, each time fulfilling the electrodeposition under identical conditions. It is seen that the size of the deposited Ni-particles can be adjusted precisely by varying the number of sweeps.

With the described approach to very low deposition voltages and thus deposition currents, the control of the deposition rate could be optimized in a way that a deposition of Ni-particles of about 10 nm diameter could be realized. This has been proven to be a reliable technique for the preparation of high density dispersion of very small Ni catalysts. In this work, in chapter III, samples prepared under these conditions have been used for the growth of low diameter CNTs by CVD.

### II.3.3 Controlled variation of the deposition density inside PAA

As it has been described above, a uniform electrodeposition can be obtained after a very slow anodization voltage decrease and by applying a sufficiently high overpotential. The idea of a controlled variation of the deposition density inside PAA is based on the following understanding:

As it has been discussed in the previous section, the electrodeposition voltage must be higher than a specific limit voltage, which itself depends on the final anodization voltage $U_f$. This is valid if the anodization voltage is decreased very slowly, maintaining the anodization equilibrium during the entire decrease, which leads to a very uniform barrier layer distribution. Thus, if the decrease of the anodization voltage is done faster, i.e. in a non equilibrium, the distribution of the barrier layer will be less uniform leading to a less uniform electrodeposition: Only in those pores with a thin barrier layer, the electrodeposition will take place while in all other pores, the resistance of the parallel connected barrier layer inhibits the deposition current to pass through this pore. At this point, it has to be mentioned that, following the argumentation in chapter I.3.5.2, the number of pores with a thin barrier layer that corresponds to the final anodization voltage, decreases if the voltage decrease is done faster, since the anodization process is stopped in all the other pores before the final anodization voltage is reached. Thus, with increasing voltage decrease rate, the density of the filled pores is reduced.

Of course, for this approach, it is important that the electrodeposition potential must be very close to the limit potential which would be necessary for the uniform electrodeposition in case of a uniform barrier layer thickness. Thus, we first investigated the influence of the electrodeposition potential on the electrodeposition current, the later indicating the number of ions deposited per time (Fig. II.6). This investigation has been done on a sample for which the anodization voltage has been decreased following the optimized function exp3 developed in I.3.5.2 with $\eta=2.0*10^{-3}s^{-1}$.

For this purpose, $U_{dep.}$ was varied from -2.5 V to -6.5 V by applying voltage pulses of 5 ms followed by a delay time of 90 ms. A typical current response of the applied voltage pulse is shown in Fig. II.5.

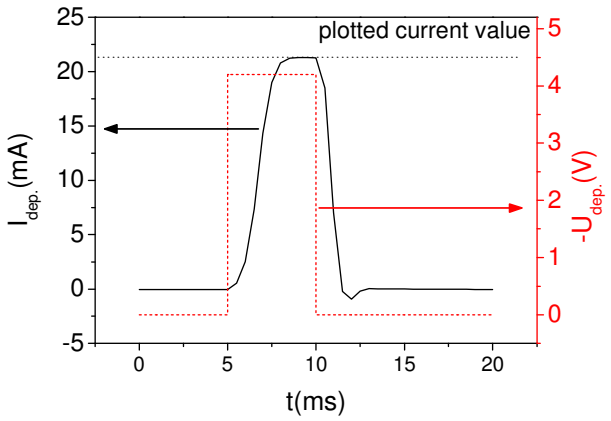


*Fig. II.5: Current response of the pulse of the electrodeposition potential.*

Taking into account only the maximum current values reached during the 5 ms voltage pulses, we could plot the current response curve for the applied electrodeposition voltage in the range from -2.5 V to -6.5 V. Such a current response curve is shown in Fig. II.6:

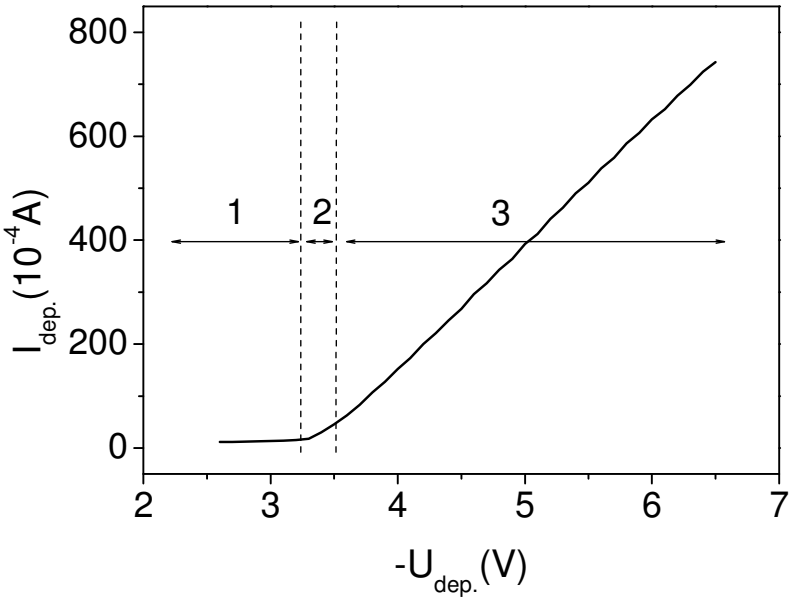


*Fig. II.6: Electrodeposition current in dependence on the electrodeposition potential.*

The graph in Fig. II.6 shows three regimes:

In the first regime, the voltage is not high enough to overcome the barrier layer and to reduce the Ni-ions at the same time. Only a very low leakage current is observed which slightly increases linearly (about 0.4 mA/V) with the applied voltage.

In the second regime, the applied voltage is just overcoming the threshold value which is determined by the barrier layer resistance, the reduction potential of Ni and the electrolyte resistance.

In the third regime, the linear current increase corresponds to the reduction and deposition of Ni at the pore bottom, which depends linearly on the applied voltage due to the combined resistance of the barrier layer and of the electrolyte.

Thus, the limit potential for the uniform electrodeposition is given by the interface between regime 2 and regime 3.

In order to compare the electrodeposition behaviour of samples prepared with different time constants η of the decrease function, we measured the same current-potential graph described above for a sample prepared with $\eta = 4.4 \times 10^{-3}\ s^{-1}$. The graph containing both current-potential-curves of the two mentioned samples is shown in Fig. II.7:

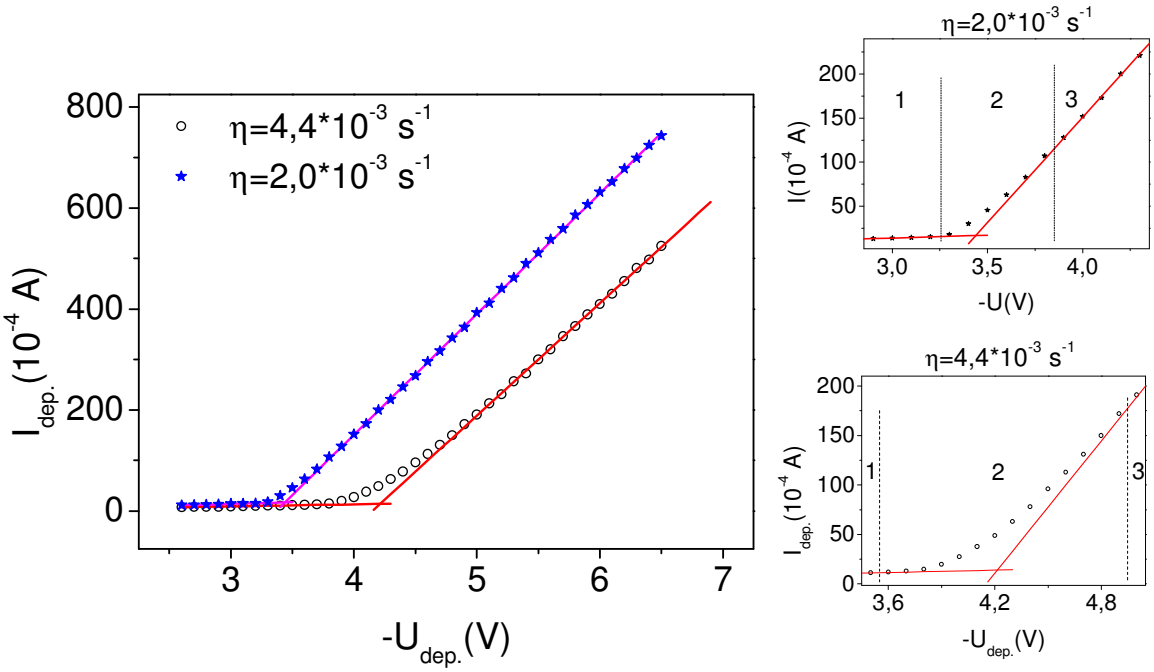


*Fig. II.7: Electrodeposition current versus the electrodeposition potential for different voltage-decrease functions of the previously realized anodization.*

The small η value yields a sharp transition between the two linear regimes, which takes place between ~ -3.3 V and -3.8 V. The high η value yields a much larger transition region, in the range of -3.6 V to -4.9 V. This clearly confirms the strong influence of the time constant of the exponential decrease on the distribution of the barrier layer thickness. Besides, in the case of the high η value, the transition regime (regime 2) is strongly extended to higher voltage values (in comparison to the low η case), which can be explained by the influence of the time constant on the barrier layer thickness distribution: as, during a fast voltage decrease, only those pores with a very thin initial barrier layer thickness can follow the anodization process until the end, the main part of the pores exhibit a barrier layer which is thicker than the expected value of 6 nm. This leads to an extension of the transition region in the $I_{dep.}= f(U_{dep.})$ curve towards higher electrodeposition voltages due to higher threshold voltages inside the major part of the pores.

The previously given explanation implies that the average barrier layer thickness and thus the average electrical resistance during the electrodeposition process is higher for samples with a faster exponential voltage decrease. This can be seen in Fig. II.7 in the third regime of the $I_{dep.}= f(U_{dep.})$ graph, where the slope of the linear increase during the electrodeposition is 22.1 mA/V for $\eta = 4.4 \times 10^{-3}\ s^{-1}$ and 23.8 mA/V for $\eta = 2.0 \times 10^{-3}\ s^{-1}$, which corresponds to a resistance of 45.2 Ω and 42.0 Ω, respectively. Taking into account the geometry of our setup and a resistivity of the electrolyte (Watts Bath) of about 10 Ω cm, we calculated a series resistance of about 14 Ω inside the electrolyte. This resistance has to be subtracted from the measured values in order to obtain the effective resistance of the barrier layer which we thereby determined to be 31.2 Ω ($\eta = 4.4 \times 10^{-3}\ s^{-1}$) and 28.0 Ω ($\eta = 2.0 \times 10^{-3}\ s^{-1}$). This means a shift of the average resistance of the barrier layer between the two different samples of 11 %.

In order to evidence the influence of the time constant η on the deposition density inside the PAA, we have carried out an electrodeposition inside PAA prepared at 40 V and followed by an anodization voltage decrease function with different time constants. The electrodeposition potential has been fixed at -4.2 V: This potential is already in the third regime for $\eta = 2.0 \times 10^{-3}\ s^{-1}$, but only in the second regime for $\eta = 4.4 \times 10^{-3}\ s^{-1}$. The results of such electrodeposition are shown in Fig. II.8. In order to better visualize the difference of the deposition density, the PAA

membrane has been etched after the electrodeposition, thus allowing the direct observation of the surface of the sample with exposed deposited Ni-particles.

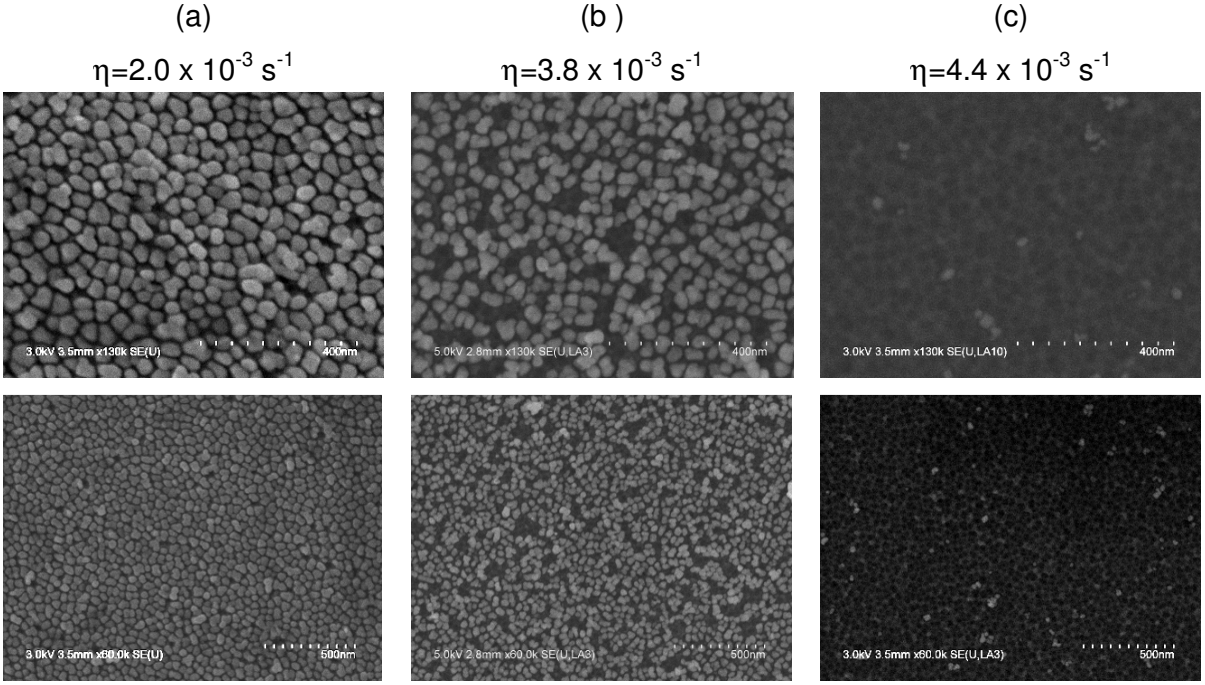


*Fig. II.8: Influence of the time constant η on the distribution of the deposited Ni-particles inside the pores (electrodeposition voltage = - 4.2 V). The SEM images show top views of the samples after selective etching of the alumina membrane.*

In Fig. II.8, it is obvious that the density of the filled pores decreases with increasing η. This shows that the distribution of the barrier layer thickness is more uniform if the voltage decrease is done slower. If the voltage is decreased faster, at low deposition voltages only in those pores with a thin barrier layer Ni is deposited. Thus, as shown, the deposition density can be varied by nearly two orders of magnitude by simply varying the rate of the voltage decrease at the end of the anodization.

If the electrodeposition is carried out during several thousands of sweeps, Ni-nanowires with different densities can be obtained.

In Fig. II.9, the SEM images of Ni nanowires on samples prepared with $\eta=2.0 \times 10^{-3}\ s^{-1}$ and $\eta=4.4 \times 10^{-3}\ s^{-1}$ are shown. Like for the samples in Fig. II.8, the PAA

membrane has been etched after the electrodeposition in order to visualize the Ni-nanowires.

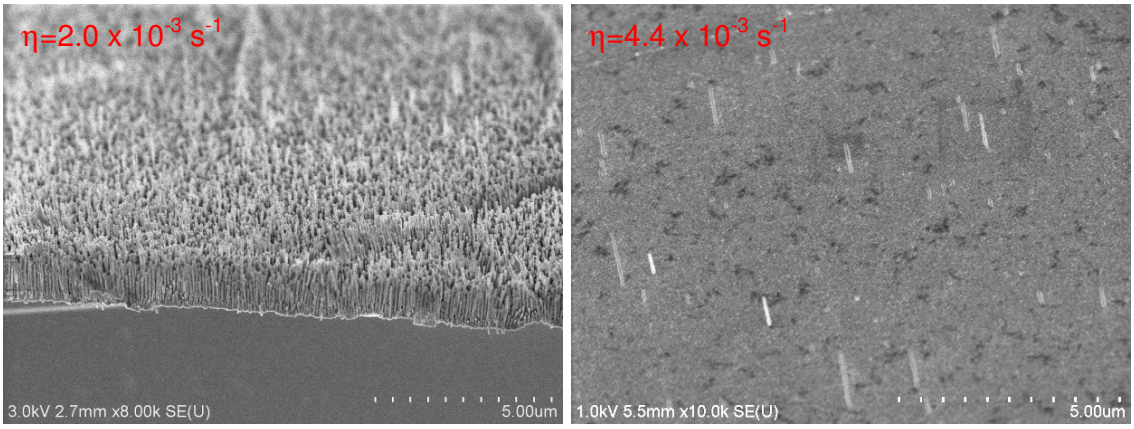


*Fig. II.9: SEM image of 45 °tilted samples with deposited Ni-nanowires.*

In Fig. II.9, the different densities of the deposited Ni-nanowires can clearly be observed. This shows the reliability of the discussed method for the variation of the deposition density, which could be the basis of further applications and investigations, like it also has been done in this work, see chapter III.

### II.3.4 Electrodeposition inside PAA with open pores on a conducting underlayer

In I.3.5.1, it has been shown that the barrier layer can be removed if PAA is realized on a conducting underlayer. Especially the PAA structures realized on TiN and Si showed clearly open pores on the specific layer. Thus, we also investigated the possibility of an electrodeposition on these samples: on the one hand, there is no insulating alumina barrier layer and on the other hand, the diffusion of catalyst during a later CVD growth or annealing in the Al through the barrier layer cannot take place. However, in case of the TiN, we have not been able to realize a homogenous electrodeposition. Probably, when the interface Al-TiN is reached, the surface of the TiN is oxidized immediately, leading to a highly resistive barrier layer at the pore bottom. As it has been shown in I.3.5.1, the breakdown of the anodization current is very slow, giving the opportunity to an “anodization” of the TiN. Thus, in this case, no electrodeposition could be realized in these PAA structures.

In case of the preparation of PAA on Si, it has been seen in chapter I.3.5.1 that the current breakdown is much faster than for TiN, leaving only a short time for the anodization of the Si at the end of the anodization process.

This, consequently, makes the electrodeposition in these PAA structures possible. In Fig. II.10, the electrodeposition results for two different electrodeposition potentials are shown. The topviews show very well the different deposition densities. In order to realize the topview, the PAA has been etched after the electrodeposition.

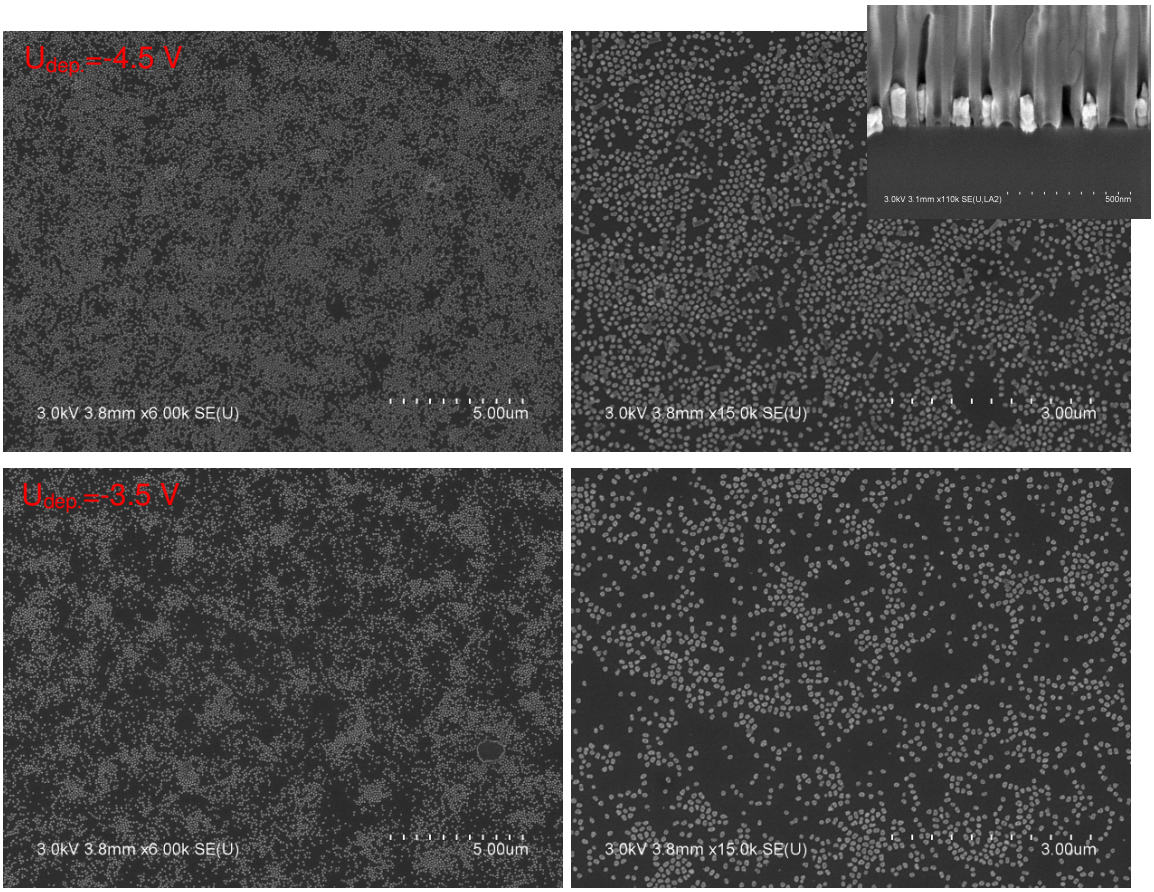


*Fig. II.10: Electrodeposition in PAA on Si. The inset shows a 45° tilted side-view of the sample before the etching of the PAA.*

In Fig. II.10, it is shown that the deposition density depends on the applied electrodeposition potential: The deposition density is higher at higher deposition potentials.

Like for the electrodeposition on the alumina barrier layer, again in this case a "barrier layer" is present, this time consisting of $SiO_2$, which has been formed when the interface Si-Al has been reached at the end of the anodization. This needs consequently a high deposition potential, since again this barrier has to be overcome

in order to realize the deposition of Ni. The influence of the deposition potential on the deposition density is obvious, referring to the same inhomogeneous distribution of the thickness of this barrier layer which has been demonstrated for the alumina barrier layer. Thus, a high overpotential is necessary in order to overcome this barrier through all pores and to depopulate during the pulse the electrolyte in those pores with a thinner barrier layer at the pore bottom. This assures an additional resistance in those pores which exhibit a thin barrier layer and thus leads to a homogenous deposition in the majority of the pores. The results of this electrodeposition strengthen the argumentation of the last chapters, since again the correlation between the barrier layer thickness and the deposition potential is demonstrated, whereas, this time, the electrodeposition is realized on a completely different material ($SiO_2$ instead of alumina).

## II.4 Conclusion

We have been able to develop an electrodeposition technique, which allows the precise control of the electrodeposition inside PAA in various manners:

First, a uniform electrodeposition with a precise control of the quantity of the deposited metal can be achieved. This uniform, controllable deposition can be realized on different barrier layer thicknesses. Thus, the resistance and the diffusion barrier between the Al-underlayer and the metal particles that are deposited inside the pores can be varied. This is an interesting feature for the device realization via PAA, for the contact between the Al electrode and the interior of the pores can be adjusted. Besides, in case of a later annealing or CVD growth, the diffusion barrier which inhibits the diffusion of deposited metal inside Al can be adapted to the experimental requirements.

Further, we have been able to develop a deposition technique through which the density of the pores of the PAA in which metal is deposited can be varied at whish. This offers very interesting applications, like the replacement of expansive lithography steps.

Finally, we have been able to demonstrate the electrodeposition on n-doped Si which is situated under the PAA. This can namely be interesting for the subsequent growth of Si-nanowires which will be in very good contact with the substrate, but also for other applications, like the patterning of Si-surfaces.

Thus, in a logic consequence of the results of chapter I, we have been able to pave the way for a huge variety of applications of PAA based on the electrodeposition technique.

# CHAPTER III

# GROWTH OF CARBON NANO TUBES (CNTS) USING PAA BASED TEMPLATES

# III. Growth of CarbonNanoTubes (CNTs) using PAA based templates

## III.1 Introduction

Since Ijima reported for the first time the observation of MultiWall-Carbon-NanoTubes (MWCNT) in 1991 [68], an incredible effort in research on CNTs has been made as CNTs were proven to have unique electrical and mechanical properties that make them interesting for a wide range of applications. A very important step during this development has been the discovery, again by Ijima, of the SingleWallCNTs (SWCNT) in 1993 [69]. SWCNTs are more fundamental than MWCNTs and show fascinating electronic and transport properties, for which reason they have been the subject of a large number of theoretical predictions and following experimental observations. Especially the prediction [70,71] and the experimental confirmation [72,73], that the electrical properties of SWCNTs depend on their geometrical characteristics and can be either semiconductor or metallic, opened a huge field of applications and thus induced enormous research activity. Nowadays there is a wide availability of CNT materials and high-yielded growth methods, and CNTs have been proven to be highly suited for the realization of nano-devices like for hydrogen storage, tips for scanning probe microscopy, field-emission devices and field effect transistors [74].

However, for all kind of devices based on CNTs, the organization and contacting of the CNTs remains a difficult challenge. The organization of CNTs thereby is basically needed for large-scale integration of CNTs and thus to open the way for practical applications of CNTs. Among a huge variety of organization methods for CNTs, the organization by PAA is a very promising one, as it offers the possibility to grow aligned CNTs inside the pores that are insulated from each other and that can be contacted in parallel. Besides, if PAA can be established for localized growth of CNTs, by simply varying the anodization conditions, CNTs can be grown in a wide range of densities and distances between each other.

In this chapter, we will present our work on the organization possibilities of CNTs by PAA. Based on our know-how about the CNTs growth on planar substrates

[75,76], the goal in this work was to adapt the growth conditions for CNTs for a growth directly inside PAA membranes or on substrates patterned by PAA. The point of departure of this study is given by the control of the PAA preparation and catalyst deposition which was described in the previous chapter and which allowed us to study the growth conditions of CNTs on PAA based substrates under reliable conditions.

# III.2 CNT: principles

## III.2.1 Physical properties

The structure of CNTs has been analyzed by TEM and STM techniques [77]. A SWCNT thus has been shown to consist of a single atomic graphic layer that is rolled to a seamless cylinder. A MWCNT consists of several coaxial cylinders, each being a SWCNT.

The graphite sheet represents the basic structure of a CNT. Inside a graphite sheet, the carbon is $sp^2$ hybridized and the carbon atoms form a hexagonal lattice. In the case of a graphite multilayer, the different layers are bonded by van-der-Waals forces. This is the case for MWCNTs, and therefore, MWCNTs show metallic properties along their axes, as graphite along the graphite planes.

The structure of a SWCNT can be explained by its 1D unit cell with the defining vectors $\boldsymbol{C_h}$, the chiral vector, and **T**, the translational vector (see Fig. III.1).

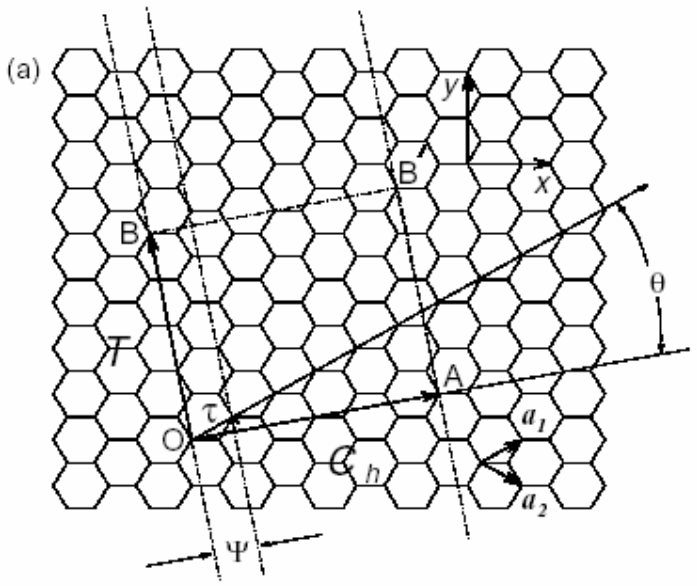


*Fig. III.1: Unit cell of a SWCNT. In the figure are shown the chiral vector* $\boldsymbol{C_h}$ *or* ***OA****, the chiral angle Θ, the translation vector* ***T*** *or* ***OB****, the unit vectors* $\boldsymbol{a_1}$ *and* $\boldsymbol{a_2}$ *and the translation unit τ and rotation angle ψ that determine the symmetry vector* ***R****=(ψ|τ).*

The circumference of a CNT is defined by the chiral vector which connects two crystallographic equivalent sites on a two dimensional graphite sheet and thus is a sum of the unit vectors of a graphite cell, $\boldsymbol{C_h} = n\,\boldsymbol{a_1} + m\,\boldsymbol{a_2}$. $\boldsymbol{C_h}$ is often described by only the two integers *(n,m)* that define the number of unit vectors constituting $\mathbf{C_h}$. The chiral angle *θ* is the angel between $\boldsymbol{C_h}$ and $\boldsymbol{a_1}$ and is given by $\theta = \tan^{-1}\left\{\frac{\sqrt{3}n}{2m+n}\right\}$

The diameter of a CNT can be described by: $d = \sqrt{3}a_{C-C}\sqrt{m^2+mn+n^2}\,\pi^{-1} = \frac{C_h}{\pi}$,

where $a_{C\text{-}C}$ is the bonding distance between the carbon atoms (1.42 Å) and $C_h$ is the length of $\boldsymbol{C_h}$.

Any SWCNT can thus be specified either by $\boldsymbol{C_h}$, i.e. *(m,n)*, or by the values of *d* and *θ*. The definition of $\boldsymbol{C_h}$ by *(n,m)* allows to distinguish between three distinct types of CNTs: armchair *(n,n)*, zigzag *(n,0)* and chiral *(n,m)*. The chiral angle *θ* can be defined for each type: for zigzag CNTs, *θ*=0°, for armchair CNTs *θ*=30° and for chiral CNTs 0< *θ*<30°. The three different types of CNTs are shown in Fig. III.2.

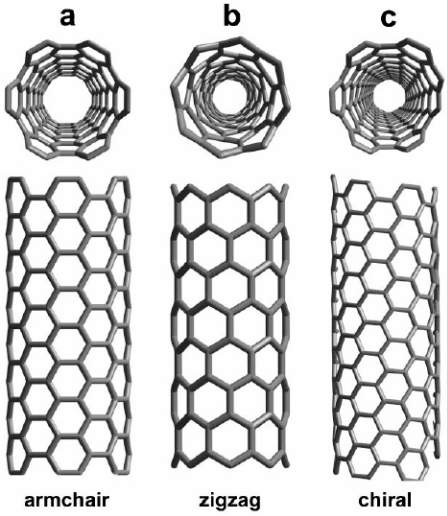


*Fig. III.2: Illustration of the three different types of CNTs: armchair, zigzag and chiral.*

The most fascinating property of SWCNTs is the fact, that SWCNTs can be either metallic or semiconducting depending on their chirality, i.e. the parameters *(n,m)*. Theoretical studies [78,79,80] have shown that all armchair SWCNTs are metallic, zigzag SWCNTs with *n* is a multiple of three and chiral SWCNTs with *n-m* is a multiple of three are very small gap semiconductors and all other SWCNTs are large gap semiconductors. It should be mentioned hereby that, in principle, the electronic structure of very small gap semiconducting SWCNTs is metallic, but the curvature due to the small diameters of the SWCNTs induces the small gap. The gap of the semiconducting SWCNTs is proportional to 1/R and $1/R^2$ for large gap and very small gap SWCNTs, respectively.

Typical diameters of SWCNTs are around 1.7 nm wheras the one of MWCNTs are in the range of 3 nm to more than hundred nm.

## III.2.2 CNT synthesis

Basically, there are three different methods to obtain high quality CNTs: the arc-discharge, the laser ablation and the Chemical Vapour Deposition (CVD) method. These three methods will briefly be introduced. Then, the CVD growth will be discussed more in detail as this growth technique has been adapted for the growth of CNTs in this work. Fig. III.3 shows the schematics of the three different growth techniques.

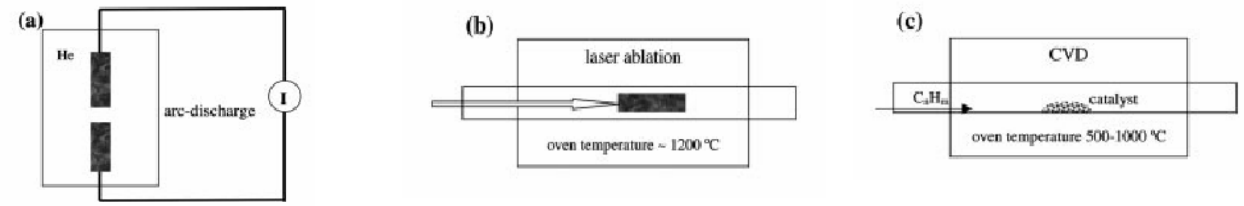


*Fig. III.3: Schematics of the basic CNT growth techniques: a) arc-discharge, b) laser ablation, c) CVD.*

### III.2.2.1 The basic CNT growth techniques

The first CNT observation has been realized by Ijima on CNTs fabricated by arc-discharge [1]. In this method, carbon atoms are evaporated from graphite electrodes by helium plasma that is established between two graphite electrodes (Fig. III.3a). A flow of inert gases through the chamber serves to collect the CNTs generated by the condensation of the evaporated carbon. The growth conditions like the plasma current, the chamber pressure and the flow of the inert gas are the most important in this setup. The arc-discharge has been shown to produce highly crystalline and pure MWCNTs and SWCNTs [2,81], whereas for the fabrication of SWCNTs, the graphite electrodes have to contain some amount of catalyst (e.g. cobalt). However, this method needs very high temperatures close to the melting point of graphite, typically 3000-4000 °C and a not negligible amount of by-products like graphitic particles and fullerenes is generated, from which the CNTs have to be separated.

The laser ablation, like the arc-discharge, also acquires a very high temperature (>1000°C) and leads to high quality SWCNTs [82,83]. In this method, intense laser pulses are used to ablate carbon targets with a low percentage of catalyst (e.g. cobalt or nickel), and the CNTs are generated by condensation and collected by the flow of inert gases. Like in the case of the arc-discharge, highly crystalline CNTs are obtained, but by laser-ablation, only SWCNTs are obtained. Again, by-products like fullerenes and graphitic particles are produced, but nevertheless, laser ablation is like arc-discharge the method of choice for the fabrication of high quality SWCNTs.

The CVD method is quite different to the two methods described above but again leads to the growth of SWCNTs and MWCNTs [84,85]. In this method, catalyst particles are heated up to their liquid state inside a furnace through which hydrocarbon gases are flowing. The catalysts are usually transition-metals which are catalytic in terms of the dissociation of hydrocarbon molecules at the catalyst surface.

During growth of CNTs, diffusion and saturation of the liquid catalyst particles of carbon atoms take place. The precipitation of carbon atoms at the catalyst surface leads to seamless tubular graphitic sheets in $sp^2$ hybridization as this is the energetically favoured state of the solid carbon formed on the catalyst (open edges mean a higher energy). The basic growth model for the CNT growth by CVD is the VLS model (Vapour Liquid Solid) [86,87], which describes the adsorption, diffusion and saturation process of the catalyst and the following crystallization of carbon to graphitic sheets including the growth of CNTs. The main parameters for the CVD method are the chamber pressure, the temperature, the catalyst and the used gases. Here, it has to be mentioned that the catalyst size strongly determines the diameter of grown CNTs. Typically, the growth temperature is around 500-1000 °C and metals like nickel, iron and cobalt are used as catalyst.

Although it is difficult to achieve by CVD growth CNTs with a quality comparable to those fabricated by laser ablation or arc-discharge, the CVD method has some important advantages:

- The growth temperature is much lower, which makes the process suited for direct growth on patterned substrates, like in PAA membranes, and thus offers the integration of the CNT fabrication in industrial processes.
- Besides, the catalyst can be arranged before growth which leads to an organized growth of CNTs.
- Moreover, the amount of by-products is much lower than for the laser ablation or arc-discharge method by what an additional separation process of the CNTs can be avoided.

The CVD method therefore is especially adapted to scale up the CNT fabrication for industrial applications.

#### III.2.2.2 The CVD and PECVD growth method

A very crucial parameter for the CVD growth is the catalyst [19,88,89]. On the one hand, as already mentioned, the diameter of the catalysts determine the diameter of the grown CNTs. On the other hand, the commonly used transition metals only exhibit catalytic properties if there are no impurities inside the metals. Especially a metal oxide shell around the catalyst particles inhibits the catalytic property. As, in general, these metals oxidize fast under ambient conditions, the

catalysts must be reduced before the growth inside the growth chamber. This can be done by a ramping or heating the catalyst first under reducing atmosphere like $H_2$ before starting the growth.

The CVD growth itself can be divided in two different growth modes: the bottom growth mode and the tip growth mode. The difference between these two modes is the localization of the catalyst: For tip growth, the catalyst is at the top of the CNT and the CNT grows under the catalyst, i.e. the catalyst is lifted up during growth. For bottom growth, the CNT grows on the catalyst and thus the catalyst is at the bottom of the CNT. The growth mode during the CVD growth mainly depends on the interaction between the catalyst and the supporting substrate.

One enhanced CVD growth technique is the PECVD (Plasma Enhanced CVD) growth mode, which has been reported for the first time in 1998 [90]. Both in the CVD and in the PECVD mode, the catalysts are heated, whereby in the case of CVD growth, generally a higher temperature of the substrate is needed as only due to the thermal energy and the catalytic properties of the catalysts the hydrocarbon molecules are dissociated and carbon thus can saturate the catalyst. In the PECVD mode, the hydrocarbon molecules are dissociated in the plasma by what the growth can take place at lower growth temperatures, which is important for a lot of samples. In addition, the plasma also leads to a directional flow of the created charged species, the positive ions are accelerated versus the sample. This also leads to an etching effect of the CNTs (plasma properties and the principles of plasma etching will be discussed in chapter IV), especially in the presence of gases like $H_2O$ and $NH_3$ which, in plasma, form carbon etching radicals (OH, O, $NH_2$, NH, H). Thus, all carbon exposed to the vertical flow of ions is etched, wherefore in PECVD, all CNTs are grown in tip growth mode with the catalyst protecting the CNT from etching. This leads to the growth of vertical, aligned CNTs. In the PECVD mode, the adjustment of the chamber pressure, the gas ratios and the current and acceleration of the ions versus the sample is especially delicate, as an equilibrium between the etching effect, the dissociation of the molecules and the prevention of damaging effects in the CNT walls has to be found.

### III.2.3 CNT organization

There is a huge variety of approaches for the organization of CNTs. In general, one can distinguish between the organization before, during or after growth. The organization methods before or during growth are strongly linked and imply the preparation of the substrate and depend on the growth conditions. The organization after growth usually is done by dissolving anyhow grown CNTs in a solution and a subsequent dispersion of CNTs on a substrate. Although after growth organization by dispersion of CNTs is a very efficient method and has been adapted for the fabrication of different devices like random network transistors, sensors and printed circuits [91,92], it is difficult to achieve aligned CNTs and to arrange them by large-scale compatible lithography processes in a manner that these CNTs can be contacted individually. In this context, growth organization has crucial advantages. In the following, two examples are given.

Patterned samples, on which catalysts have been arranged on the surface, have already been used in 1997 to grow organized CNTs [93]. The patterned catalyst structure has successfully been used for the fabrication of CNT networks and CNT transistors, whereby even individual CNTs could be contacted.

One very fascinating approach is the lattice oriented growth on Si or sapphire substrates [94,95]. In this method, catalyst is patterned on the surface and during the growth process, the CNTs grow along planes of the crystal lattice of the substrate. Recently, by this method parallel SWCNT have been realized on a sapphire substrate and then been processed to a thin film transistor.

Among the different possibilities of growth organization of CNTs, the growth of CNTs based on PAA is of particular interest. The PAA structure offers the possibility to organize catalysts without applying complex lithography steps, as catalysts deposited inside the PAA are highly ordered and the density and size of the catalyst can be varied in a wide range. In addition, the pore diameter of PAA is close to the one of CNTs. Thus, PAA can be used to guide the CNTs and to fabricate parallel but each of them insulated CNTs. Moreover, the anodization and electrodeposition are very reliable and cost efficient processes that could easily be integrated in industrial processes. This, of course, has attracted the interest of many researches, and in the last years, several studies about the growth inside PAA structures and possible applications have started [96,97,98,99,100].

In this work, the goal was to control the growth of CNTs on PAA patterned samples in a reliable way and thus to open the possibility to use PAA based samples for CNT devices.

## III.3 Results and discussion

### III.3.1 The CNT growth reactor

All CNT growth has been realized in a PECVD chamber (Fig. III.4), either in PECVD or in CVD mode, i.e. either with the plasma turned on or off.

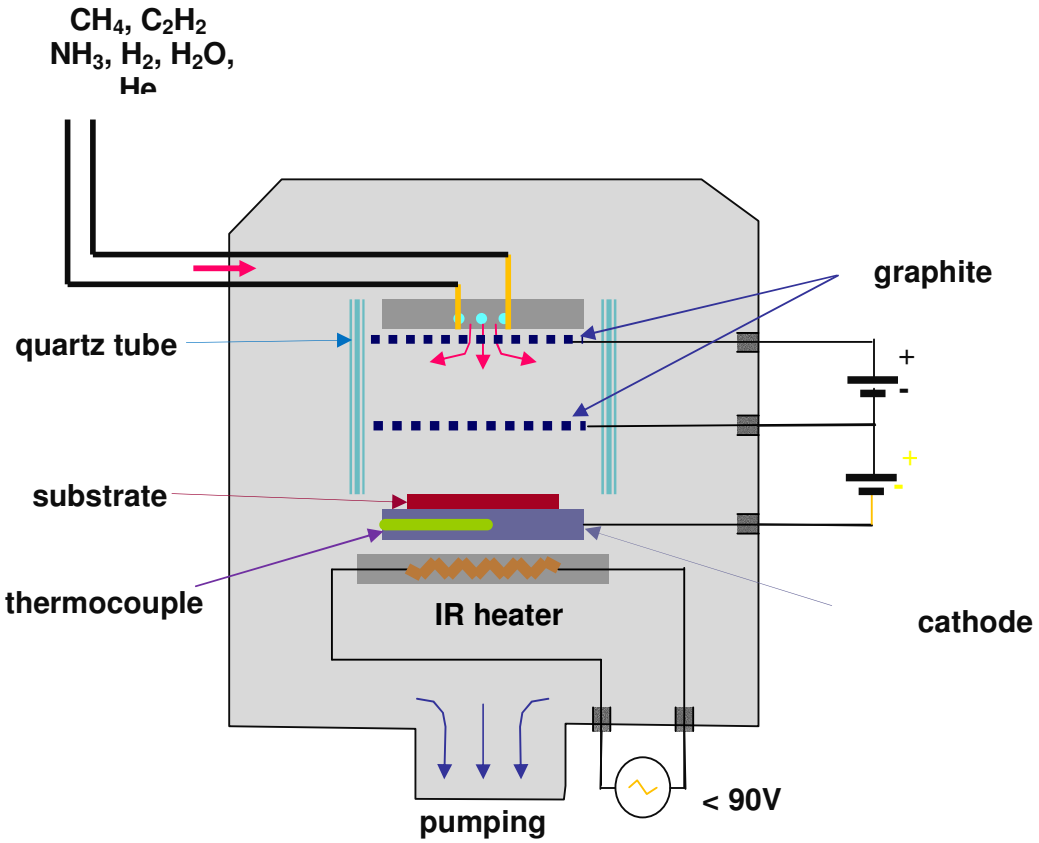


*Fig. III.4: Schematics of the PECVD reactor.*

The PECVD chamber contains two graphite grids and the sample electrode. The sample is mounted on the graphite plate by graphite glue, and the temperature of the graphite plate is controlled by a thermocouple. The temperature of the graphite plate and thus the sample is adjusted by a Eurotherm controller which controls the

power of the IR heater. The position of the sample in respect to the grids can be varied by an external screw. The distance between the grid and the sample mainly influences the drift current $I_D$ (see explanation at the end of this paragraph).

At the one side of the chamber there is the gas inlet, at the opposite side, there is the sample electrode with the heater.

The PECVD chamber can be used in triode or diode mode. In diode mode, there is only one DC power between the sample and one of the two grids, which means that the acceleration of the ions versus the sample correlates with the plasma density. In this mode, it is difficult to control precisely the growth and etching parameters of CNTs at the same time. In the triode mode, the plasma is generated by a DC power between the two grids and the ions are extracted by applying a low DC potential between the substrate and the lower grid. Thus, the direction of momentum of the ions and the plasma density can be controlled mainly independently, and in general, the CNTs therefore show smaller damage and defects. Another mode is the downstream mode, in which plasma is created between the two grids without applying a potential on the sample.

Very important parameters for the CNT growth in PECVD are, besides the parameters already mentioned as crucial, the ion current on the sample, also called extraction current $I_{ex}$, and the extraction voltage $U_{ex}$, that is applied between the sample and the second grid. $I_{ex}$ and $U_{ex}$ determine the amount of ions and the momentum of the ions, respectively, and thus influence the etching and growth behaviour during the CNT growth. In triode mode, as described above, $I_{ex}$ and $U_{ex}$ can be varied to a large extent independently as the plasma power between the two grids determines the plasma density. For a given plasma power, $I_{ex}$ increases with increasing $U_{ex}$. However, for a given $U_{ex}$, $I_{ex}$ increases with increasing plasma power. If there is no extraction voltage applied ($U_{ex}$=0), the current value of $I_{ex}$ depends only on the plasma power and the distance between the grid and the sample. The current at $U_{ex}$=0 is called “drift current” $I_D$.

## III.3.2 Growth of CNTs inside PAA by CVD growth technique

The CNT growth inside PAA implicates several problems. The aspect ratio of PAA membranes is quite high and thus it is not evident that the gas molecules can migrate

down to the pore bottom, saturate the catalysts and lead to a subsequent growth. Anyway, by choosing a low growth pressure of 2 mbar, this problem could be solved, since the higher free mean path in the low pressure gas assures the diffusion of the species through the pores down to the pore bottom. Besides, the pores should not be clogged by amorphous carbon, for which reason well established growth parameters with well adjusted gas ratios of etching and hydrocarbon gases are necessary. In this respect, in this work we could profit of the know-how in our group and established growth recipes could be adapted for the growth inside PAA as well.

The most striking problem we have been faced with for the growth of CNTs inside PAA has been the growth temperature and the temperature ramping which have an important influence on the catalyst and thus the growth of CNTs. The catalysts deposited at the pore bottom are separated only by the barrier layer from the Al layer, on which the PAA has been fabricated. If there is a diffusion of the catalyst or the aluminium through the barrier layer, the catalyst is either not anymore available for growth or it is "poisoned" by the Al. Thus, the temperature must be far below the melting point of aluminium, which is at 660 °C for ambient conditions. The analysis of the behaviour of the catalyst has been shown to be the most crucial element for the CNT growth inside PAA and thus the following studies are mainly focused on this problem.

### III.3.2.1Sample preparation

The growth conditions of CNTs inside PAA have been studied on PAA membranes with electrodeposited nickel inside. The sample preparation was based on the knowledge acquired during the numerous studies on PAA fabrication and electrodeposition described in chapter I and chapter II. This allowed us to start the CNT growth from samples with a homogenous catalyst deposition that could be reproduced at wish.

In order to study the behaviour of the catalyst on the barrier layer, the anodization of the PAA membranes was done in oxalic acid and at a fixed voltage of 40 V, as under these conditions, the reliability of the sample preparation was guaranteed. Different barrier layer thicknesses have been prepared and the diameter or length of deposited catalyst has been varied in a wide range. For all samples the

exponential voltage decrease function exp3 (see paragraph I.3.5.2) has been applied, the final barrier layer thickness has thus always been determined by the last voltage of the voltage decrease. The amount of catalyst deposited inside the pores has been adjusted by the number of sweeps of the electrodeposition.

### III.3.2.2 The CNT synthesis inside PAA by CVD

In a first step we have analyzed the influence of the final anodization voltage on the diffusion of the catalyst though the barrier layer. The cleaved facets of two samples before and after annealing are shown in Fig. III.5.

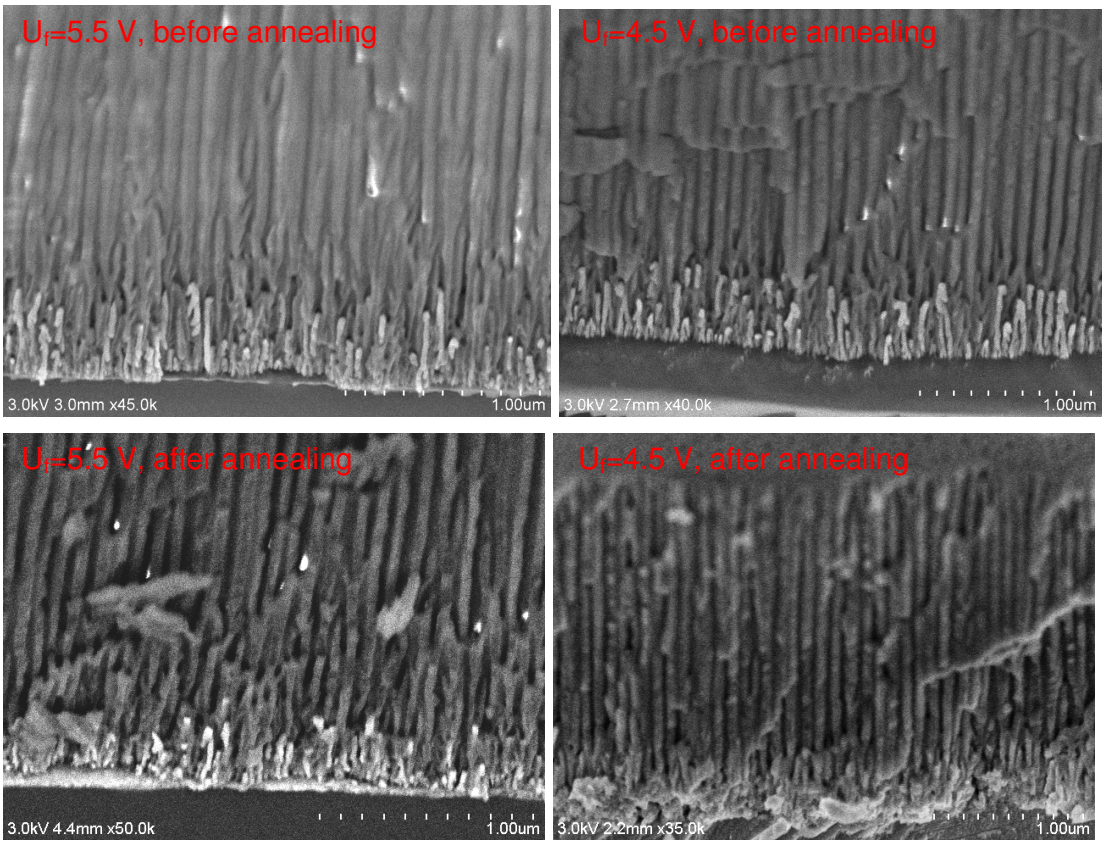


*Fig. III.5: Samples before and after annealing prepared with different final anodization voltages $U_f$. The annealing has been done at 640 °C during 20 min at 10 mbar under $N_2$.*

The influence of the barrier layer can clearly be seen: If the voltage decease is stopped at $U_f$=5.5 V, i.e. at a barrier layer of about 7.7 nm, the annealing does not

strongly change the shape of the Ni-wires inside the PAA since no diffusion of Ni through the barrier layer takes place. To the contrary, if the voltage decrease is stopped at $U_f$=4.5 V, i.e. at a barrier layer of about 6.3 nm, the Ni inside the PAA diffuses nearly completely through the barrier layer. Thus, at temperatures close to the melting point of Al, the barrier layer has been shown to have a major influence on the behaviour of the catalyst.

For the study of growth conditions of CNTs, we decided to focus on samples prepared with final voltages of 5.0 V and to fix the growth temperature to 625 °C. In the same PECVD chamber, it has been shown in our group that at 650 °C, with $C_2H_2$ as hydrocarbon growth gas and $H_2O$ as etching gas, CNTs of good quality with very low deposition of amorphous carbon can be achieved on plane substrates (see Fig. III.6 with the details of the deposition conditions) [101].

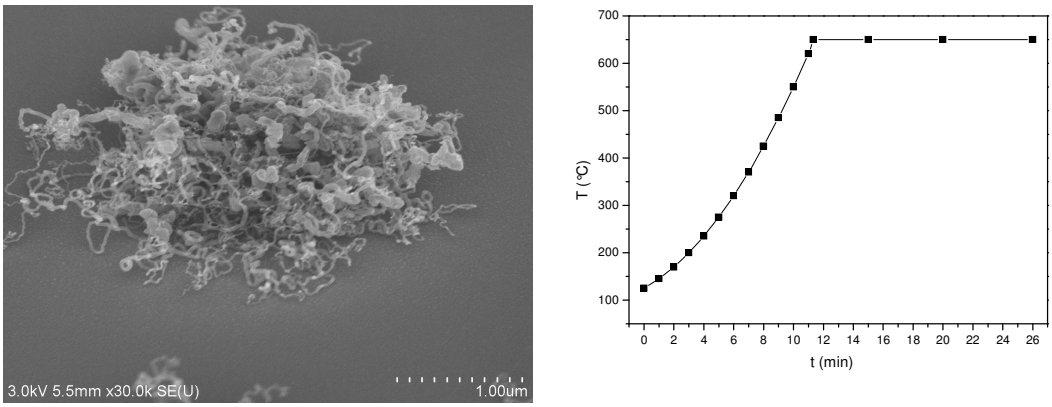


*Fig. III.6: CNT growth at 650 °C on a plane substrate with 7 nm thick Ni layer at 3 mbar and flow gases $H_2O$ 10 sccm, $C_2H_2$ 30 sccm during the growth of 15 min and $H_2O$ 10 sccm and $H_2$ 30 sccm during the ramping. The temperature during the entire process is shown in the graph.*

The addition of $H_2O$ during the growth offers several advantages for the growth of CNTs inside PAA. On the one hand, the presence of $H_2O$ allows the growth at low growth temperatures as $H_2O$ etches already at very low temperatures efficiently amorphous carbon. On the other hand, the oxidizing property of $H_2O$ strengthens the barrier layer under the catalyst and thus hinders the diffusion and poisoning of the catalyst. The use of $C_2H_2$ as hydrocarbon gas has been chosen due to the low decomposition temperature of $C_2H_2$, which is as well important to realize a low temperature growth.

For the growth inside PAA, in this work basically the growth conditions established in our group have been used. However, the $C_2H_2$, in the shown figure fixed at 30 sccm, has been reduced to 15 sccm in order to assure the etching effect of $H_2O$. Besides, a low pressure of 2 mbar has been fixed for the growth in order to have longer free mean paths of the species which is favourable to let the gases moving towards the catalyst at the pore bottom.

Under these conditions, different temperature ramps and reduction processes have been studied. For the series, PAA membranes with catalyst of about 10-20 nm diameter on a barrier layer of about 10 nm have been used (Fig. III.7).

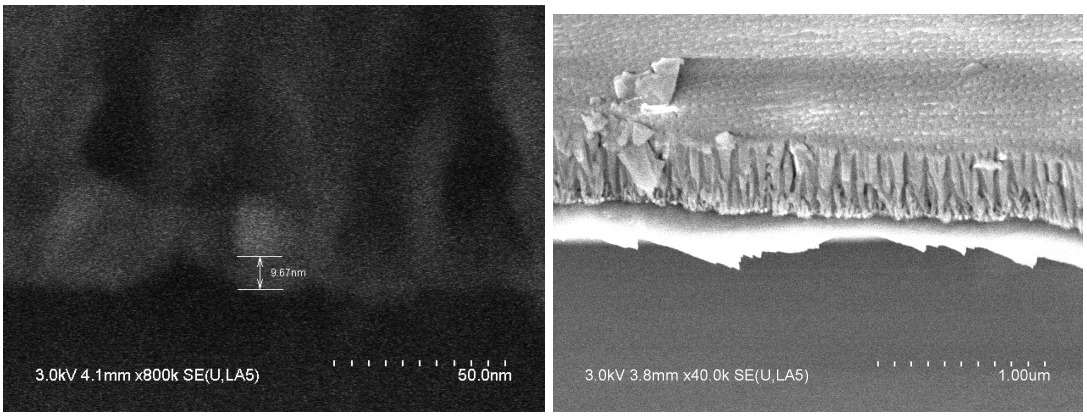


*Fig. III.7: SEM images of nickel catalyst before growth, deposited on the barrier layer.*

In Fig. III.7, a typical catalyst particle inside the PAA structure as well as the uniformity of the deposition is shown. The diameter size and the uniformity of the catalyst varied in a very low range between the samples. However, only a filling rate of about 50 % of the catalyst has been obtained due to the very sophisticated conditions for the deposition of the very small catalyst.

Of course, the catalyst has to be reduced before the beginning of the growth. However, the presence of reduction gases ($H_2$) also reduces the $Al_2O_3$ of the barrier layer and thus makes the catalyst diffuse into the Al layer. Thus, during the temperature ramp, we also added $H_2O$ which should oxidize the layer under the catalyst before the reduction process in order to assure a stable diffusion barrier under the catalyst. We found, that the correct management of the $H_20$ and $H_2$ gases during the ramping and the growth strongly determines the growth result. The influence of different ramping and growth parameters on the CNT growth is shown in Fig. III.8.

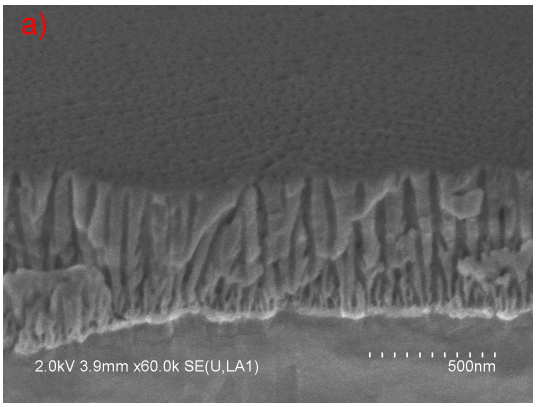
a)
2.0kV 3.9mm x60.0k SE(U,LA1)
500nm

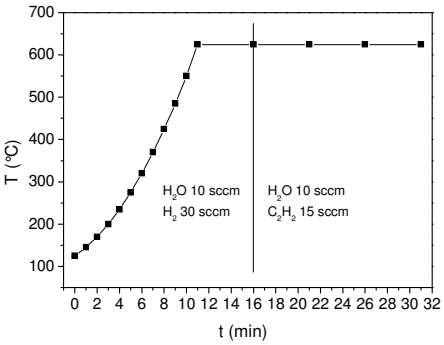
T (°C)
t (min)
H2O 10 sccm
H2 30 sccm
H2O 10 sccm
C2H2 15 sccm

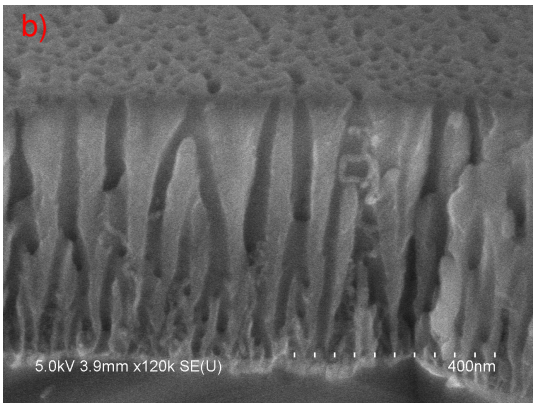
b)
5.0kV 3.9mm x120k SE(U)
400nm

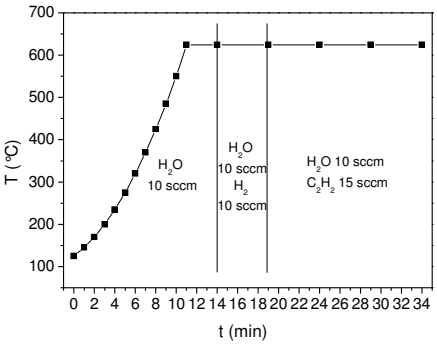
T (°C)
t (min)
H2O
10 sccm
H2O
10 sccm
H2
10 sccm
H2O 10 sccm
C2H2 15 sccm

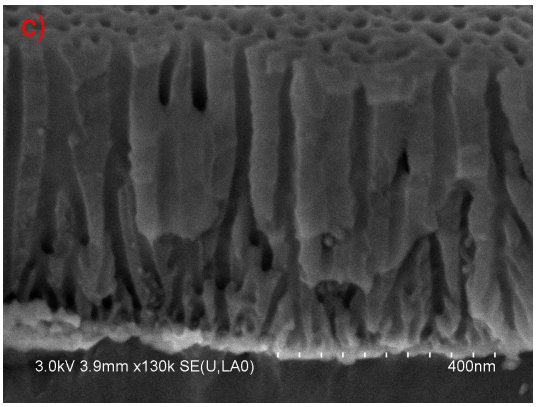
c)
3.0kV 3.9mm x130k SE(U,LA0)
400nm

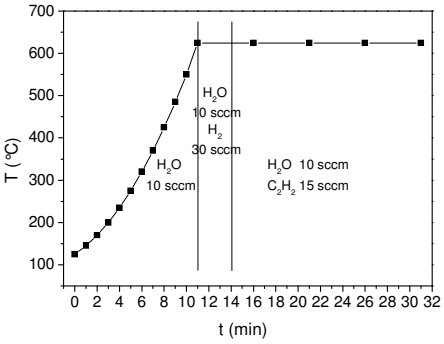
T (°C)
t (min)
H2O
10 sccm
H2O
10 sccm
H2
30 sccm
H2O 10 sccm
C2H2 15 sccm

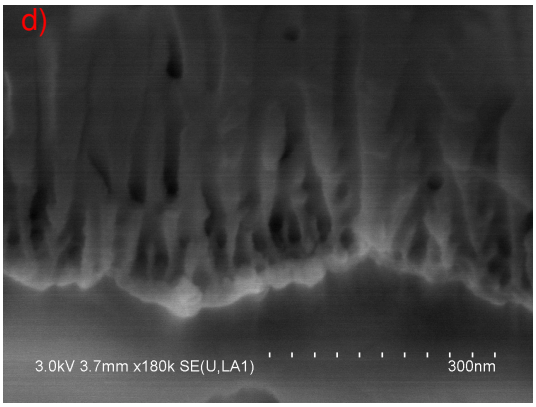
d)
3.0kV 3.7mm x180k SE(U,LA1)
300nm

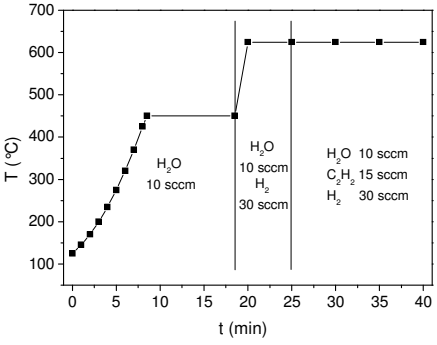
T (°C)
t (min)
H2O
10 sccm
H2O
10 sccm
H2
30 sccm
H2O 10 sccm
C2H2 15 sccm
H2 30 sccm

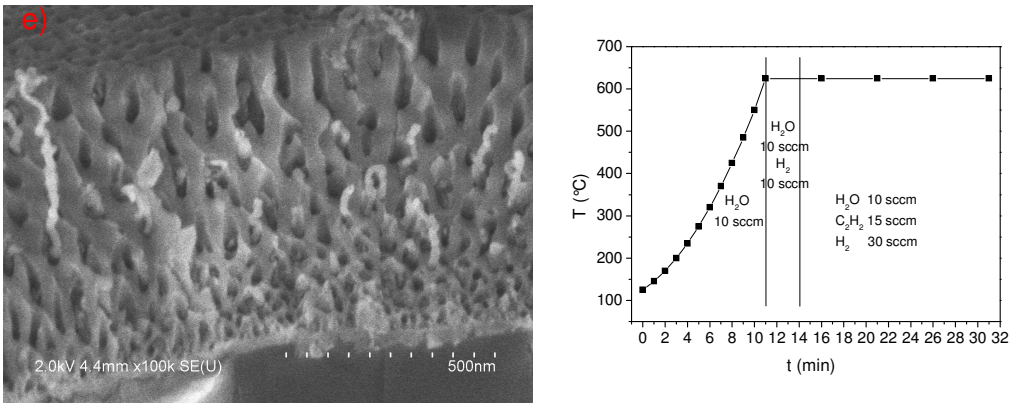


*Fig. III.8: Influence of the ramping and growth conditions on the CNT growth inside PAA.*

The influence of the ramping and growth conditions can be explained and summarized by the following:

- If, like in a), the ramping is done under $H_2O$ and $H_2$ flow, the reduction effect during the ramping is too strong, the barrier layer is reduced and the catalyst diffuses and consequently no growth can take place.
- If, like in b), the ramping is done under only $H_2O$ flow, the catalyst and the barrier layer are strongly oxidized and a subsequent reduction by adding a low $H_2$ flow of 10 sccm during 5 min mainly reduces the catalyst and not the barrier layer which leads to a good density of CNTs inside the PAA. However, in this case, the CNT density is much lower than the density of deposited catalyst before growth which is either due to still oxidized catalysts or due to the beginning of diffusion of catalyst during the 5 min of reduction before growth.
- We therefore shortened the oxidation step and increased the $H_2$ flow in c) during the 5 min of reduction, which should lead to a better reduction of the catalyst. It is evident, that the lack of CNTs in this case indicates the diffusion of catalyst through the barrier layer which clarifies the result in b): the lower CNT density in b) is obviously due to the starting diffusion of the catalyst.
- Thus, in a next step (d), a long oxidation step of 10 min under $H_2O$ flow was included in the ramp in order to strengthen the barrier layer before the reduction step. However, it seems that during the following reduction step of 7 min, the oxide is completely reduced and the catalyst again has diffused through the barrier layer.

- In e), the conditions that show the best results for the growth of CNTs inside PAA in our study are shown: After the oxidation step, a short reduction of 3 min by adding a low $H_2$ flow of 10 sccm has been applied before the growth, whereas the reducing gas $H_2$ has been maintained during the growth. This leads to a density of CNTs which is comparable to the catalyst density before the growth.

Another open question has been the dependence of the diameter of the CNTs on the size of the catalyst inside the pores. Especially the question was raised if the catalyst inside one pore can be the origin of several CNTs which grow in one pore.
After the observations done in this work, the catalyst diameter inside the pore determines strongly the diameter of the CNTs grown inside PAA. In all analyzed samples, there has been only one CNT per pore, and the diameter of the CNT inside the pore corresponds to the diameter of the deposited catalyst before growth (see Fig. III.9).

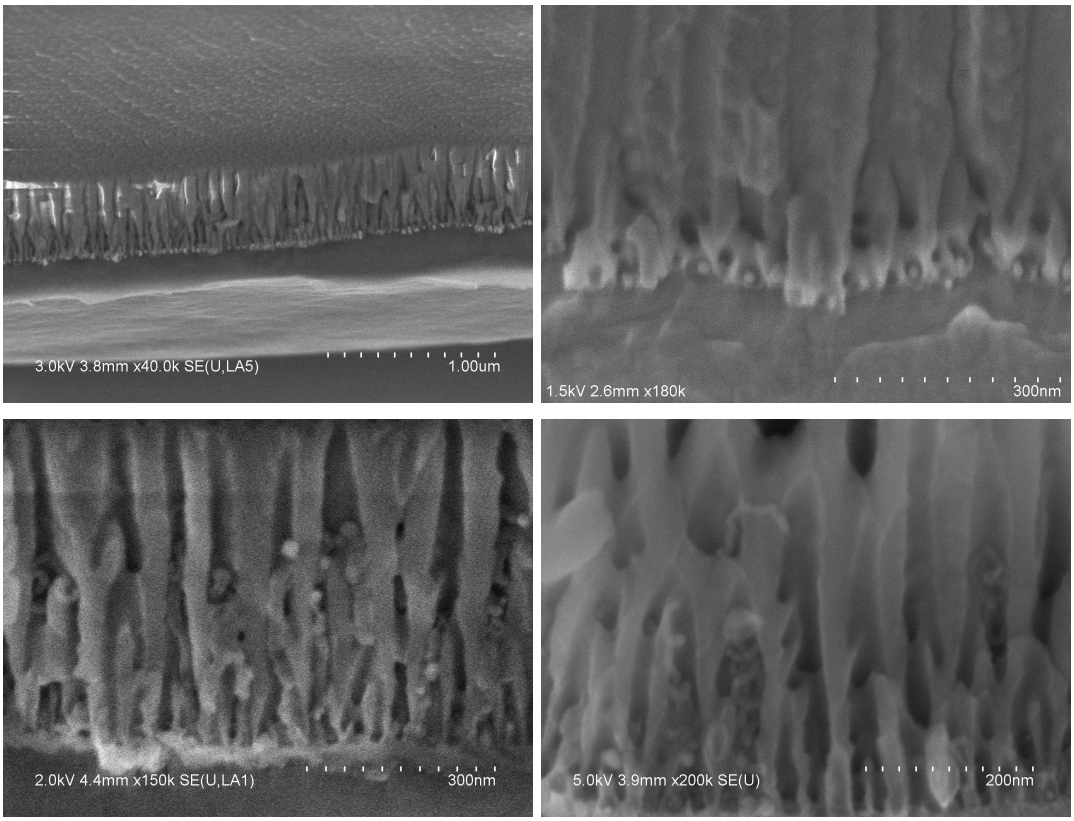


*Fig. III.9: Dependence of the CNT diameter on the catalyst size inside PAA before growth. The upper images show the samples before, the lower after growth, respectively.*

In Fig. III.9, from the upper images the diameter size and the uniformity of the catalyst deposition can be estimated. In the lower images, it can be seen that the CNT diameter depends on the catalyst diameter before the CNT growth and that in all cases, from each single catalyst in one pore, only one CNT has been grown.

## III.3.3 Growth of CNTs on PAA structured surfaces by PECVD

In this work, PAA structured surfaces have been used for the PECVD growth in order to vary the surface density of the vertical tubes fabricated by PECVD. This can be very interesting for field emission applications as for these applications the density of the electron emitting tubes influences strongly the performance of the field emission devices. The use of PAA patterned surfaces can replace costly lithography steps and therefore is of special interest.

### III.3.3.1 Sample preparation

The PECVD growth has been done in the triode mode, as this mode offers a multiple control of the growth conditions and leads to high quality vertically aligned CNTs. The sample used in the triode PECVD mode is polarized and thus must be conducting. The PECVD, in this case, is thus not adapted for the growth of CNTs inside PAA (as discussed in the previous chapter), but only for the growth of samples for which the PAA has been used for a patterning process and then been removed before the growth.

PAA has been used to localize the catalyst on the surface of a sample. For this goal, an Al layer has been deposited on a highly doped, degenerated n++ Si wafer, whereas a TiN layer between the wafer and the Al inhibited the diffusion of Al inside the Si-wafer during growth. Then, the PAA was fabricated by anodization and the catalyst was deposited inside the PAA. Finally, the PAA was removed by chemical etching. According to the method of the exponential decrease described in chapter I and II, we were able to vary the density of the deposited catalyst and thus to vary the density of CNTs by simple use of PAA. For all samples, the final voltage has been fixed at 5.0 V.

Like in the CVD growth described in the previous paragraph, during PECVD growth the catalyst is only protected by the barrier layer from diffusion into the Al on which the PAA has been formed. Thus, we have been faced to the same problem for the temperature ramp and reduction step as in the previous paragraph. The development of the ramping and reduction process for the PECVD growth therefore was based on the study discussed just before. However, the conditions for the CVD growth inside PAA and the PECVD growth after having etched the PAA are not completely the same. The barrier layer under the catalyst is as well slightly etched. Thus, the fine adjustment of the ramping and the reduction conditions had to be done again.

### III.3.3.2 The CNT synthesis by PECVD

The CNT synthesis by PECVD has been done under similar conditions as the CVD synthesis described in the previous paragraph. The growth has been realized with the same gases, $C_2H_2$ and $H_2O$, as the advantages of the low decomposition temperature of $C_2H_2$ and the etching and oxidizing feature of $H_2O$ are as well very important for the low-temperature growth of vertical aligned CNTs by PECVD.

In previous experiments, we have shown that well crystallized MWCNTs can be prepared with the $C_2H_2/H_20/H_2$ mixture at very low growth temperatures by triode PECVD mode. A typical result is shown in Fig. III.10.

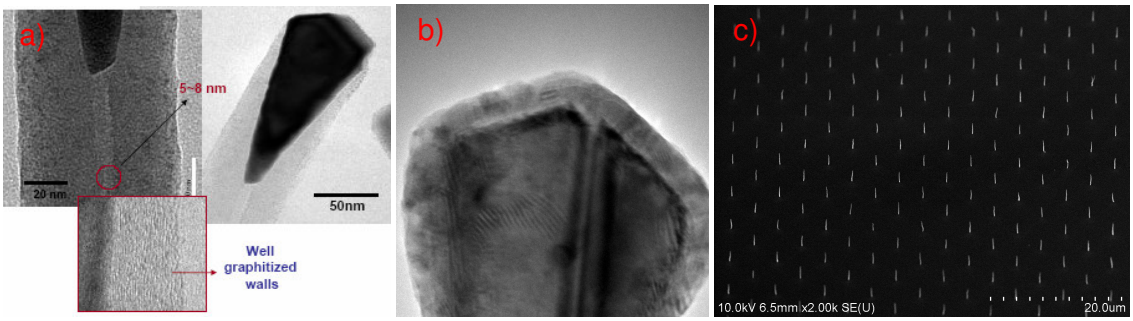


*Fig. III.10: TEM images of MWCNTs grown by PECVD at 600 °C under $C_2H_2$, $H_2O$ and $H_2$ atmosphere. The TEM images in a) show the very good crystallization of the MWCNTs. The TEM image in b) shows a close view of the nickel catalyst at the top of the MWCNT. The etched shape of the catalyst as well as the amorphous layer, which we identified as nickel oxide, is clearly seen. In c) an SEM image of vertical aligned CNTs obtained from nickel-pads (e-beam lithography) on TiN are shown.*

However, the growth of CNTs by PECVD at very low temperatures (T<650°C) needs a very sophisticated growth technique which allows the controlled saturation and formation of the catalyst and a precisely controlled equilibrium between the growth of CNTs and the vertical etching that leads to highly crystalline, vertical CNTs. In the following, the principles of the PECVD growth and the used method are introduced.

A very important stage of the CNT growth by PECVD is the very beginning of the growth.
This initial growth state can be described by the followig four steps [102]:
a) Adsorption and diffusion of carbon species into the catalyst;
b) Saturation of the catalyst and beginning precipitation of graphitic sheets;
c) Facet etching and deformation of the catalyst and beginning CNT growth;
d) CNT growth.

Especially the adsorption, saturation and deformation process concerning the catalyst must be precisely optimized, as during these processes, the present plasma should provide dissociated hydrocarbon molecules to saturate the catalyst by only slightly etching amorphous carbon and then increase the facet etching with the beginning precipitation of carbon and the starting formation of the CNT until finally a constant equilibrium between the CNT growth and the facet and amorphous carbon etching is obtained. Therefore, the plasma parameters have been adjusted in the following way:

- At the beginning of the growth process, i.e. at the beginning saturation process, the extraction voltage $U_{ex}$, the ion current $I_{ex}$ and the gas flow of $C_2H_2$ are fixed to low values, whereas the gas flow of $H_2O$ and $H_2$ are constant during the entire growth.
- During the growth, $I_{ex}$, $U_{ex}$ and the $C_2H_2$ flow are increased linearly, which increases the vertical etching effect of the plasma in the PECVD and the effective flow of hydrocarbon radicals to the sample at the same time.
- Thus, after the initial catalyst formation of the mentioned step c), the increasing etching of carbon effect leads to a vertical growth of the CNTs and the coincidental increase of hydrocarbon radicals enables the continuation of the CNT growth.

In Fig. III .11, the development of $I_{ex}$, $U_{ex}$ and the used gases are shown for the growth of the CNTs shown in Fig. 10, which, in the following, will be called the "standard conditions".

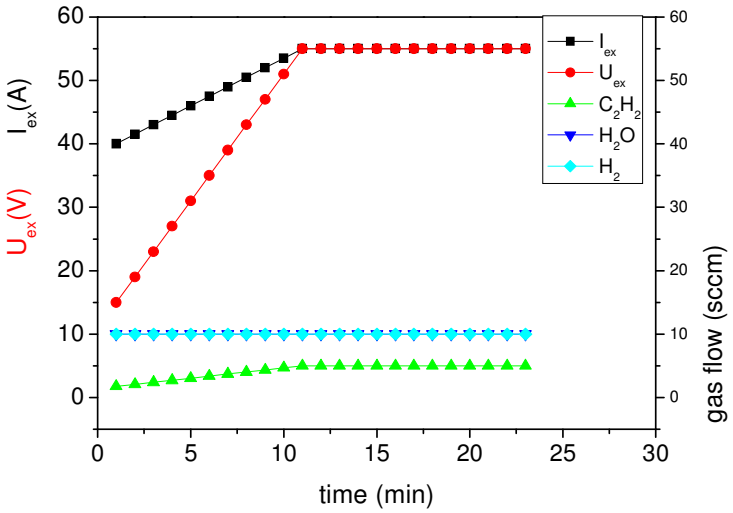


*Fig. III.11: Variation of the growth parameters during the growth. The growth pressure is fixed at 2 mbar, the distance between the second grid and the sample is 30 mm.*

We have established the growth parameters shown above for a specific reference sample with thin-layer nickel-plates. However, these parameters have to be adjusted for each specific sample type. The best conditions found for the samples realized in this work are shown in Fig. III.12. The difference between samples fabricated under the optimized conditions and under the standard conditions is shown in Fig. III.13. Hereby, the growth temperature has been reduced to 575 °C, since the plasma leads to a further heating of the sample and for 600 °C, due to the diffusion of the catalyst, no growth of CNT has been achieved.

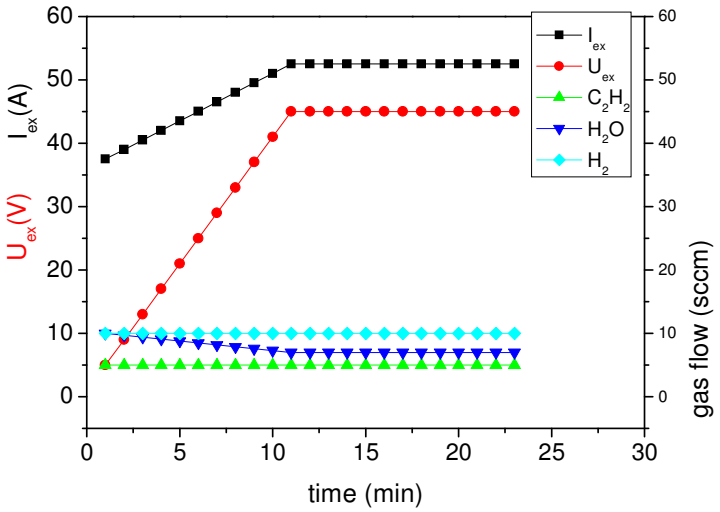


*Fig. III.12: Optimized growth parameters for the PECVD growth of CNTs on PAA structured samples. The gas pressure is fixed at 2 mbar, the distance between the second grid and the sample is 25 mm.*

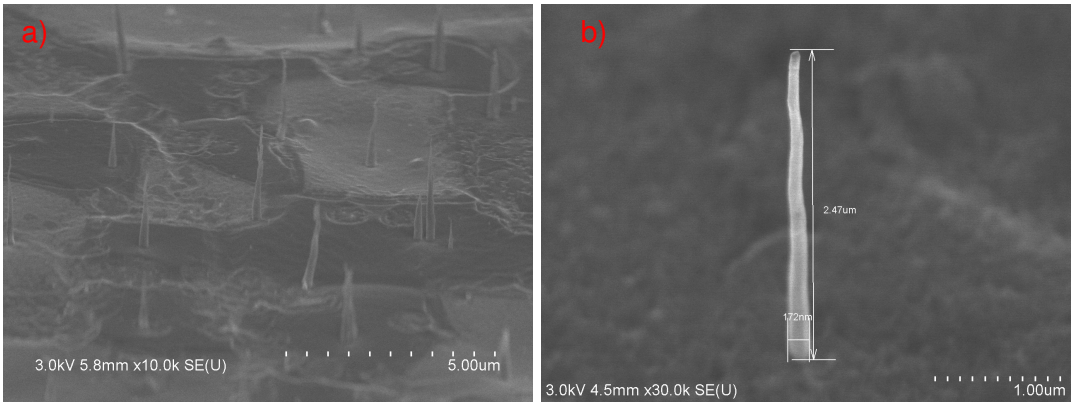


*Fig. III.13: CNTs grown under standard (a) and optimized conditions (b). The growth time was 35 min in both cases. The growth temperature was 575 °C.*

The difference between these two samples is evident: Under standard conditions, the CNTs are too strongly etched which leads to a very conic shape. Besides, the outer walls of the CNTs obviously contain much more impurities than in the case of the optimized growth conditions. Both properties are very important for possible applications like field emission, for which the conductivity (depends on the impurities), the durability (sharp tips are quickly destroyed by a high current density) and the shape (this will be explained in chapter III.3.4) are determining parameters. As it can be seen in the Fig III.11 and Fig. III.12 of the growth parameters, for the optimized

conditions, both $U_{ex}$ and $I_{ex}$ have been decreased, whereas $U_{ex}$ has been decreased much more in order to reduce the etching effect of carbon. Besides, for the optimized conditions, the ratio of $C_2H_2$ to $H_2O$ has been fixed at 5/7, whereas for standard conditions, the ratio has been 5/10=1/2. This was done to increase the amount of growth-active hydrocarbon radicals in comparison to the etching species created from $H_2O$.

After the discussion about the growth conditions, we describe the fine adjustment of the temperature ramp and the reduction process of the catalyst. The influence of the ramping and reduction process are shown in Fig. III.14.

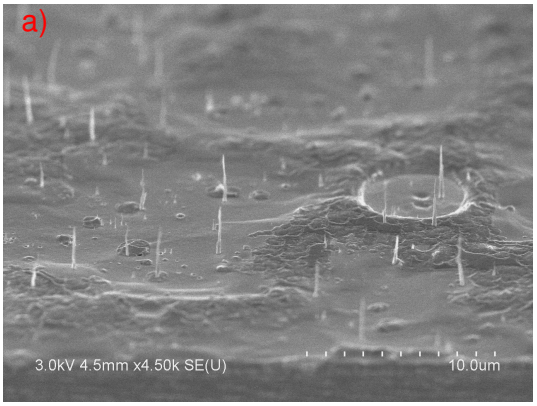


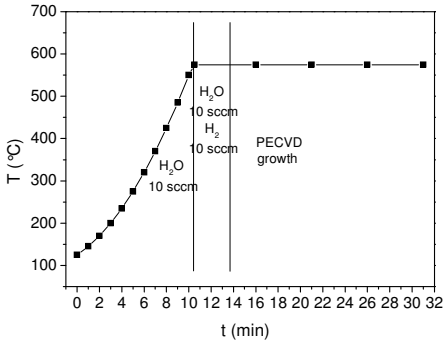


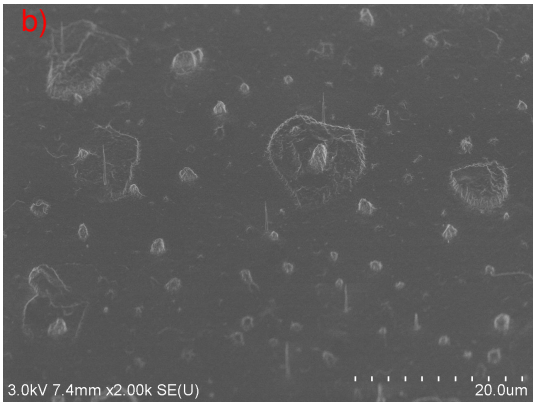


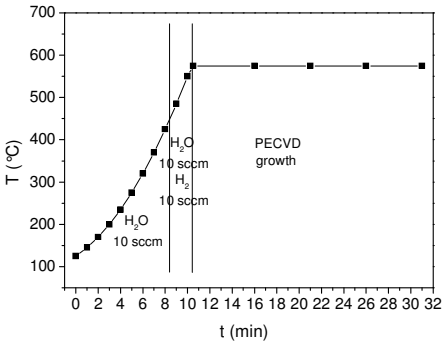


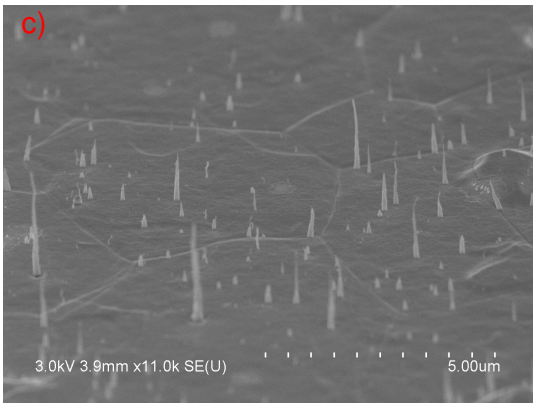


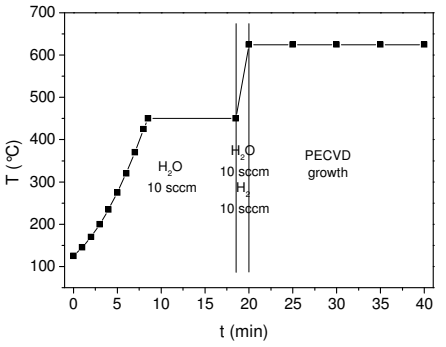

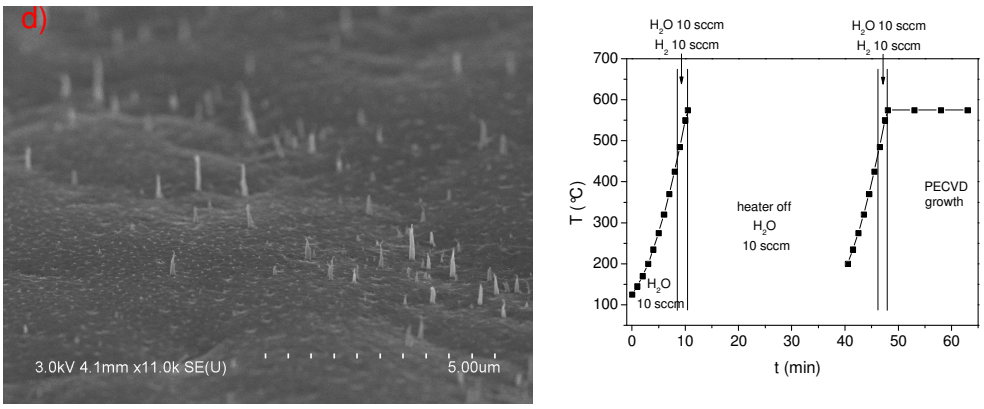


*Fig. III.14: SEM images of 45° tilted samples showing the influence of the different ramping and reduction conditions on the PECVD growth. All samples have been prepared with the same density and amount of nickel catalysts before the growth.*

The influence of the ramping and reduction conditions on the shape and the density of the CNTs is evident:

- In a), by applying the optimized conditions for the CVD growth inside PAA discussed in the last paragraph, the surface has become very rough during the growth which probably is due to the volume expansion during the oxidation of Al at high temperature, as in this case, the sample has been heated up to 575 °C under $H_20$ flow. However, the height and shape of the CNTs differs a lot. This can be explained by the partial diffusion of the catalyst into the Al, which poisons different catalysts in a different way, depending on the barrier layer thickness on which it is deposited (as shown in chapter I and II, the barrier layer thickness varies over the sample).
- In b), the oxidation has only been done up to T= 450 °C and the $H_2$ has been added up to T= 575°C. Then, the growth has been started immediately. On this sample, one can clearly see that the density of catalysts is smaller, probably due to the shorter oxidation. Besides, the CNTs are much more homogenous, which might be due to the fact that only catalysts on very thick barrier layers did not get poisoned by the diffusion.
- To prove this assumption, the sample has been reproduced in c) by only prolonging the oxidation time at T= 450 °C. In this case, again the CNTs are not homogenous. We think, this proves that the additional oxidation has inhibited the complete diffusion of several catalysts which have been the origin of truncated CNTs.

- The same effect can be observed for the double-ramping done for the growth in d): here, all CNTs are strongly truncated which indicates the poisoning of all catalysts due to the enlarged ramping and reduction process.

In summary, it has been found that the ramping and reduction process influence not only the properties (shape, impurities, ...), but also the density and homogeneity of the grown CNTs. The conditions shown in Fig. III.14 b) with a fast ramping and short reduction before the growth have been determined as the best conditions in terms of homogeneity and shape of the CNTs.

After having optimized both the ramping and reduction process, the determined parameters for the PECVD growth have been applied for the growth of samples with different catalyst densities, fabricated by the method described in paragraph II.3.3. The result for the CNT growth on samples fabricated with different time constants η of the anodization voltage and thus different catalyst densities are shown in Fig. III.15.

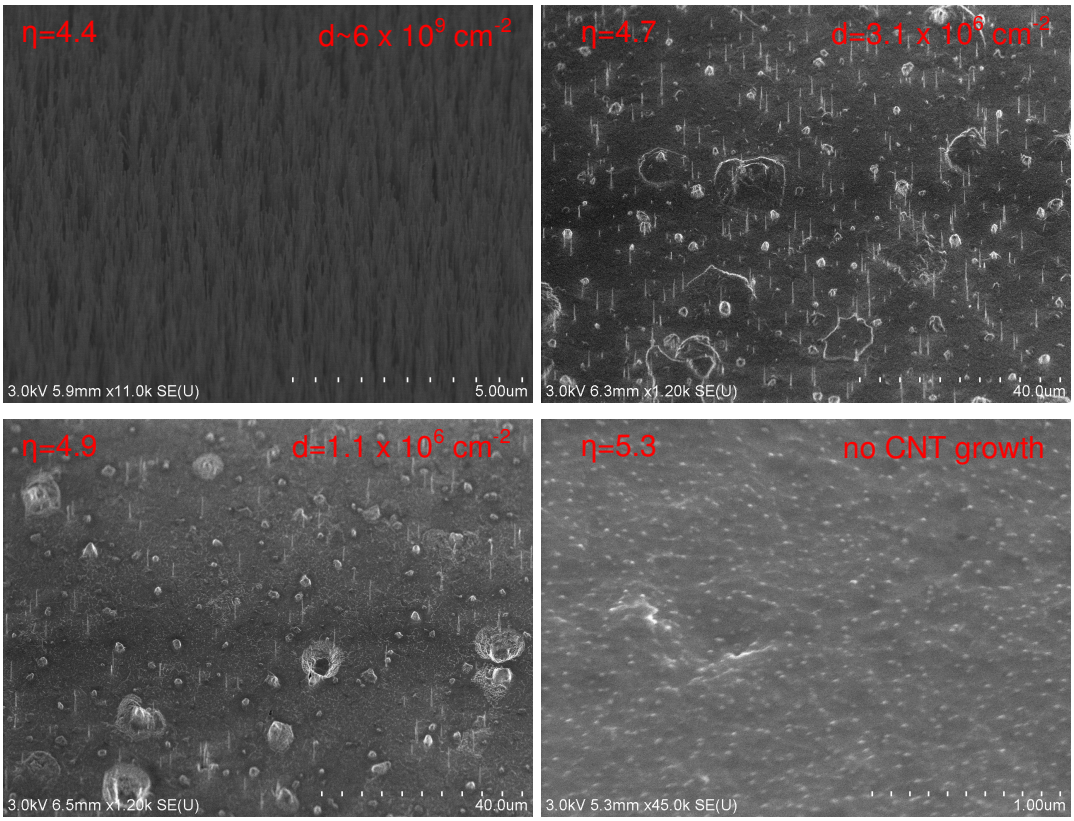


*Fig. III.15: SEM images of 45° tilted samples. CNTs have been grown on samples fabricated with different time constants η and a subsequent anodization voltage of - 4.5 V. The density d of CNTs is given for each η value.*

The difference of the CNT density in dependence on the different time constants η is clearly seen: The slower the voltage decrease (the lower η), the higher the CNT density.

For the samples shown in Fig. III.15, an electrodeposition voltage of – 4.5 V has been applied which is higher that the – 4.2 V applied for the study of the catalyst density variation in chapter II. The electrodeposition voltage has been increased in order to deposit rather on thicker barrier layers and thus to reduce the diffusion effect as far as possible.

However, for η=5.3, there is even no growth of CNTs anymore. For all samples, there is a high density of white spots on the surface. We believe that this indicates the position of nickel catalysts that have diffused into the aluminium due to the very small size of the catalyst.

## III.3.4 Field emission of CNTs grown on PAA structured samples by PECVD

### III.3.4.1 Field emission: an introduction

Field emission has been studied for more than hundred years and numerous applications have been realized with field emission devices [103]. Historically, the field emission has first been investigated from metal tips. During the last decades, the field emission from micron-size metal tips has largely been studied and today arrays of metal microtips fabricated by the well known Spindt-technique [104] are used for field emission displays (FED). FEDs and even more the application for backlights for active-matrix liquid crystal displays (AMLCD) are very realistic applications of field emission for industrial use in the close future. In the last decade, the field emission from MWCNTs has attracted large interest in the research community, as MWCNTs exhibit ideal properties for field emission devices like small diameter, high aspect ratio, high thermal and chemical stability and very good conductivity. The excellent field emission properties of MWCNTs have been demonstrated in different field emission devices [105, 106, 107]. However, for the realization of field emission devices based on CNTs, vertical aligned MWCNTs are needed that are uniformly

distributed on the surface with densities of $10^6$-$10^7$ $cm^{-2}$. The growth of CNTs by PECVD on PAA structured samples offers the extraordinary possibility to realize those CNT configurations without complex and costly lithography steps. In this chapter, after an initial theoretical argumentation for the interest of the use of our samples for field emission, first results of field emission measurements of such grown CNTs are shown.

### III.3.4.2 Field emission: principles

Field emission describes the emission of electrons from a material by applying an electric field. The emission takes place at ambient temperature and thus differs from the thermoionic emission for which the emitting sample is heated so that the energy of electrons inside the material can overcome the potential barrier at the surface. Therefore, the field emission is also called “cold emission”.

The field emission is based on the tunnel effect: if an electron is inside a quantum well with a potential barrier energy higher that the energy of the electron, the probability to find the electron outside the quantum well is not zero but decreases exponentially with the potential barrier. Consequently, the probability to remove an electron from a solid for a field emission application and thus the field emission current depend on the potential barrier for the electron, which itself depends on three different parameters:

a) the work function Φ of the specific material that emits the electrons;
b) the electric field energy, which the electron gains outside the material by the applied electric field;
c) the image potential due to the electrostatic charge that is created by the removal of the electron from the solid (hole) which exerts the Coulomb force on the electron.

The potential barrier and the three parameters are described in Fig. III.16, where V(x) is the energy of the electron corresponding to its position x.

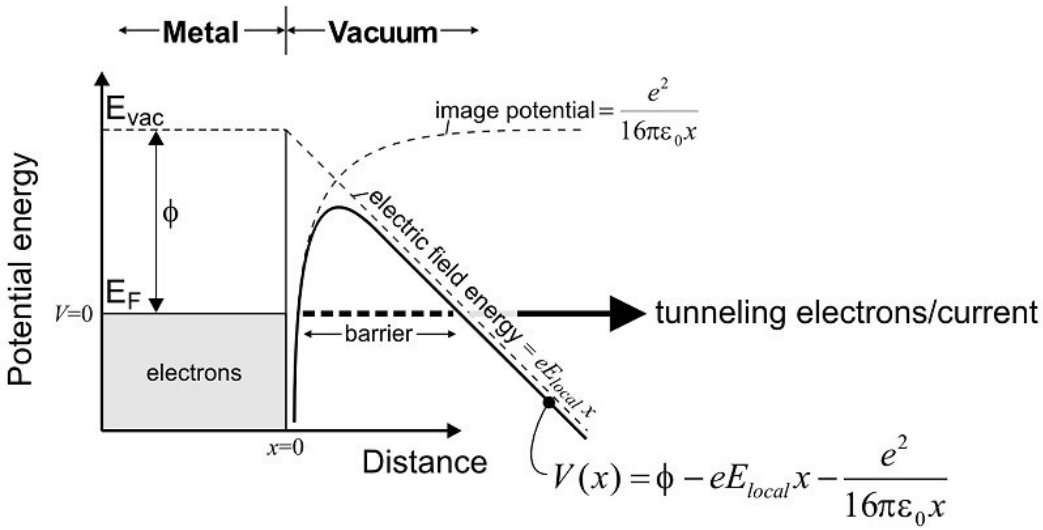


*Fig. III.16: Different parameters influencing the field emission of electrons from a metal.*

For the realization of field emission from a material, the work function and the local electric field are thus emission determining factors. In this respect, the geometry of CNTs and of the CNT arrangement is important:

The electric field streamlines density increase at curved surfaces. As the tip of CNTs shows a very strong curvature due to the low diameter of CNTs, the electric field is especially enhanced at the tips of CNTs. Besides, tips with high aspect ratio (diameter/height) lead to a high concentration of the electric field. CNTs therefore again are well suited as they can exhibit very high aspect ratios. By theoretical modelling it has furthermore been demonstrated that the ideal arrangement of field emitting tips is realized in a way that the distance between the tips is twice the height of the tips [108]. To give an example: for CNTs with a height of 2.5 µm, a density of $4*10^6$ $cm^{-2}$ is needed. Otherwise, for shorter distances, the enhancement of the electric field on one CNT due to the high aspect ratio is weakened by the neighboured CNT, which is called “screening effect”. For longer distances, i.e. smaller CNT densities, the field emission is lower as there are less electron emitters. Moreover, the high aspect ratio of CNTs is most efficient for the enhancement of the electric field at the tip of the CNT if the CNT is of a whisker shape and not conic.

The pioneering theoretical calculations for the probability of an electron to overcome the potential barrier in an applied electric field have been done by Fowler and Nordheim [109], who calculated the emission current density of an emitting surface depending on the applied electric field and the work function for a given temperature.

Although Fowler and Nordheim had done the calculations based on flat emitters, their calculations can easily be modified and adapted for tip emitters. The most common version in literature of the Fowler-Norheim equation is given by:

$$I(E) = S\frac{a}{\Phi}(\beta E)^2 \exp\left(-\frac{b\Phi^{3/2}}{\beta E}\right)$$

where S is the emitting surface,

a and b are constants,

E is the applied electric field,

Φ is the work function,

β is the enhancement factor

The enhancement factor β refers to the geometrical parameters of the field emission sample as described above. For ideal whisker-shaped emitters with a high aspect ratio, diameter (d) << height (h), the approximation $\beta=h/d$ is valid [110].

### III.3.4.3 The field emission measurements

The field emission measurements have been realized with the equipment and the support of Thales Research & Technology in Palaiseau using an UHV chamber whose set-up is shown in Fig. III.17.

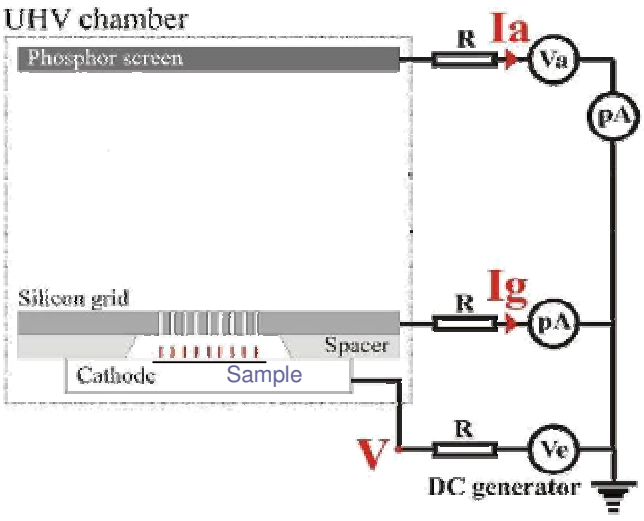


*Fig. III.17: Schematics of the field emission setup.*

The sample is mounted on the cathode and the potential *U* is applied between the silicon grid and the sample, which is separated by a quartz spacer of a thickness *d* =110 µm from the grid. The applied electric field *E* is thus given by *E=U/d*. The emission current is collected by a phosphor screen and the current is measured by a pico amperemeter.

In order to be able to measure the emission electron current density of the CNTs, a surface of 1 $mm^2$ of the CNT samples fabricated as described above has been determined by lithography. The sample preparation has been done according to the following steps:

1) A 200 nm thick $SiO_2$ layer has been deposited on the aluminium and an area of 1$mm^2$ has been opened in this $SiO_2$ layer by RIE with $SF_6$ as etching gas;
2) Thus, only in the 1 mm² area, PAA has been formed by anodization of the exposed 1 mm² Al area;
3) Nickel catalyst has then been deposited during a subsequent electrodeposition;
4) The PAA has been etched by chemical wet etching;
5) In order assure a conductive sample surface during the following PECVD growth and thus to avoid arcing and plasma instabilities during the growth, the $SiO_2$ layer, which was still present at the sample surface around the 1 mm² area, again has been etched by RIE. During this last step, we had to apply a very low RIE power of 20 W, as a higher RIE power leads to surface damages and therefore rough surfaces.

The field emission has been measured on such samples and the best field emission results has been obtained on a sample corresponding to the optimized growth conditions in the last chapter, and with a catalyst deposition of -4.5 V after the PAA fabrication with a time constant of η=4.9 (CNT density $1.1*10^6$ $cm^{-2}$, CNT length ~2.5 µm).

The sample and the field emission measurements are shown in Fig. III.18.

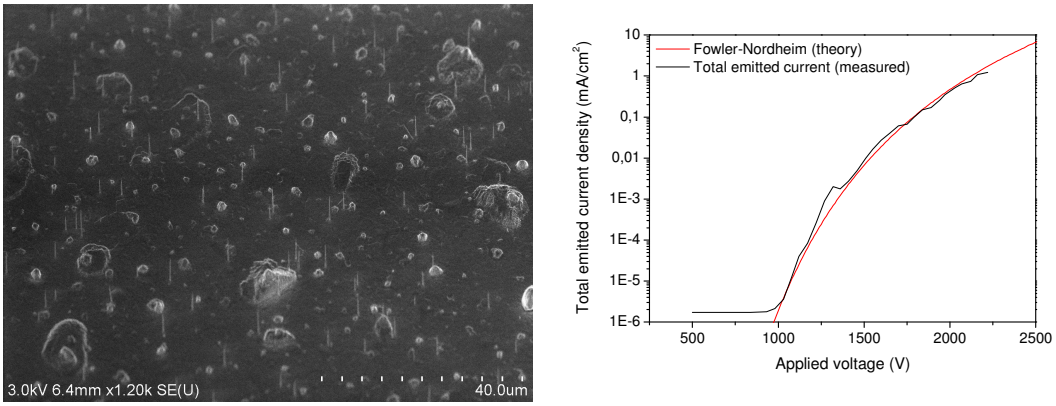


*Fig. III.18: SEM image and field emission of a CNT fabricated by PECVD on a PAA structured sample.*

Although the field emission current of the order of 1 mA/cm$^2$ at about 30 V/µm is close to the necessary values for backlight applications and comparable to the results obtained for the field emission of random metal nanowires devices, it is still far smaller than the values obtained for CNT arrays organized by lithography. In our group, such CNT arrays fabricated by $H_2O$ assisted PECVD typically achieve field emission currents of about 14.3 mA/cm$^2$ [111]. This important difference can be explained by several reasons:

a) Although the growth and ramping conditions have precisely been optimized, still the surface roughness of the samples is not negligible which disturbs the concentration of the electric field on the CNT tips.
b) The random organization of the CNTs is by far not as efficient as the organization by lithography. Thus, the screening effect is much higher in case of the PAA based CNT arrays.
c) The poisoning of the catalyst by the diffusion through the barrier layer seems to be the crucial problem for the CNT growth on the PAA structured samples, which leads to CNTs of different heights and thus a non uniform distribution of the electric field and of potential emitters over the sample.

The next step for the optimization of the field emission characteristics of CNTs fabricated by the applied PAA structuring method is the increase of the barrier layer thickness under the catalyst in order to avoid the poisoning of the catalyst. This can only be done by establishing a new final voltage for the PAA fabrication and to study different catalyst densities for different electrodeposition voltages before the PECVD

growth. The increased thickness of the barrier layer might also allow a slower ramping and an earlier addition of the reducing $H_2$ gas during the growth which might also diminish the surface roughness after growth.

## III.4 Conclusion

We have established reproducible growth conditions of the growth of CNTs inside PAA membranes and on PAA structured surfaces. This paths the way for future research on PAA based CNT devices.

The research activity in this work was based on the know-how in our group concerning the growth of CNTs by CVD and PECVD on plane substrates. With an attentive optimization study of the growth parameters, the growth recipes established for planar substrates have been adapted for the growth inside PAA and on PAA structured surfaces. It has been shown that the principle problem for a reliable growth of CNTs on such substrates is the realization of low temperature growth and the treatment of the catalyst during the reduction process and the growth itself.

With the growth conditions established in this work, different CNT organizations could be achieved: On the one hand a high density growth of CNTs inside the vertical PAA, on the other hand vertical aligned CNTs at different densities on a conducting substrate.

A first application for the growth techniques established in this chapter has been demonstrated with a field emission device. Although, so far, the field emission based on PAA structured surfaces has not been in the range of the field emission based on samples structured by lithography techniques, it has shown to be an interesting alternative way to obtain cost efficient field emission devices.

# CHAPTER IV

# PAA AS ETCHING MASK

# IV. PAA as etching mask

## IV.1 Introduction

In the recent development of semiconductor industry, the lithography in the nm-range has become important for today's devices. By the end of 2009, the 32 nm CMOS technology will be commercially available, which demonstrates the huge demand for ultra high resolution lithography.

This increasing demand has led to strong research activity in the field of very high resolution lithography. The resolutions applied today for very small structures are either based on optical (extreme UV, 'EUV'), X-ray or e-beam lithography. Although these technologies offer great possibilities (by e-beam lithography, linewidths around 10 nm can be realized), they require very complex systems and are very costly, as not only the resolution given by the used wavelength, but also the used photoresist and development technique must comply with highest requirements.

For this reason, the nanostructure formation by self organization offers a very interesting alternative to common lithography steps. Usually, self-organization is used for a self-arrangement of single particles in a single layer. In order to replace lithography steps in a device fabrication process and thus to reduce process costs, it is especially interesting to realize a first self-organized layer which can then serve as a mask and allow the transfer of the self-organized structure inside one or several sublayers.

In this respect, PAA membranes are of unique interest for the use as etching mask. One the one hand, PAA has the already mentioned advantages of easily adjustable pore diameters, low costs and the compatibility with CMOS technology, on the other hand, PAA moreover consists of alumina which resists to a wide range of etching processes and thus is especially suited as mask.

# IV.2 Patterning with a PAA mask: an overview

## IV.2.1 Patterning with a PAA mask: state of the art

As the advantages of PAA as mask are evident, there has been a strong research in this field in the last years. The main difficulties consist in the anisotropic etching and the interface between the PAA and the subsequent layer, as the barrier layer hinders the direct access to a possible underlayer. There are two possibilities to overcome this problem:

Either, the PAA is fabricated independently and then is mounted on the sample with the barrier layer at the top. The barrier layer is thus exposed to the surface and can easily be etched to open the pores at the surface before a subsequent etching process.

Or, the PAA is directly fabricated on the sample by anodizing a thin Al layer at the top of the structure. In this second case, either a conductive underlayer is required in order to realize an open pore structure, or the anodization is stopped inside the Al layer and the barrier layer must be etched by a highly anisotropic dry etch.

In the following, an overview over different approaches of patterning by PAA in the literature is given.

a) One possibility is the transfer of the order of PAA by using the imprint method [112]. In this case, the PAA is fabricated independently of the layer that is to be structured, starting from bulk aluminum. Then, the entire aluminum-PAA-sample is used to realize imprints in PMMA (poly methyl methacrylate) by x-ray illumination which can then be transferred to subsequent underlayers. Although this method is quite cost efficient and reliable, it is difficult to achieve high aspect ratios and small pore diameter structures.

b) The independently fabricated PAA can also be used for a following ICP dry etch process [113,114,115]. In this case, the PAA is mounted on any sample and the order of PAA is transferred into the surface of the sample by anisotropic dry etch. This method has successfully been adapted for the realization of nanohole surfaces with low aspect ratios [113] and also for high aspect ratio structured surfaces [115]. Following the same principles, also surface patterning by ion-beam-etching (IBE) has been achieved [116].

Although this technique is quite promising, the handling of the PAA membranes is difficult and therefore a time and cost intensive step.

c) PAA can also directly be realized on a conducting sublayer like Si and then be used for a structuring of this underlayer by dry-etching [117,118]. A nanodot structured surface of Si could be obtained by this method, where the aspect ratio of the realized Si-pattern has been very low. One reason for this is the weak adhesion of the alumina membrane on the sublayer (Si), which is inherent in the structure, since the volume expansion during the anodization weakens the interface between the PAA and the sublayer.

d) A good alternative for the etching across the PAA-mask is the direct anodization of the conducting underlayer after having anodized the entire Al-layer. Asoh et al. [119] anodized an Al layer deposited on Si and then observed precisely the anodization current at the interface. A strong, rapid current increase referenced the anodization of the Si-surface, which resulted in ordered $SiO_2$-nanodots on the Si-surface. These nanodots themselves could serve as etching mask.

e) The highest aspect ratio can be achieved, if the anodization is stopped inside the Al and the order then is transferred inside the Al-bulk [120]. This technique implies the initial etching of the barrier layer and then a subsequent Al-etching, which makes it difficult to control the real Al-etch rate.

### IV.2.2 PAA as etching mask: the research in this work

In contrast to the so far realized patterning by using PAA as mask, the goal in this work was namely the realization of a high aspect ratio nanoporous multilayer and not only the structuring of surfaces. The favoured structure should be adapted for a localized growth of nanostructures like CNTs and SiNWs and at the same time offer the possibility to contact these nanoobjects in respect to their characterization and to a device fabrication. One possible application for the porous multilayers, whose realization will be demonstrated in annexe A, is the vertical transistor based on CNTs or SiNWs. The principles of this possible device will be discussed in annexe A.

For this ambitious goal, the adhesion of the PAA layer on the sample, the stability of the sample and the reliability of the etching process are very important. Thus, the

PAA membrane has always been fabricated directly on the sample and then has served as etching mask. For that purpose, an Al layer has been evaporated on the respective sample and then the Al has been anodized to create an ordered porous top-layer.
The easiest and most stable stacking, of course, is achieved, if, like in the previous paragraph IV.2.1.e), the ordered structure is first transferred inside the Al-layer under the PAA. Consequently, this structure has widely been studied in this work, the results of the etching inside the Al and inside the following underlayer has been the major part of our research and will be discussed in IV.3.3.

By an another approach, we have realized an open-pored PAA structure on n-doped polycrystalline Si and studied the etching behaviour inside this layer and the following underlayer. This will be discussed in IV.3.4.

## IV.2.3 Anisotropic dry etch

In the semiconductor technology, the anisotropic dry etch is of remarkable interest, as this technique offers, in contrast to the wet etching processes, the possibility to realize structures with a high aspect ratio and with clean, straight etched sides. The dry etching process therefore is a well known and well established technique [121,122].
Within the anisotropic dry etch one must distinguish between the Ion Beam Etching (IBE) and the Reactive Ion Etching (RIE). The IBE rather acts like a sputtering process, an ion (often Ar) is accelerated to the sample and thus removes matter by its kinetic energy, or, better said, by the transfer of momentum. The RIE is very similar to the IBE, but in this case, chemical reactive ions or radicals are used for the bombardment of the sample. It thus combines the advantages of chemical etching (selectivity, clean surfaces) with those of the IBE (anisotropy) and therefore is the method of choice for anisotropic etching of any material.

### IV.2.3.1 Reactive Ion Etching: principles

The Reactive Ion Etching (RIE) is based on a plasma process.
A plasma [123] is defined as a partially ionized gas that contains a significant number of charged and neutral particles. Usually, a plasma consists of molecules, radicals,

atoms and charged particles like electrons, positive and negative ions. A plasma is always quasi-neutral and exhibits a collective behaviour. To create a plasma, energy has to be coupled in a gas, and the plasma is generated and maintained by collisions between its constituting elements. It presents a difference to the three common states of matter (solid, liquid, gas). Therefore, the plasma is also called “the forth state of matter”. The characteristic parameters of a plasma are the energy of its elements, the plasma density and its temperature. The high temperature (in terms of a thermodynamic equilibrium this is the average energy of free particles) of its constituting elements is a main characteristic of the plasma. The plasma density $n$ hereby is defined as the density of the positive ($n_p$) or negative ($n_n$) particles, which in general are equal due to the quasi-neutral behaviour of the plasma: $n=n_p=n_n$. According to their characteristic parameters, plasmas can differ from each other in a very wide range. For a RIE process, only low pressure plasmas are of interest. These plasmas are commonly called non-LTE plasmas (non local thermal equilibrium), as the light electrons have a much higher temperature (about $10^4$ K) than the heavy ions and neutrals (about RT). The plasma densities are in the range of $10^8$-$10^{13}$ $cm^{-3}$. Non-LTP plasmas are widely investigated and used for surface structuring processes, namely in the semiconductor industry.

For an RIE process, a plasma is created in a process chamber in which the target, i.e. the sample, is positioned. The plasma parameters are hereby determined by a complex interaction between the chamber pressure, the energy that is coupled into the plasma, the gas flow, the chamber and target temperature and the geometry of the chamber. In RIE reactors, the species are accelerated to the surface of the target and thus produce a bombardment that is perpendicular to the target’s surface (see the following paragraph for details). The plasma species interact both physically and chemically with the target. The kinetic energy and the transfer of momentum of the ions are responsible of the physical interaction and the activated radicals and ions of the chemical interaction on the target. In most cases, the etching gases are chosen in a way that chemical reactive ions react with the target surface and build volatile products. Combined with the anisotropic sputtering effect, the etching leads to high aspect ratios and clean facets can be achieved. As there is no deposition on the etched sides, the structures are not clogged.

### IV.2.3.2 RIE and ICP

The basic chamber for a RIE process consists of two electrodes (see Fig. IV.1).

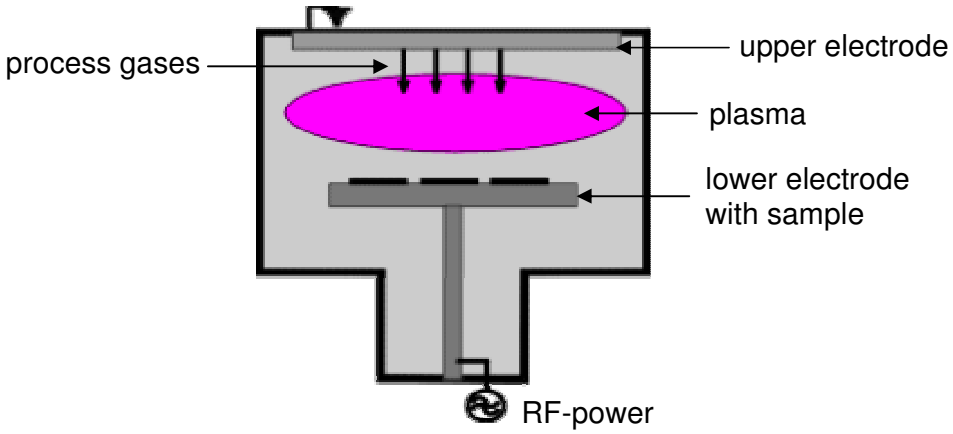


*Fig. IV.1: The RIE reactor*.

The etching gases enter the chamber through the upper electrode, the sample is mounted on the lower electrode. An RF voltage (generally 13.56 MHz) is applied between the two electrodes and creates the plasma inside the chamber. By applying an RF voltage, it is guaranteed that the positive ions inside the chamber are accelerated towards the walls of the chamber and the sample, which enables the vertical, anisotropic etching process. This effect will be explained in the following.
The driving frequency of the plasma $\omega_{rf}$ is defined by $\omega_{rf}=2\pi f_{rf}$ while $f_{rf}$ is the frequency of the applied RF voltage. In case of an applied RF voltage, the relation between the plasma frequency $\omega_{rf}$, the electron plasma frequency $\omega_{ep} = \sqrt{\frac{n_e e^2}{m_e \varepsilon_0}}$ and the ion plasma frequency $\omega_{ip} = \sqrt{\frac{n_i q^2}{M_i \varepsilon_0}}$ is given by: $\omega_{ip} << \omega_{rf} << \omega_{ep}$. This means, that inside the plasma, only the electrons follow the applied electric RF field, whereas the ions cannot follow the fast change of the electric field due to their high inert mass. Therefore, only the electrons move inside the RF plasma. The electrons thus move towards the surrounding surfaces of the plasma and leave a positive plasma bulk, the quasi-neutral state of the plasma does not exist anymore at the surfaces of the electrodes and the chamber walls. If the electrons hit the surrounding surfaces, these potentially floating surfaces get negatively charged. This negative charge repels

electrons and attracts the positive ions that move towards these surfaces. Finally, an equilibrium is established in which the surface has a stable negative potential. This potential, which occurs naturally in RF plasmas without applying an external bias, is called “self-bias”. Close to the self-biased negative charge, the density of positive ions is higher than inside the bulk plasma. The resulting positive charge region is called “sheath”. For the monitoring of the plasma etching process inside an RIE, especially the self bias and the peak-to-peak voltage at the RF-driven sample electrode are important. The self bias refers to the kinetic energy of the ions that bombard the sample, the peak-to-peak voltage indicates the potential variation on the sample during one RF-cycle [124,125].
In summary, the ions do not move along the applied electric RF field, but move along the established static field close to the floating surfaces. The surface of the sample is one of those floating surfaces, which allows to obtain a flow of ions that is perpendicular to the surface of the sample.

The ICP (Inductively Coupled Plasma) reactor (Fig. IV.2) is similar to the basic RIE reactor but delivers some crucial advantages. In such reactor, the plasma is not created between two electrodes, but is created by an antenna through induction. The antenna is driven by an RF signal of a given power, which is called the “coil-power”. In addition to the coil-signal, a second RF signal is applied on the sample electrode. This power of this second signal is called “platen-power”.

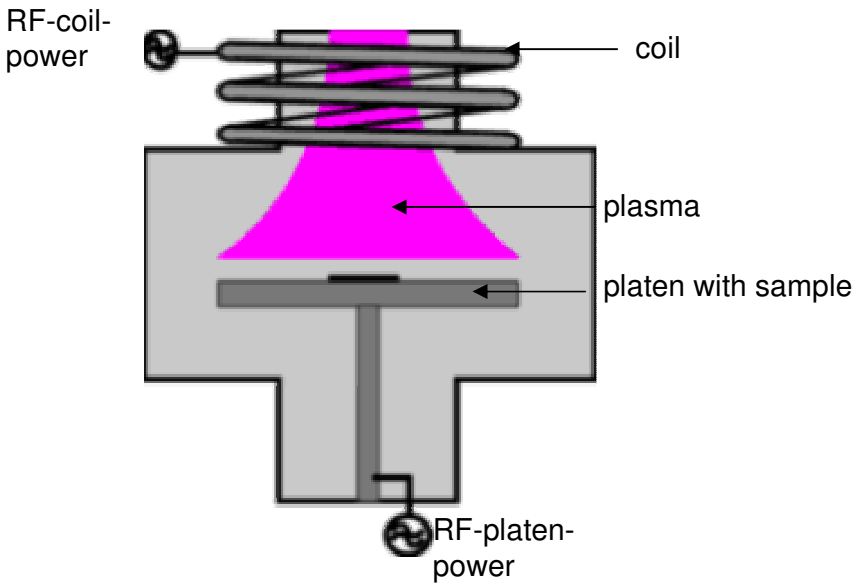


*Fig. IV.2: The ICP reactor.*

The main advantages offered by an ICP system in comparison to the basic RIE system is the decoupling of the creation of the plasma from the biasing of the sample. The plasma density and temperature is mainly determined by the coil power, the self-bias and the peak-to-peak voltage are mainly determined by the platen-power, although, of course, both platen-power and coil-power influence on the entire setup.
Due to this decoupling, the ICP reactor is especially well adapted for low-pressure and low-bias etching processes and is able to combine high plasma densities with very good homogeneity.
In this work, all etching processes have been realized with an ICP reactor. This offered the best possibilities to achieve a low-energy, highly anisotropic etch.

## IV.3 Experimental: Results and discussion

### IV.3.1 The etching setup: The ICP reactor

All etching processes that will be discussed in the following have been realized on a commercial *Multiplex STS* ICP reactor (Fig. IV.3). In this reactor, the plasma is created by an RF power in an inductive coil which is automatically matched with the RF power applied on the platen. A 6” wafer serves as sample holder and the sample is automatically charged via a load-lock. Inside the chamber, the 6” wafer is put on the platen electrode which is lifted up to circular surrounding clamp fingers which press the wafer on the platen electrode. This electrode allows a flow of liquid helium at the back of the wafer which cools the wafer and thus the sample during the etching process in order to avoid strong heating of the wafer due to the etching during which heat energy is created by chemical and physical reactions.

In the *Multiplex STS* reactor, the platen-power can be varied between 0-300 W, the coil-power between 0-600 W. The plasma etching process can be monitored by the self-bias and the peak-to-peak voltage. The impedances in the electrical circuits are adjusted automatically by an integrated matching box.
Inside the reactor, the following gases can be used as process gas:
$Cl_2$, $C_4F_8$, $SF_6$, $CHF_3$, Ar, He, $O_2$

A very important detail during the etching process is the used sample holder, i.e. the used 6” wafer. The wafer must withstand the etching processes and should be well conducting with an insulating layer at the side which is exposed to the plasma. Thus, on the one hand, the wafer does not constitute an additional resistance to the circuit, on the other hand the electrode should not be in a direct contact to the plasma as this results in huge peak-to-peak voltages (since the impinging electrons get immediately absorbed by the electrode) and thus makes a stable etching difficult. Corresponding to the used gases, either a p-doped wafer with 5 µm $SiO_2$ layer or an Al wafer with an $Al_2O_3$ layer has been used as sample holder.

a) b)

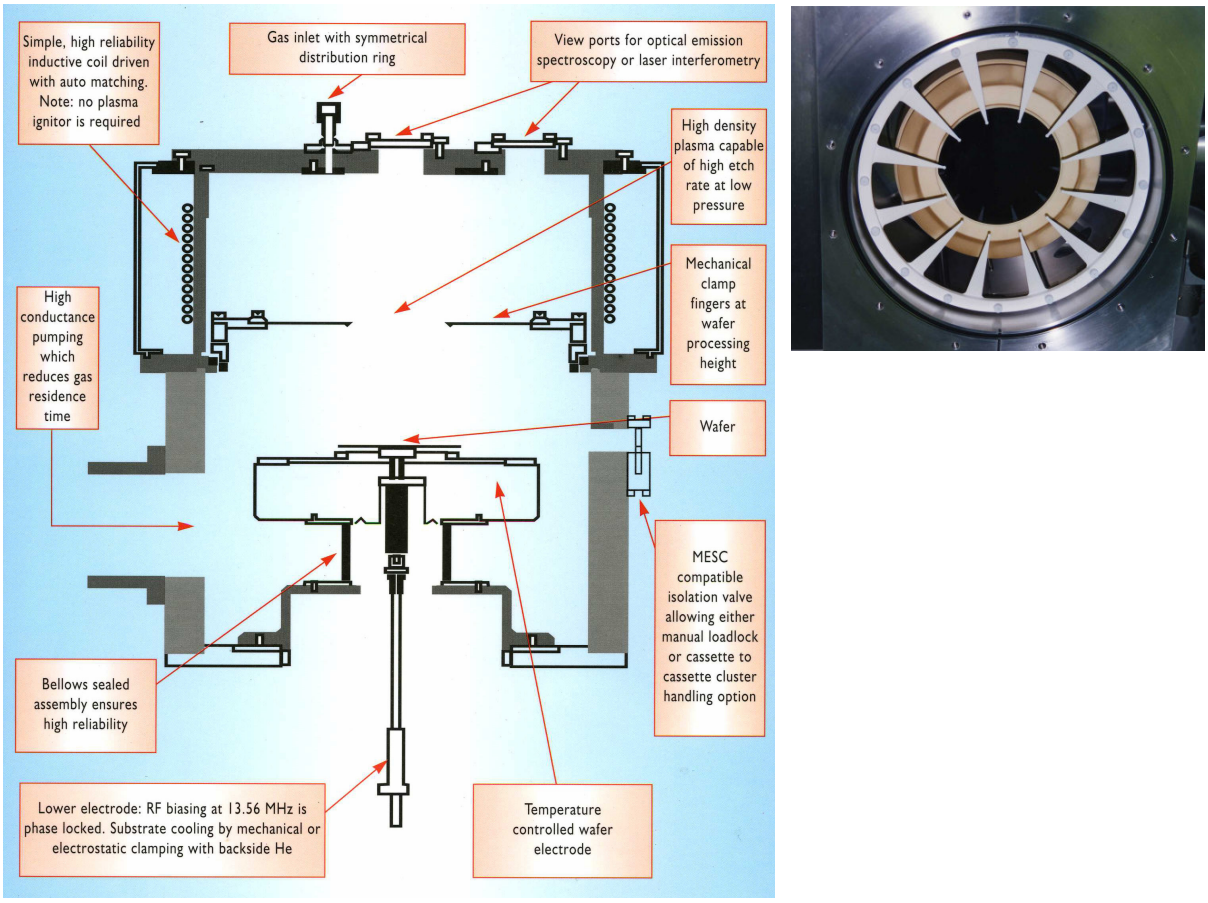


*Fig. IV.3: The ICP system STS Multiplex. In a), a schematical drawing of the ICP system is shown. In b), a topview on the sample holder is shown. This picture has been made after having removed the upper stainless steel plate with the gas inlet and it shows the mechanical clamp fingers and the sample holder. The samples are mounted on this 6 " wafer sample holder.*

## IV.3.2 Mask preparation

In order to assure a good transfer of the etching ions, all masks have been fabricated via a two step anodization at 1 °C which leads to a PAA structure with straight pores (see paragraph I.3.3).

For the etching process, the height of the PAA membrane is very important: On the one hand, the membrane has to serve as mask during several subsequent etching processes and thus has to be sufficiently thick, since during each etching process, also the PAA mask itself is etched. On the other hand, the thicker the membrane, the less ions will be able to transfer through the membrane without interactions with the pore walls and then contribute to the etching of the sample

under the PAA mask. Thus, the PAA thickness might influence the etching behaviour inside the sample. Consequently, to get reliable results, the membrane thickness has to be constant during any study of etching conditions.

This thickness is linked with the first anodization and the thickness of the possibly present Al-layer under the PAA mask. The precise control of the alumina formation rate, which has been discussed in paragraph I.3.2, is very important as it determines the reliability and the stacking of the final sample structure.

The fabrication of the PAA mask was done in several steps (see Fig. IV.4):

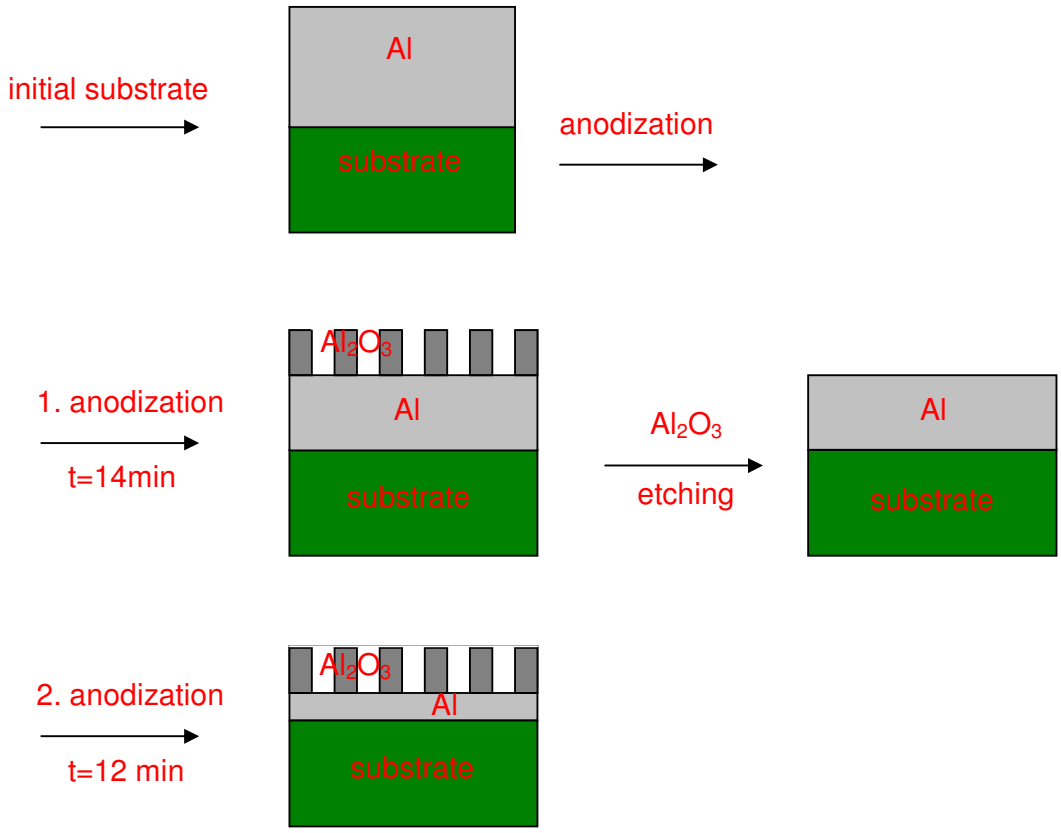


*Fig. IV.4: Preparation of a PAA mask.*

Starting from a Al layer that is deposited on the sample, a first anodization is carried out. The Al layer thickness that is present under the PAA during the first anodization depends on the thickness of said PAA: The thickness of the Al layer is reduced by the thickness of Al that has been oxidized during the first anodization. Then, said PAA is removed by chemical wet etching and the second anodization is carried out on the remaining Al layer. The duration of the second anodization therefore determines the thickness of the PAA mask, and the duration of both anodizations,

both first and second anodization, determine the thickness of the remaining Al layer under the PAA mask.

A very crucial point during the mask preparation is the homogeneity of the Al thickness over the entire anodized area, as in the following etching processes, a slight initial inhomogeneity of the Al thickness can lead to strong etching inhomogeneities in the sublayers. This will be discussed in detail in paragraph IV.3.3.2.

In the following paragraph, the main investigations have been performed out on PAA masks with 50 nm diameter pores. Also, to show the possible applications for a wide range of diameters, some etching demonstrations have been made with PAA masks with 20 and 180 nm diameter pores. These samples have been prepared in sulphuric and phosphoric acid, respectively, whereas the 50nm-pore masks have been prepared in oxalic acid.

## IV.3.3 PAA-mask on Al for multilayer etching

### IV.3.3.1 The etching inside the Al layer

*IV.3.3.1.1 The optimized etching process*

The sample before etching consists of a PAA membrane at the fop of the structure, a subsequent Al layer and the following sublayers (see Fig. IV.5).

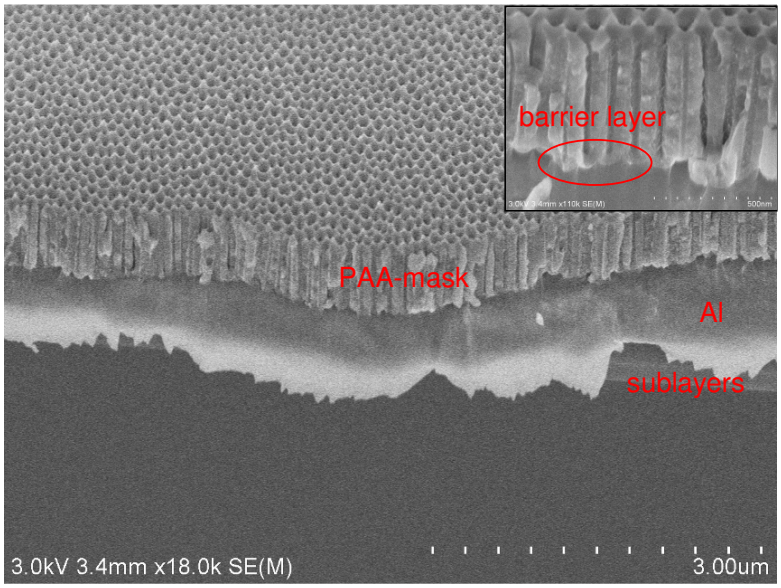


*Fig. IV.5: Cross section of a sample showing the PAA mask on Al.*

In Fig. IV.5, it can be seen that, after having realized the PAA mask, the thickness of the Al cannot be measured by SEM, as the Al cannot be cleaved correctly but shows the behaviour of a bent foil. As already mentioned in paragraph IV.3.2 the only way to determine the thickness of the Al underlayer is the strict method of mask preparation described there.

In general, for dry etching processes of Al, Cl containing gases are used, such as $SiCl_4$, $BCl_3$ or $Cl_2$ as the Cl reacts with Al [126,127]. The dominant overall reaction at temperatures below 200 °C is described as:

$2\ Al + 3\ Cl_2 \rightarrow Al_2Cl_6$

with $Al_2Cl_6$ as a volatile product.

If pure $Cl_2$ is used as etching gas, like in our STS ICP system, the etching is rather isotropic due to the fast chemical reaction and the small mass of Cl. In order to

assure a high anisotropy, an ion bombardment must be present. In the ICP system used in this work, this was realized by the dilution of $Cl_2$ in Ar. The ratio between Ar and $Cl_2$ is one of the most important parameters of the etching process [128] and will be discussed later in this chapter.

The etching parameters have been chosen in respect to a highly anisotropic etching process. The most important parameters of ICP etching are the coil-power, the platen-power, the chamber pressure and the gas ratio. The influence of each of them will be discussed in detail later, but first, a rough description about the range of the chosen values of each parameter is given.

For an anisotropic etch, it is important that the ions bombard the surface in the vertical direction. Thus, collisions between the ions must be avoided as far as possible, which, above all, requires a low chamber pressure. The chamber pressure for the Al etching operation has been fixed to the lowest possible value that could be attained in the ICP system, which has been 3 mTorr. Moreover, to keep the plasma density low and thus to avoid collisions between the ions in the plasma, which always change the direction of the movement of the ions, the coil-power has been maintained at small values. However, the density depends also on the platen-power as both platen and coil power influence the plasma. The platen-power itself has been fixed at high values in order to assure a high kinetic energy of the bombardment and thus to avoid the isotropic etch by $Cl_2$.

In Fig. IV.6, the result of an optimized Al etch is demonstrated: the high anisotropy and the high aspect ratio of about 15 can clearly be seen, as well as the transfer of the ordered porous structure inside the Al layer.

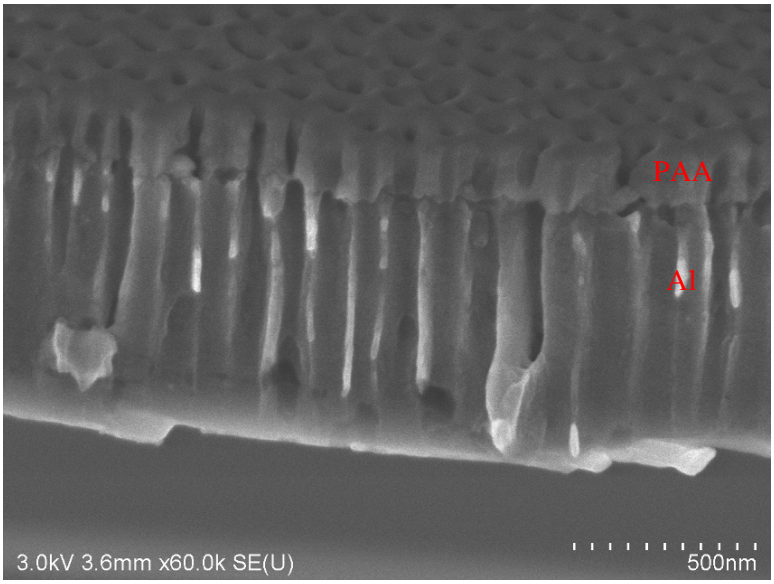


Optimized etching parameters:

pressure: 3 mTorr

flow $Cl_2$/Ar: 4/8 sccm

coil-power: 95 W

platen-power: 245 W

etching time: 13 min

*Fig. IV.6: Optimized Al etch.*

With the optimized etching conditions, the transfer of pores can be realized for a wide range of pore diameters. Examples for 20 and 180 nm pores are given in Fig. IV.7.

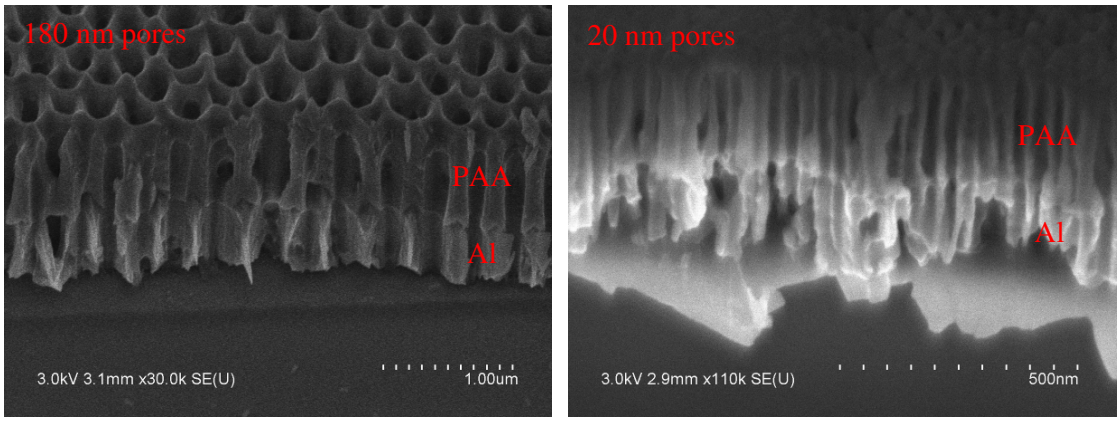


*Fig. IV.7: Transfer of a porous structure of different pore diameters into the Al layer.*

*IV.3.3.1.2 The role of the barrier layer during the etching process*

Apart from the high anisotropy that is required for the etching process, the transfer of the pores inside the Al can only be done after having etched the barrier layer at the pore bottom to get access to the Al underlayer. This has been a great challenge for the first etching experiments, as only after having etched the barrier layer, which consists of alumina and thus is very rigid and difficult to etch, the etching

process can be analyzed in respect to the etching rate and behaviour inside the Al. Besides, the etching rate at the pore bottom is much smaller that at the surface, so that the PAA mask is strongly thinned during the barrier layer etching. In this work, under the optimized etching conditions, the etching rate of the alumina at the surface has been determined to be about 15 nm/min, the one at the pore bottom to about 1.5 nm/min. For this reason, the barrier layer has been thinned by the pore widening process (i.e. wet chemical etching) described in chapter I before the ICP etch. The pore widening process is an isotropic etching process and thus removes the same thickness of alumina at the pore bottom as at the pore walls and the PAA surface. The duration of the pore widening process thus plays an important role for the subsequent etching process as it also changes the pore diameter and the thickness of the pore walls. The pore diameter might influence the etching rate inside the Al, as it influences the transmission of the etching ions through the PAA mask. The thickness of the pore walls is important for the adhesion of the PAA mask on the finally porous Al layer.

In Fig. IV.8, etched samples after different pore widening duration $t_{p.w.}$ and the respective etching depths are shown. All samples are etched under the optimized etching conditions.

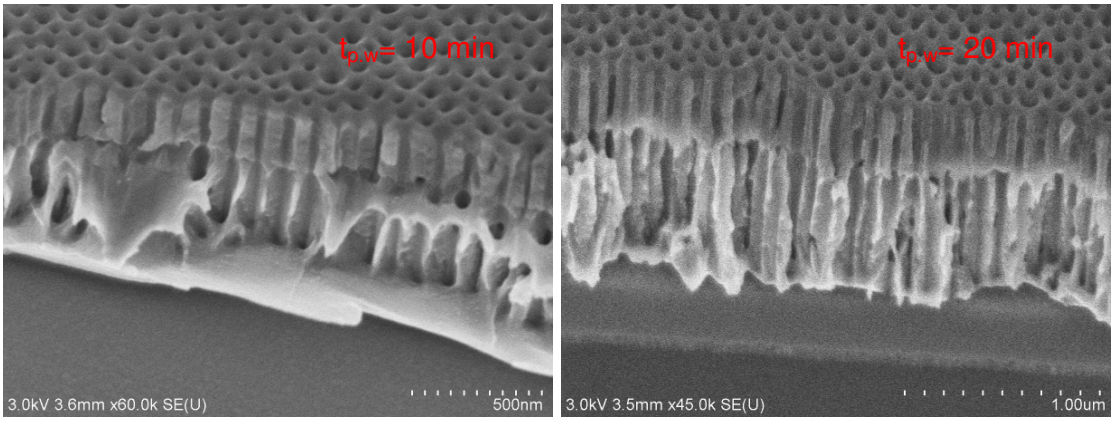

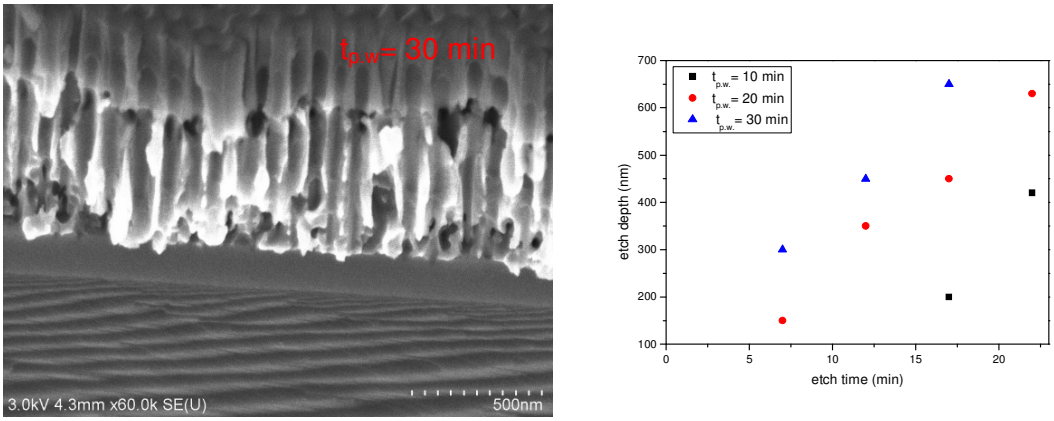


*Fig. IV.8: Etched samples with different pore widening durations.*

In Fig. IV.8, one can clearly observe, that the pore walls inside the Al are getting much thinner in the case of higher pore widening durations. The adhesion of the PAA mask on the Al layer is still good, even in the case of $t_{p.w}$=30 min, but in terms of stability of a multilayer structure, certainly a lower $t_{p.w}$ is favourable.

A very interesting effect can be observed for the etching rate. With shorter $t_{p.w}$, the etching inside the Al layer starts later, as first the barrier layer has to be etched. For the optimized etching conditions, anyway, the etching rate inside the Al layer is the same for all different $t_{p.w}$, which indicates the vertical flow of the ions and the high anisotropy of the etching process. Once the barrier layer is etched, the etching rate is about 20 nm/min.

*IV.3.3.1.3 The influence of the etching parameters*

In the following, the influence of the most important plasma parameters, the coil-power, the platen-power and the gas ratio are discussed.

Influence of the platen-power

The platen-power is responsible for the acceleration of the ions towards the sample. Consequently, it influences both the anisotropy of the process and the kinetic energy and thus the shape of the etched sides and the etching rate.

In Fig. IV.9, samples etched with different platen-powers are shown. The table in Fig. IV.9 summarizes the observed etching characteristics.

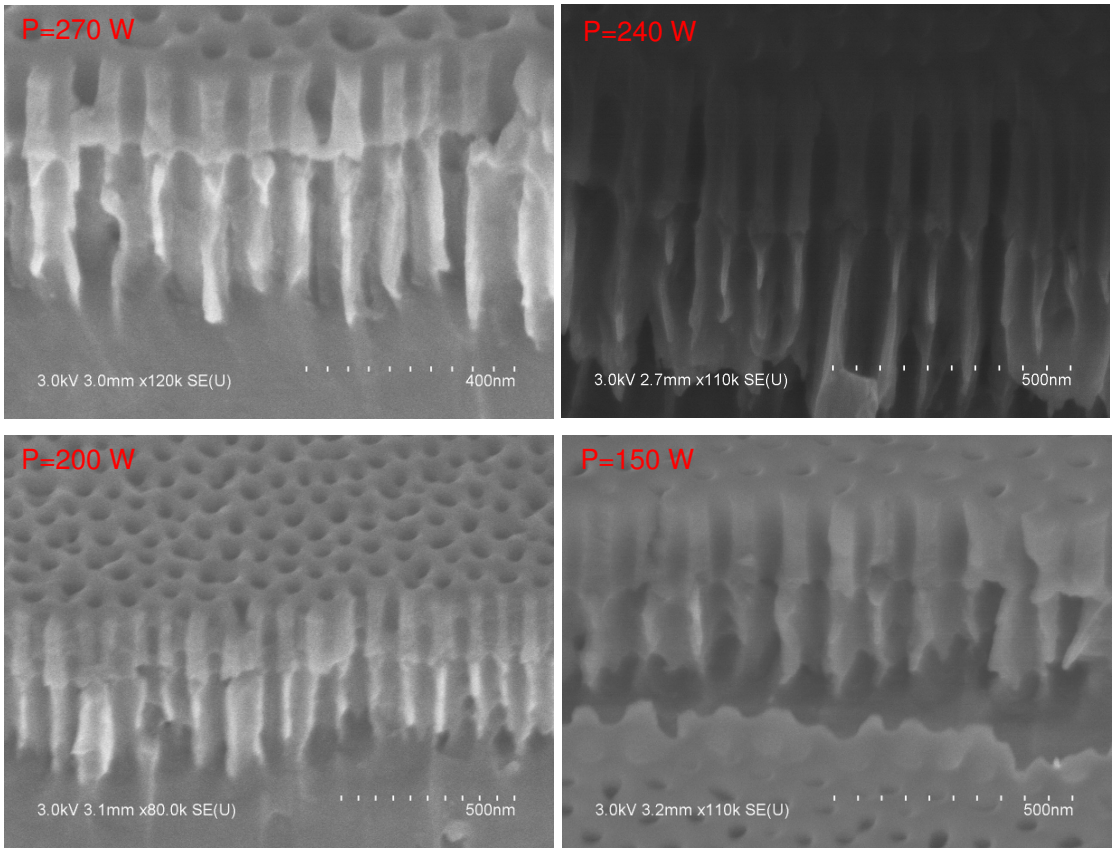


| ***Platen-power (W)*** | ***270*** | ***240*** | ***200*** | ***150*** |
|---|---|---|---|---|
| *Thickness Al-etch (nm)* | *280* | *280* | *250* | *200* |
| *Thickness PAA-etch (nm)* | *170* | *150* | *170* | *140* |
| *Refl. power (platen) (W)* | *11* | *8* | *5* | *2* |
| *Self-bias (V)* | *unstable* | *110* | *90* | *50* |

*Fig. IV.9: Influence of the platen-power P. All samples have been etched for 10 min under the optimized etching conditions by varying only P. In the table, the measured thicknesses of Al and $Al_2O_3$, respectively, after the 10 min etching duration are referred.*

The physical behaviour of the etching plasma and the etching species can be concluded by the reflected platen-power and the self-bias.

It can clearly be observed that the plasma becomes unstable with higher platen-powers. The platen-power of 270 W is the highest value that could be applied in the

mentioned configuration. Other tests have shown that a higher coil-power is needed to assure a stable plasma at higher platen-powers, but under these conditions, an anisotropic etching through the PAA mask has not been possible, since the ions are less directed perpendicular to the sample and thus, the etching becomes more isotropic.

The self-bias is increasing with increasing platen-power which demonstrates the higher energy of the bombarding ions. This influences, of course, the etching rate, which increases with increasing platen power. However, the etching rate of the PAA mask is rather not influenced by the platen-power. The slight variations of the etching rate seen in the table of Fig. IV.9, result of the measurement itself: this can be explained simply by the very slow etching rate of the PAA whose slight variation cannot be detected in the observed range.

The shape of the pores etched inside the Al is influenced by the platen-power, too. Although there is only a minor difference in the range from P=200-270 W, at lower platen power of 150 W it can already be seen that the pore walls become less straight and rough. For deeper etches, these low platen powers are not suited. The choice of a platen-power of 240 W finally has been done as this has been the highest power value for which constant stable plasma and thus etching conditions could be assured.

Influence of the coil power

The coil-power determines the density of the ions inside the plasma and thus has a strong influence on the etching rate and also the ion-ion collisions inside the plasma.

In Fig. IV.10, samples etched with different coil-powers are shown. The table in Fig. IV.10 summarizes the observed etching characteristics.

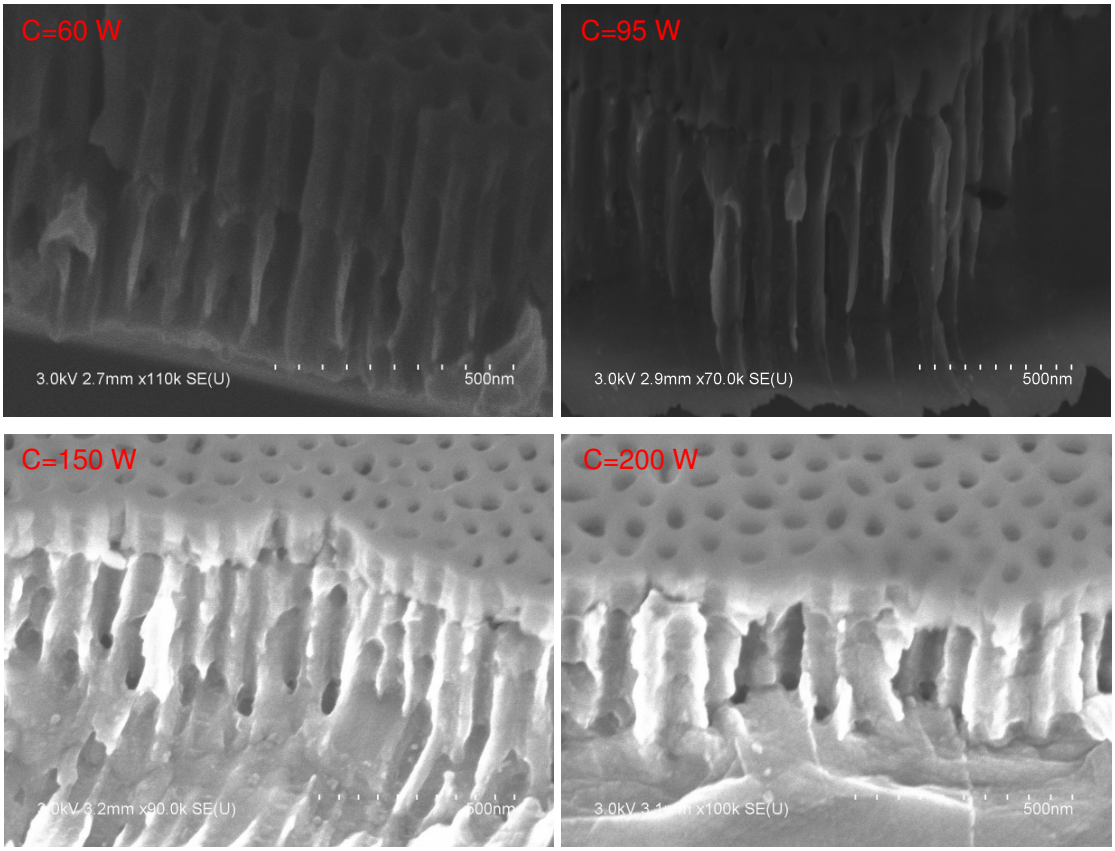


| ***Coil-power (W)*** | ***60*** | ***95*** | ***150*** | ***200*** |
|---|---|---|---|---|
| *Thickness Al-etch (nm)* | *180* | *280* | *280* | *250* |
| *Thickness PAA-etch (nm)* | *50* | *150* | *260* | *310* |
| *Refl. power (platen) (W)* | *8* | *8* | *8* | *8* |
| *Self-bias (V)* | *100* | *110* | *50* | *20* |

*Fig. IV.10: Influence of the coil-power C. All samples have been etched for 10 min under the optimized etching conditions by varying only C. In the table, the measured thicknesses of Al and $Al_2O_3$, respectively, after the 10 min etching time are referred.*

It can clearly be seen that the coil-power does not have an influence on the stability of the plasma in the investigated range, as the reflected power is low and constant for all different coil-powers. However, the self-bias decreases strongly with increasing coil-power. This can be explained by the higher density of the plasma: The shorter

mean-free path implicates a stronger interaction between the species in the plasma and thus enhances the charge exchange which reduces the potential of the sheath.
It is probably mostly due to the lower self-bias that in cases of higher coil-powers, the surface of the pore walls inside the Al become rough and the pores become less straight.
A very interesting effect is observed for the etching rates at the PAA surface and the one inside the Al: The etching rate of the PAA at the surface is strongly increasing with higher coil-power whereas the etching rate inside the Al only increases for low coil-powers and decreases again for higher coil-powers. This allows the following conclusion: At the surface, the etching rate simply increases with increasing plasma density. For the anisotropic etch inside the pores, the etching rate only increases with increasing coil-power as long as the etching is directional, i.e. highly anisotropic. As soon as the collisions between the ions in the dense plasma result in a less directional etch, the etching rate inside the pores decreases with increasing coil-power and the upcoming lateral etch leads to rough pore walls.
In respect of a high aspect ratio and the selectivity between the PAA mask and the Al-etch, low coil-powers are thus much more suited than higher ones. One should mention that in the used STS ICP system, under the applied etching conditions, we were limited to a lower limit of 60 W of the coil power. For lower coil-powers, the peak-to-peak voltage exceeded the limiting value of the system. The increase of the peak-to-peak voltage hereby is due to the fact that, by reducing the plasma density and keeping the platen-power constant, the voltage at the sample is automatically adjusted to higher values: The power being fixed and being the product of the current and the voltage at the electrode, the voltage is strongly increased if the current is decreased due to a lower density of charged species. In order to avoid the effect of a peak-to-peak voltage exceed, we therefore chose the coil-power of 95 W for the optimized condition.

Influence of the etching gas

The ratio between the two used etching gases, $Cl_2$ and Ar, has a strong impact on the etching behaviour inside the pores. In the etching process, Ar only serves as physically reactive gas, i.e. to remove matter by sputtering. $Cl_2$ in contrast reacts chemically and produces volatile etching products while reacting with Al. The addition of $Cl_2$ thus makes deeper etches possible and leads to cleaner pore walls and a

higher selectivity of the etching process. However, one has to keep in mind that pure $Cl_2$ leads to an isotropic etch. The influence of different $Cl_2$/Ar ratios can be observed in Fig. IV.11.

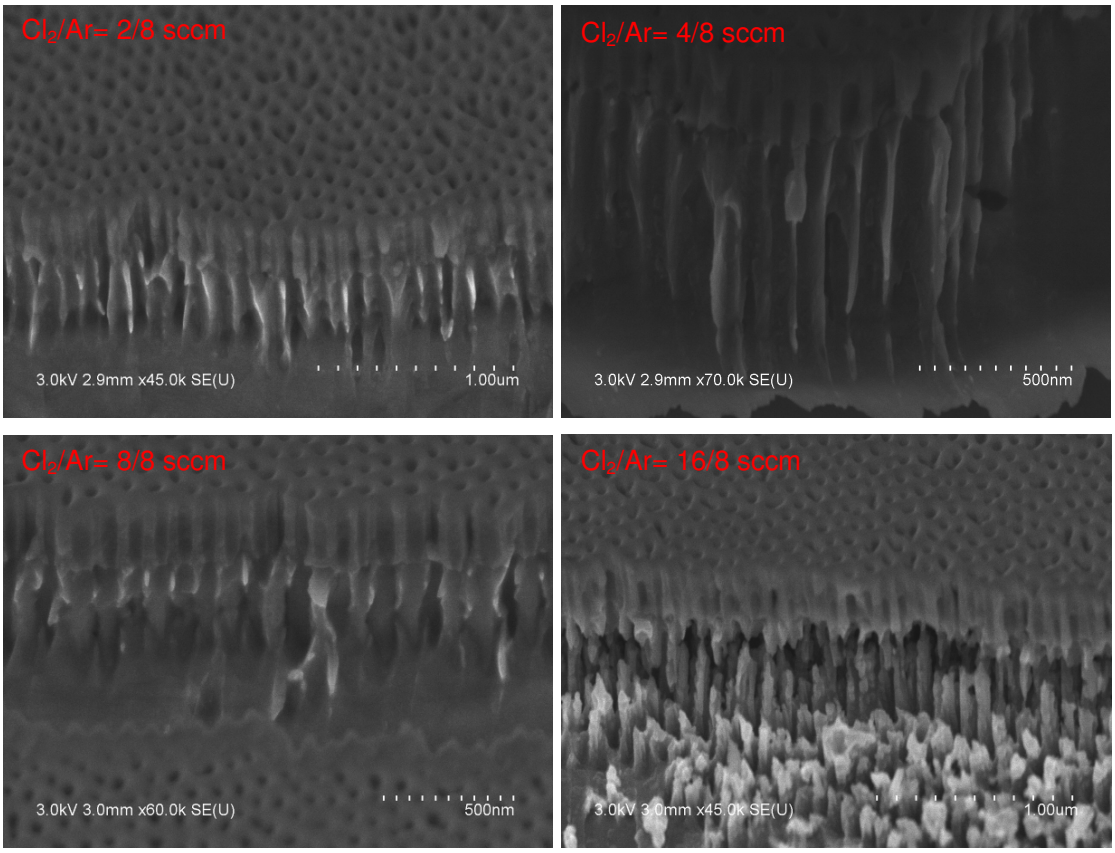


| ***Gas flow $Cl_2$/Ar (sccm)*** | ***2/8*** | ***4/8*** | ***8/8*** | ***16/8*** |
|---|---|---|---|---|
| *Thickness Al-etch (nm)* | *220* | *280* | *300* | *380* |
| *Thickness PAA-etch (nm)* | *150* | *150* | *150* | *180* |
| *Refl. power (platen) (W)* | *8* | *8* | *8* | *8* |
| *Self-bias (V)* | *120* | *110* | *130* | *120* |

*Fig. IV.11.: Influence of the different gas ratios. All samples have been etched for 10 min under the optimized etching conditions by varying only the gas ratio. In the table, the measured thicknesses of Al and $Al_2O_3$, respectively, after the 10 min etching time are referred.*

By varying only the gas ratio, neither the self-bias nor the reflected platen-power changes, which is evident, since the gas ratio does not have an influence on the electrical circuit inside the etching chamber.

As already mentioned, the selectivity of the etching becomes much better with higher amounts of $Cl_2$. But, with a higher percentage of $Cl_2$, the quality of the pores etched inside the Al drastically decreases, a real transfer of the porous structure does not anymore take place in the case of 16 sccm $Cl_2$.

For the optimized conditions, we have chosen the ratio of $Cl_2$/Ar=4/8 as in this case, no real degradation of the transfer of the porous structure can be observed but at the same time, a relatively good selectivity of the etching process is assured.

Conclusion

The effect of the variation of different etching parameters has been presented. The conclusion drawn for each specific parameter allowed us to determine the optimized etching conditions which have already been presented in paragraph IV.3.3.1.1. These etching conditions are also the basis for the multilayer etch, which will be described in the following paragraph.

### IV.3.3.2 The etching through the Al layer into a $SiO_2$ underlayer

In this paragraph, the use of a PAA for a multilayer etching will be discussed. The multilayer we have used correspond to the stacking described in Fig. IV.12.

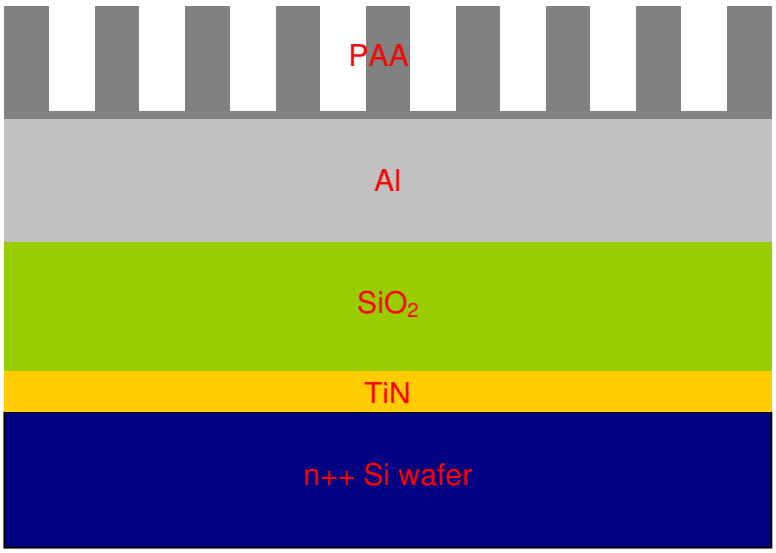


*Fig. IV.12.: Multilayer stacking with PAA mask on top.*

The goal of the etching trough this multilayer is the transfer of the porous structure in both the Al and the $SiO_2$ layer. We wanted to stop the etching on the TiN surface as this offers the very interesting stacking with a conducting layer that also serves as diffusion barrier at the pore bottom which is, by the $SiO_2$ layer, insulated from the Al layer which itself, by the PAA mask, is insolated from the surface. Any nanoelement defined in a pore could thus be contacted at three different places along the pore. One very interesting possible application of such structure is the vertical transistor. The basic idea of such transistor is presented in annexe A.

One big challenge is the fact that different etching chemistries are needed to etch $SiO_2$ and Al [126,127]. While, as already mentioned, the Al is chemically etched by $Cl_2$, $SiO_2$ is only very slowly etched by $Cl_2$ and much faster by fluor based gases. The use of a Cl-based etchant (for Al) leads to a partial reflection of the chloride species at the interface $SiO_2$-Al and thus to an accumulation of chloride species inside the pores which results in a lateral etch inside the Al layer and thus the destruction of the porous structure inside the Al layer. The change of the etching chemistry at the interface $SiO_2$-Al was therefore obligatory. Thus, in a first step, pores have been etched inside the Al that are open on the $SiO_2$, and then the etching

behaviour inside the $SiO_2$ itself could be studied by applying different reaction chemistries and thus different gases. These two investigations (the etching of pores that are open on the $SiO_2$ and the etching process inside the $SiO_2$) will be presented in the following chapters.

*IV.3.3.2.1 ICP Etching of open pores on $SiO_2$*

As already mentioned, the etching chemistry has to be changed at the interface $SiO_2$-Al in order to avoid a lateral etching inside the porous Al layer. This is evident, but the precision, with which the ICP etching process has to be stopped at this interface, is rather surprising. In Fig. IV.13, samples at different steps of the Al-etch are shown, applying the optimized etching conditions presented in paragraph IV.3.3.1.1.

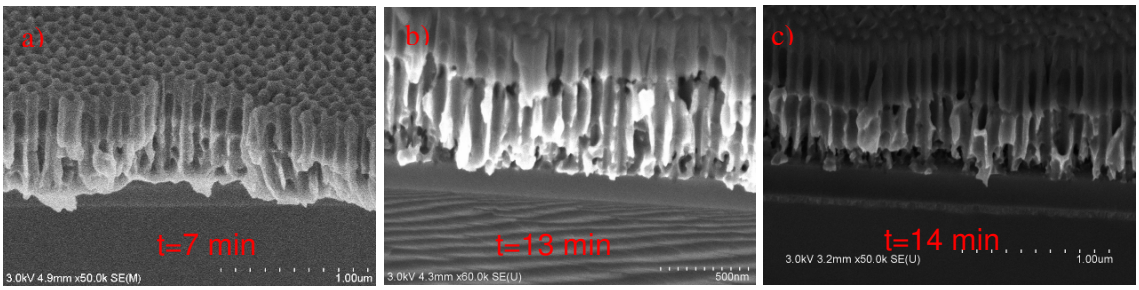


*Fig. IV.13: Sampes at different steps of the Al etch. The duration t of the Al etching increases from a) to c).*

In Fig. IV.13 a), the Al is not etched completely. The pores are straight inside the Al, but a subsequent fluoride based etching process cannot be applied as the fluoride does not react with Al and thus no etching will take place.

In Fig. IV.13 b), the pores are right opened on the $SiO_2$. This is the perfect sample for a subsequent $SiO_2$ etch.

In Fig. IV.13 c), the Al etch has been done 30 s after the opening of the pores. Clearly, a lateral etch inside the Al layer can be observed which weakens the porous structure.

Consequently, the Al etching has to be performed very carefully and the etching rate inside the Al has to be controlled precisely. Only if all the pores in the Al layer are open on the $SiO_2$, a really homogenous etching inside the $SiO_2$ layer can be realized. The homogeneity of the initial Al layer thickness is thus of major importance, as there is only very little time during which the ICP etching inside the Al layer can be

continued after having opened the first pore on the $SiO_2$ layer. Otherwise, the local destruction of the porous structure inside the Al takes place. In Fig. IV.14, two samples are shown after the etching inside the $SiO_2$ layer. The etching conditions of the $SiO_2$ have been identical (and correspond to the optimized conditions presented in the following paragraph IV.3.3.2.2), the only difference consists in the etching duration of the Al before the real etching process: in case of the sample in Fig. IV.14 b), this etching duration has been 20 s longer than in Fig. IV.14 a). But the pore density inside the $SiO_2$ varies drastically.

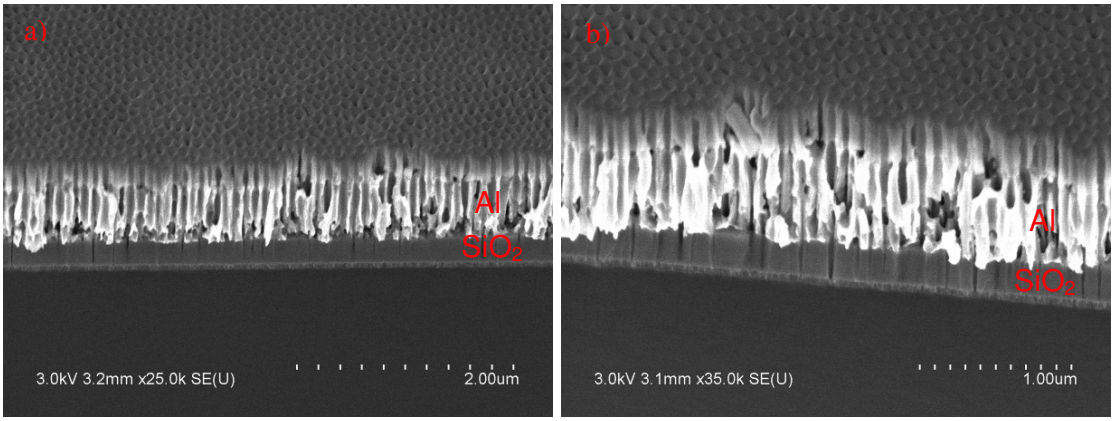


*Fig. IV.14: Etching inside the $SiO_2$ layer after two different etching durations inside Al.*

*IV.3.3.2.2 The etching process inside $SiO_2$*

It is well known that $SiO_2$ is a well suited material for an anisotropic etching process. As for the Al etching ICP process, we have used the lowest possible chamber pressure. This pressure has been fixed at 4 mTorr, but for a higher flow of etching gases than for the Al etching.

Different mixtures of $SF_6$, $CHF_3$ and $O_2$ have been used for the etching gases. Both $SF_6$ as $CHF_3$ react chemically and physically during the $SiO_2$-etch, and thus allow a vertical etch of $SiO_2$. However, the use of $CHF_3$ gives in general a higher aspect ratio and leads to more reliable etching results [129,130]. In this case, in addition to the etching effect, the carbon can form polymers at the pore walls and thus protect upper areas of the pores from a lateral etch by present fluoride species. The oxygen can remove these polymers and thus the equilibrium between these three gases is important for the anisotropic etching process. It should be mentioned that the commonly used Bosch process [131], in which $C_4F_8$ is used in a passivation step to protect the sidewalls before the following etching step, could not be applied for the

PAA mask of this work, as, during this passivation process, the pores would be completely clogged. Consequently, the use of $CHF_3$ has been the only possibility to protect the pore walls during the etching process.

Influence of the platen-power and the coil-power

Concerning the platen-power and the coil-power, the principles discussed in the previous pararaphs are still valid. However, one important difference between the Cl and the F etching consists in the much higher etching rate of $Al_2O_3$ in case of fluoride etching. Thus, especially the selectivity of the etching process is important for a suited etching process. In Fig. IV.15, the optimized etching conditions inside $SiO_2$ are shown. The etching conditions are the following:

Platen-power: 150 W

Coil-power: 300 W

Pressure: 4 mbar

Gas flows: $SF_6/CHF_3/O_2$: 5/100/2 sccm

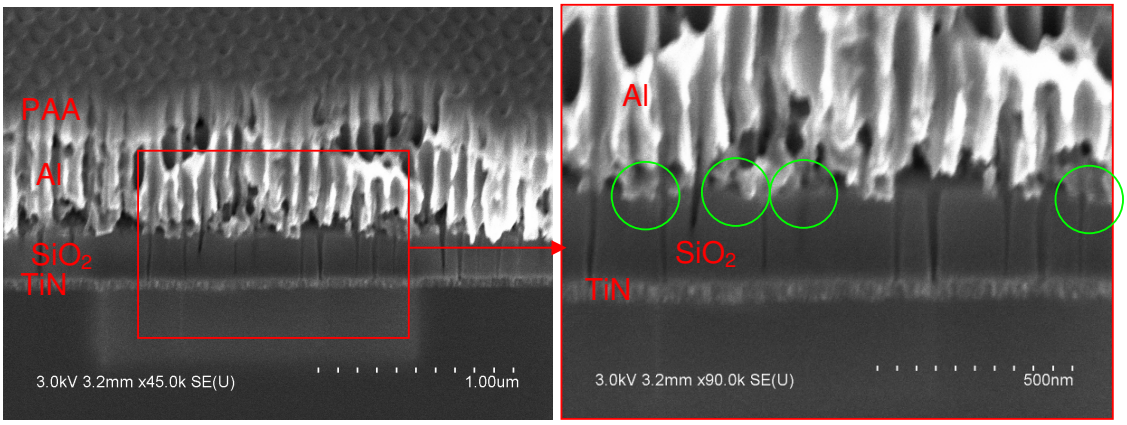


*Fig. IV.15: Optimized etching conditions inside $SiO_2$. On the right image there is a zoom from the marked area of the left one. In the right image, some areas at the pore bottoms with a remaining Al layer are marked.*

For the optimized etching conditions, a high density of straight pores inside the $SiO_2$ layer can be obtained as shown in Fig. IV.15. However, still the porous structure has not been transferred completely inside the $SiO_2$. This is mostly due to the non-homogeneity of the Al layer. The blocking Al-layer right at the bottom of the pores is marked in Fig. IV.15. This problem might be solved in the future as a new e-beam evaporation system will be available for our group which is supposed to produce a perfect homogeneity of deposition thicknesses.

In Fig. IV.16, the influence of the platen- and the coil-power on the etching conditions is shown by some selected examples. For these samples, the optimized etching conditions have been applied by only varying the platen- and the coil-power. All samples have been cleaved from the same initial sample after the anodization steps and the Al etch.

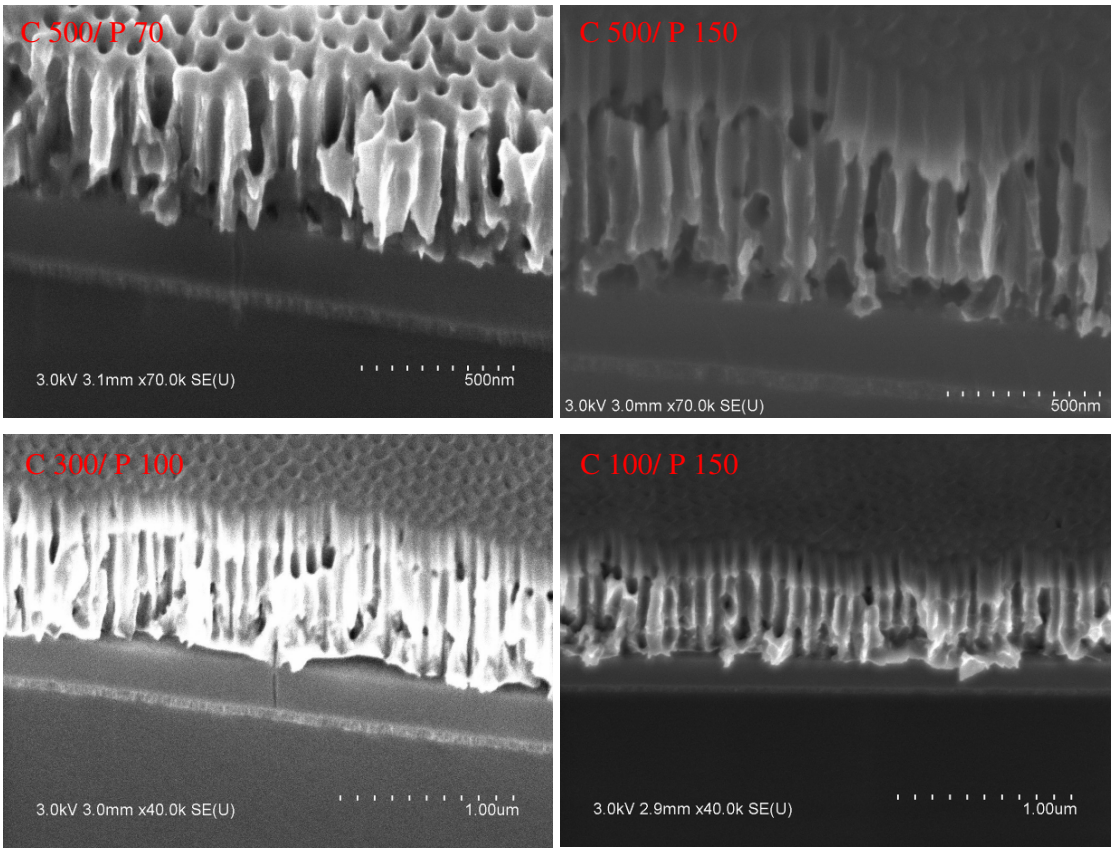


| *C/P (W)* | *500/70* | *500/150* | *300/100* | *300/150* | *100/150* |
|---|---|---|---|---|---|
| *thickness PAA-etch (nm)* | *200* | *>400* | *180* | *200* | *150* |

*Fig. IV.16: Influence of coil-power C and platen-power P on the $SiO_2$-etching process. The etching process has been performed for 10 min under optimized conditions by varying only C and P.*

In Fig. IV. 16, the following tendencies are shown:

A very high coil power combined with a very low platen power (C500/P70) does not lead to any etched pores inside the $SiO_2$, but leads to slight lateral etch of the pore walls inside the Al. Obviously, there is a high density of the plasma and the low platen power is not able to direct the species inside the plasma well perpendicular to

the sample, since too many collisions between the ions take place. However, at the same time, the PAA mask surface is etched. Therefore, we cannot use these etching conditions for our purpose.

If the very high coil power is combined with a higher platen power (C500/P150), the etching effect becomes very strong and the PAA mask itself is etched fast. At the same time, there is a visible etching process inside the $SiO_2$ due to the stronger directional movement of the ions, but the etching process is not enough selective between the PAA mask- and the $SiO_2$-etch. Thus, very high coil powers do not seem to be suited for our purpose, combined with any platen power.

If the coil power is reduced to only 300 W, an etching inside the $SiO_2$ can be observed (C300/P100) with sufficient selectivity between the etching of the PAA mask and of the $SiO_2$. However, compared with the optimized etching conditions (C300/P150), the etching process inside the $SiO_2$ works much better with a platen power of 150 W and without loosing the selectivity (see images in Fig. IV.15).

In case of further reduction of the coil power (C100/P150), there is no visible etching inside the $SiO_2$ anymore, but only a slow etch of the PAA mask.

Thus, in terms of the selectivity between the etching of the PAA mask and the etching of the $SiO_2$ and in respect to the uniformity of the etching process, the optimized etching values have been chosen (C300/P150, Fig. IV.15).

Influence of the etching gas

As we have used three different gases, the gas ratio can be varied in a wide range. In the following, only an extract of the entire series that has been studied will be shown, that gives an idea about the influence of the different gas ratios. In Fig. IV.17, the influence of different gas flows is shown. These samples have been prepared under the optimized power/pressure conditions by varying the different gas flows. All samples have been cleaved from the same initial sample after the anodization steps and the Al etch and therefore show the same Al-$SiO_2$ interface.

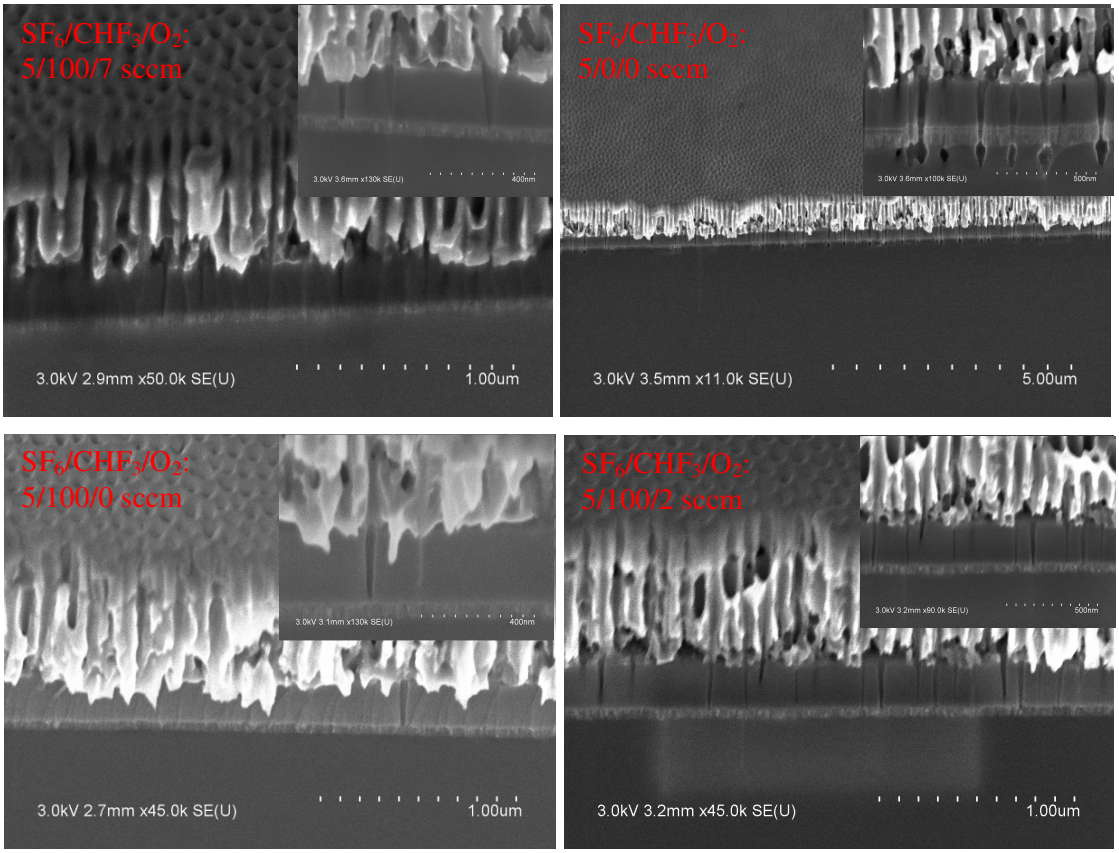


*Fig. IV.17: Influence of the gas flows on the etching inside $SiO_2$. The samples have been etched for 10 min under the optimized conditions by only varying the gas flows.*

In the case of pure $SF_6$ etching, the pores in $SiO_2$ are of a slightly conic shape, which is probably due to the lack of protection of the pore walls by polymers formed of carbon species inside the $CHF_3$. The most significant change concerning the pure $SF_6$ etching anyway is that the etching process does not stop on the TiN. We wanted to avoid this effect in order to have a well defined pore structure in the multilayer system that ends on a conducting barrier layer, i.e. the TiN.

With the addition of $CHF_3$, the pores are straighter, but the density of the pores decreases. Probably, the etching process is too much inhibited by polymer deposition, which is especially important if the Al etch has opened only a very small aperture at the bottom of the pores inside the Al. The addition of $O_2$, that etches the deposited polymers, thus was necessary.

However, for high $O_2$ flows, the pores again are of a conic shape. The finally found optimized etching parameters are chosen in order to achieve a straight porous structure with a high pore density inside the $SiO_2$.

Conclusion

The etching inside the PAA-Al-SiO2-TiN multilayer with TiN as stopping layer has been investigated. We have shown that the etching process inside the Al layer can be perfectly controlled, which leads to a perfect transfer of the porous structure inside the Al layer.

For the transfer of the porous structure inside the $SiO_2$ layer under the Al layer, good results could be achieved after a thorough optimization process. A porous structure with straight pores and a high pore density is obtained. However, the transfer inside the $SiO_2$ layer could not be performed with the same precision like into the Al layer, not all pores of the porous structure inside the Al layer could be transferred into the $SiO_2$. This is mainly due to the inhomogeneity of the initial thickness of the Al layer deposited on the top of the structure. This problem could be solved by using a high precision e-beam evaporator which our group will have access to, in the future.

However, to overcome this problem, we have tried another approach. This approach consisted in replacing the Al layer of the structure by a deposited n-doped polycrystalline silicon (poly-Si) layer. In this case, the etching chemistry is the same for both the n-doped poly-Si etch and the $SiO_2$ etch which allows one to etch both layers in one step. This approach is the subject of the following paragraph.

### IV.3.4 PAA mask on n-doped polycrystalline-Si for multilayer etching

For the etching of the n-doped polycrystalline Si, the PAA mask has been prepared with open pores on the n-doped poly-Si as described in paragraph I.3.5.1. Such sample before etching is shown In Fig. IV.18.

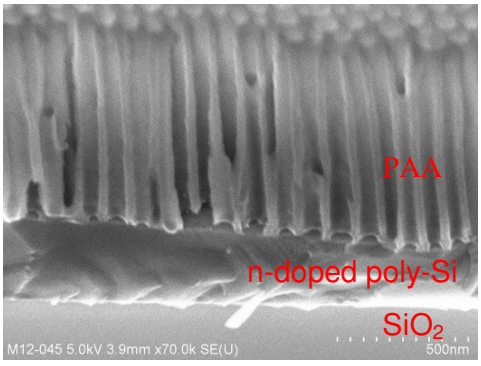


*Fig. IV.18: Multilayer sample before etching.*

In principle, an etching process similar to the $SiO_2$ etching ICP process described in the previous chapter has to be applied, whereas the platen- and coil-power should be lower for the n-doped poly-Si etch and again fluoride gases should be used. These power values have been varied in a wide range, but for all applied parameters we have been faced with the same problem: the adhesion between the n-doped poly-Si and the PAA mask is very weak, since the Si is etched from the interface Si-PAA and therefore, the connecting surface between the PAA and Si is easily underetched or destroyed by lateral etching. In Fig. IV.19, the sample after different etching durations is shown.

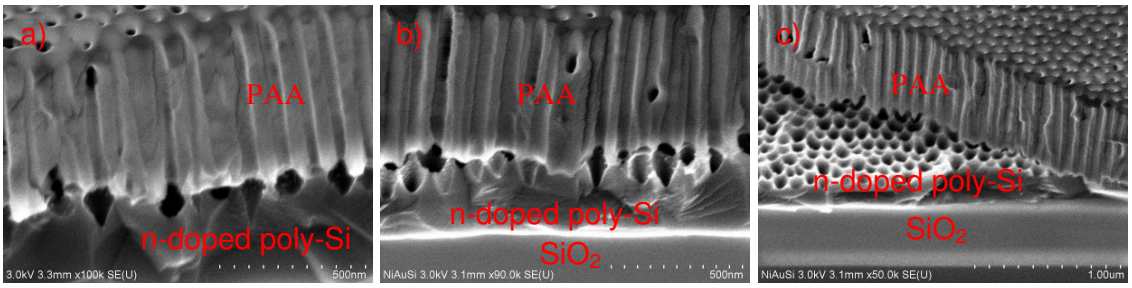


*Fig. IV.19: Samples etched for 7 min (a), 10 min (b) and 12 min (c) are shown. The etching conditions have been: $SF_6/CHF_3/O_2$=5/100/2 sccm, C=50 W, P=90 W.*

It is clearly seen that the PAA membrane looses the contact to the n-doped poly-Si underlayer with increasing etching time. If the etching time is even more increased, this intermediate n-doped poly-Si layer is completely etched and the etching process continues into the $SiO_2$ layer (Fig. IV.20 a). In Fig. IV.20 b), the alumina membrane has been removed and the vertical etch inside the $SiO_2$ can be observed. However, this etching process is clearly not suited for the desired application as the intermediate n-doped poly-Si is completely destroyed during the vertical etching process into $SiO_2$.

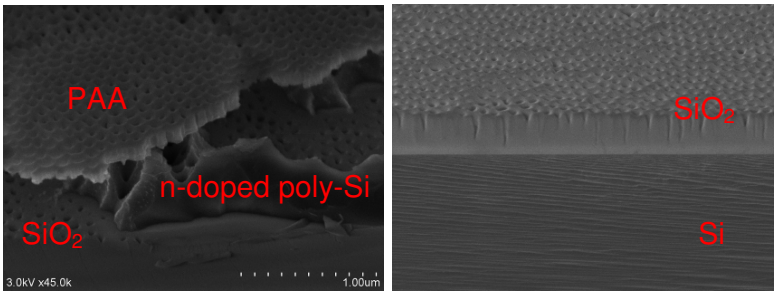


*Fig. IV.20: Prolonged etching into the n-doped poly-Si and $SiO_2$ layer.*

## IV.4 Conclusion

For the first time, we have realized a multilayer etching process by using PAA masks. This includes the perfect control of the anisotropic etching process into the Al layer under the PAA mask with a perfect transfer of the porous structure of the PAA in this layer, as well as the subsequent etching process into the $SiO_2$ layer. However, although a high density porous multilayer structure has been realized, not all pores of the PAA structure have been transferred inside the $SiO_2$ layer. This is probably due to the inhomogeneity of the deposited Al thickness, which, in the future, will be solved by the application of a high performance evaporation system.

In another approach, we tried to replace the Al layer in the above mentioned stacking by a n-doped poly-Si layer. In this case, no satisfying results could be obtained as the lateral etch inside the the n-doped poly-Si layer has been too important during the etching process, especially for the long etching durations that have been necessary for the $SiO_2$ etch.

The described results offer the possibility for the realization of reliable vertical porous multilayer structures in respect of applications for the contacting of nanoelements like SiNWs and CNTs and for the realization of devices based on those nanoelements.

One possible device that has become practicable with the presented results is the vertical transistor whose concept is presented in annexe A.

# Conclusion and Outlook

In this work, we studied the anodization process for the fabrication of PAA and the feasibility of different further applications of PAA, like the electrodeposition and CNT growth inside the PAA and the use of PAA as etching mask. Our first goal hereby was to obtain a good understanding of the anodization process and to become aware of the crucial experimental parameters during the anodization in order to be able to fabricate PAA membranes in a reliable, reproducible way.

Concerning the formation rate of PAA, which is important for the determination of the PAA thickness after the anodization, we have pointed out the influence of the experimental conditions such as the temperature and the time and concentration of the anodization acid. In particular, we have found that the dipping time of the aluminium inside the acid (before the 'real' anodization) has a strong influence on the formation rate of PAA. In consideration of the crucial anodization parameters we have determined, we have been able to fabricate PAA under completely reliable formation rates.

Concerning the barrier layer at the pore bottom, we have developed a unique technique to control both the thickness of the barrier layer and the uniformity of said thickness over the sample. This is in particular interesting for further applications of PAA, as shown for further electrodeposition or CNT growth based on PAA.

In respect to the fabrication of very small pores, we found that highly concentrated sulfuric acid is adapted the best for an anodization acid. By applying of very low voltages (< 5 V) on Al in said acid, we have been able to realize PAA membranes with pore diameters of about 4 nm, the lowest diameter reported for PAA so far.

On the prefabricated PAA membranes, we have been able to adapt an electrodeposition step by which Ni-particles can be deposited in controllable density inside the pores and by precisely controlling the amount of deposited Ni.

This allowed us to study the CNT growth inside PAA and on surfaces patterned by PAA with pore diameters of about 40 nm. During this study, we have investigated the growth conditions both for CVD and for PECVD growth on the respective samples. By this way, we were able to realize a high density of CNT inside a PAA membrane and in particular, we were able to realize vertical aligned CNTs whose density is adjustable by the pretreatment of the PAA before the

electrodeposition and the electrodeposition itself. This allowed us to measure the field emission of respectively fabricated CNT arrangements.

Moreover, we investigated the use of PAA as etching mask. In this study, we developed a good understanding of the etching process using PAA as etching mask and realized porous multilayer structures by transferring the ordered pores of a PAA membrane into the following underlayers, which has not yet been realized so far.

The results obtained in this work contribute to a good understanding and to an increased reliability of the fabrication process of PAA. The realization of further processing, like the electrodeposition, the CNT growth and the use of PAA as etching mask, show new possibilities for future applications. However, the results in this work also make evident that still research is necessary and promising in the field of PAA.

We demonstrated the feasibility of the fabrication of very small pore diameter PAA (4nm), but did not investigate the formation rate, electrodeposition, CNT-growth and etching behaviour on these extreme PAA structures. The investigation itself of those small diameter and high density PAA structures could be very interesting for several nanoapplications, e.g. interconectors. This is a real challenge.

The porous multilayer structure as well could be the basis for further research on nanodevices. However, still the problem of the uniformity of the etched pores must be solved, for which a very uniform deposition of the multilayers will be necessary, combined with a perfectly calibrated etching rate. In addition, physical properties of such multilayers like the rigidity and leakage current through damages caused by the etching process must be analyzed. Once such uniform multilayer is realized, the vertical transistor is one promising application, which implies to solve device-specific problems, like the contacting of the multilayers and the nanoelement inside the pores.

The field emission given by the randomly dispersed vertical CNT with adjustable CNT density is very interesting, as it is a cost-efficient method. The field emission current of about 1 mA we obtained must be improved for further applications. The reasons for this low emission current have to be analyzed in detail, namely the influence of the poisoning of the catalyst during the growth. In this respect, still a detailed study of the growth process on such samples and of the catalyst treatment before the growth will be necessary.

# ANNEXE A: The vertical transistor

The presented concept for the vertical transistor shows a device based on nanoelements like semiconducting CNTs (Fig. A1) or semiconductor nanowires. The intended transitor structure offers a surroundgate transistor with vertical aligned CNTs. This is the most favourable geometry as the electric field is symmetrical and influences the CNTs equally in their whole diameter. Besides, the vertical structure offers the possibility of a very close stacking of parallel contacted CNTs.

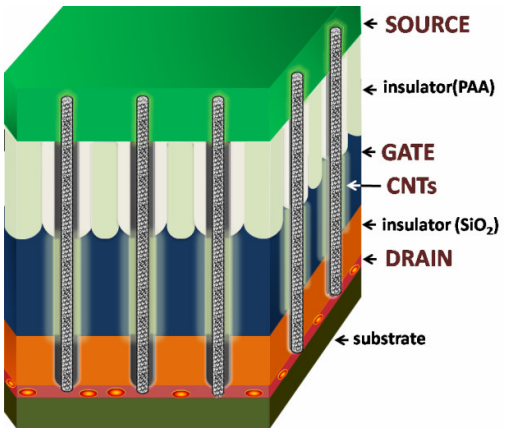


*Fig. A1: The concept for the vertical transistor.*

The idea for the vertical transistor is based on a porous multilayer structure in which a conducting layer forms the pore bottom, followed by a first insolating porous layer, again by a porous conductive layer and one more insolating layer. On the conductive pore bottom, growth catalyst can either be deposited by electrodepositon or formed by annealing a thin layer of catalyst material deposited on the conducting layer during the stacking of the layers of the multilayer structure. The porous multilayer can then be loaded in a CVD growth system and growth of, e.g., CNTs can take place. These CNTs are thus in electrical contact with the conducting underlayer. If an electrode is evaporated on CNTs that have reached the surface during growth, these CNTs can be contacted by this top electrode and the conductive bottom layer. Taking into account the conductive layer in the centre of the multilayer structure, the CNTs can be contacted at the top, the bottom and in the centre area.

In the multilayer structure discussed in chapter IV.3.3, the conductive layer in the centre of the multilayer structure consists of Al. Al is known as a very fast oxidizing material. Thus, if the porous multilayer structure is annealed under oxidizing atmosphere after the growth and before the deposition of the upper electrode, a metal oxide is at the interior of the pore inside the Al layer which enables this layer to work like a gate for the CNTs inside the pores. Besides, as the volume expands during the formation of $Al_2O_3$ from Al, the oxidized pore walls will enclose the CNTs inside the pore which will lead to a good contact.

# References


[1] C.R. Martin, *Chem. Mater.* **8**, 1739, 1996.
[2] K. Nielsch, F. Müller, A. P. Li, U. Gösele, *Adv. Mat.* **12**, 582, 2000.
[3] J. Choi, G. Sauer, K. Nielsch, R. B. Wehrspohn, U. Gösele, *Chem. Mat.* **14**, 776, 2003.
[4] B. Wolfrum, Y. Mourzina, D. Mayer, D. Schwaab, A. Offenhäusser, *Small* **2**, 1256, 2006.
[5] T. Shimizu, T. Xie, J. Nishikawa, S. Shingubara, S. Senz, U. Gösele, *Adv. Mat.* **19**, 917, 2007.
[6] S. Matéfli-Tempfli, M. Matéfli-Tempfli, A. Vlad, V. Antohe, L. Piraux, *J. Mat. Sci: Mater Electron* **20**, 249, 2009.
[7] L. Li, S. Pan, X. Dou, Y. Zhu, X. Huang, Y. Yang, G. Li, L. Zhang, *J. Phys. Chem.* **111**, 7288, 2007.
[8] M. V. Kamalakar, A. K. Raychaudhuri, *Phys. Rev. B* **79**, 205417, 2009.
[9] X. H. Huang, G. H. Li, X. C. Dou, L. Li, *J. Appl. Phys.* **105**, 084306, 2009.
[10] A. Vlad, M. Matéfi-Tempfli, V. A. Antohe, S. Faniel, N. Reckinger, B. Olbrechts, A. Crahay, V. Bayot, L. Piraux, S. Melinte, S. Matéfi-Tempfli, *Small* **4**, 557, 2008.
[11] T. Iwasaki, T. Motoi, T. Den, *Appl. Phys. Lett.* **75**, 2044, 1999.
[12] T. E. Bogart, S. Dey, K.-K. Lew, S. E. Mohney, J. M. Redwing, *Adv. Mat.* **17**, 114, 2005.
[13] M. R. Maschmann, A. D. Franklin, P. B. Amama, D. N. Zakharov, E. A. Stach, T. D. Sands, T. S. Fisher, *Nanotechnology* **17**, 3925, 2006.
[14] M. R. Maschmann, A. D. Franklin, A. Scott, D. B. Janes, T. D. Sands, T. S. Fisher, *NanoLett.* **6**, 2712, 2006.
[15] A. D. Franklin, R. A. Sayer, T. D. Sands, D. B. Janes, T. S. Fisher, *IEEE Trans. Nanotech.* **8**, 1536, 2009.
[16] J. S. Lee, G. H. Gu, H. Kim, K. S. Jeong, J. Bae, J. S. Suh, *Chem. Mat.* **13**, 2387, 2001.
[17] H. Y. Jung, S. M. Jung, J. R. Kim, J. S. Suh, *Appl. Phys. Lett.* **90**, 153114, 2007.
[18] J.-F. Dayen, A. Rumyantseva, C. Ciornei, T. L. Wade, J.-E. Wegrowe, D. Pribat, C. Cojocaru, *Appl. Phys. Lett.* **90**, 173110, 2007.
[19] S. M. Eichfeld, T.-T- Ho, C. M. Eichfeld, A. Cranmer, S. E. Mohney, T. S. Mayer, J. M. Redwing, *Nanotechnology* **18**, 315201, 2007.
[20] G. Cheng, M. Moskovits, *Adv. Mat.* **14**, 1567, 2002.
[21] J. H. Choi, T. H. Kim, J. Seo, Y. Ku, M. S. Suh, *Appl. Phys. Lett.* **85**, 3235, 2004.
[22] A. Tormann, N. Teuscher, M. Pfannmöller, U. Rothe, A. Heilmann, *Small* **3**, 1032, 2007.
[23] J. P. O'Sullivan, G. C. Wood, *Roy. Soc. Lond.* A. **317**, 511, 1970.
[24] H. Masuda, K. Fukuda, *Science* **268**, 1466, 1995.
[25] A. P. Li, F. Müller, A. Birner, K. Nielsch, U. Gösele, *J. Appl. Phys.* **84**, 6023, 1998.
[26] F. Zhang, X. Liu, C. Pan, J. Zhu, *Nanotechnology* **18**, 345302, 2007.
[27] S. M. Moon, S. I. Pyun, *J. Electrochim. Acta.* **43**, 3117, 1998.
[28] T. P. Hoar, N. F. Mott, *J. Phys. Chem. Solids.* **9**, 97, 1959.
[29] K. Shimizu, K. Kobayashi, G. E. Thompson, G. C. Wood, *Phil.Mag. B* **64**, 345, 1991.
[30] V. P. Parkhutik, V. I. Shershulsky, *J. Phys. D: Appl Phys.* **25**, 1258, 1992.
[31] S. K. Thamida, H. C. Chang, *chaos* **12**, 240, 2002.
[32] K. Nielsch, J. Choi, K. Schwirn, R. B. Wehrspohn, U. Gösele, *Nano Lett* **2**, 677, 2002.

[33] S. Ono, M. Saito, M. Ishiguro, H. Asoh, *J. Electrochem. Soc*. **151**, B473, 2004.
[34] S. Ono, M. Saito, H. Asoh, *Electrochimica Acta* **51**, 82,72005.
[35] M. A. Kashi, A. Ramazani, *J. Phys. D: Appl. Phys.* **38**, 2396, 2005.
[36] L. Ba, W. S. Li, *J. Phys. D: Appl. Phys.* **33**, 2427, 2000.
[37] T.-Y. Kim, S.-H. Jeong, *Korean J. Chem. Eng.* **25**, 609, 2008.
[38] J. Oh, C. V. Thompson, *Adv. Mat.* **20**, 1368, 2002.
[39] I. Vrublevsky, V. Parkoun, J. Schreckenbach, W. A. Goedel, *Appl. Surf. Sc.* **252**, 5100, 2006.
[40] M. Tian, S. Xu, J. Wang, N. Kumar, E. Wertz, Q. Li, P. M. Campbell, M. H. W. Chan, T. E. Mallouk, *Nano Lett.* **5**, 697, 2005.
[41] J. Li, C. Papadopoulos, J. Xu, *Nature* **402**, 253, 1999.
[42] G.Meng, Y. J. Jung, A. Cao, R. Vajtai, P. M. Ajayan, *PNAS* **102**, 7074, 2005.
[43] W. Cheng, M. Steinhart, U. Gösele, R. B. Wehrspohn, *J. Mat. Chem.* **17**, 3493, 2007.
[44] H. Masuda, M. Yotsuya, M. Ishida, *Jpn. J. Appl. Phys.* **37**, L1090, 1998.
[45] D. Routkevitch, A. A. Tager, J. Haruyama, D. Almawlawi, M. Moskovits, J. M. Xu, *IEEE Trans. Electr. Devices* **147**, 1646, 1996.
[46] L. Li, s. Pan, X. Dou, Y. Zhu, X. Huang, Y. Yang, G. Li, L. Zhang, *J. Phys. Chem. C* **111**, 7288, 2007.
[47] T. E. Bogart, S. Dey, K.-K. Lew, S. E. Mohney, J. M. Redwing, *Adv. Mat.* **17**, 114, 2005.
[48] T. Iwasaki, T. Motoi, T. Den, *Appl. Phys. Lett.* **75**, 2044, 1999.
[49] G. P. Sklar, K. Paramguru, M. Misra, J. C. LaCombe, *Nanotechnology* **16**, 1265, 2005.
[50] A. Saedi, M. Ghorbani, *Mat. Chem. a. Phys.* **91**, 417, 2005.
[51] C. Jia, B. Zhang, W. Liu, C. Jin, L. Yao, W. Cai, X. Li, *J. Cryst. Growth* **285**, 527, 2005.
[52] G. J. Strijkers, J. H. J. Dalderop, M. A. A. Broeksteeg, H. J. M. Swagten, W. J. M. de Jonge, *J. Appl. Phys.* **86**, 5141, 1999.
[53] M. L. Tian, J. U. Wang, J. Kurtz, T. E. Mallouk, M. H. W. Chan, *Nano Lett.* **3**, 919, 2003.
[54] X. Y, Zhang, L. D. Zhang, Y. Dei, L. X. Zhao, Y. Q. Mao, *J. Mat. Chem.* **11**, 1732, 2001.
[55] V. Caboni, *Italian Patent* 339232, 1937.
[56] D. AlMawlawi, N. Coombs, M. J. Moscovits, *J. Appl. Phys.* **70**, 4421, 1991.
[57] M. Zheng, L. Menon, H. Zeng, Y. Liu, S. Bandyopadhyay, R. D. Kirby, D. J. Sellmyer, *Phys. Rev. B – Cond. Mat.* **62**, 12282, 2000.
[58] A. J. Yin, J. Li, W. Jian, A. J. Bennett, J. M. Xu, *Appl. Phys. Lett.* **79**, 1039, 2001.
[59] N. J. Gerein, J. A. Haber, *J. Phys. Chem. B* **109**, 17372, 2005.
[60] K. Nielsch, F. Müller, A.-P. Li, U. Gösele, *Adv. Mat.* **12**, 582, 200.
[61] G. Sauer, G. Brehm, S. Schneider, K. Nielsch, R. B. Wehrspohn, J. Choi, H. Hofmeister, U. Gösele, *J. Appl. Phys.* **91**, 3243, 2002.
[62] W. Cheng , M. Steinhart , U. Gösele , R. B. Wehrspohn, *J. Mat. Chem.* **17,** 3493,2007.
[63] Y.-G. Guo, L.J. Wan, C.-F. Zhu, D.-L.-Yang, D.-M.-Chen, C.-L. Bai, *Chem. Mat.* **15**, 664, 2003.
[64] K. Kim, M. Kim, S. M. Cho, *Mat. Chem. and Phys.* **96**, 278, 2006.
[65] A. Saedi, M. Ghorbani, *Mat. Chem. and Phys.* **91**, 417, 2005.
[66] X. H. Huang, G. H. Li, X. C. Dou, L. Li, *J. Appl. Phys.* **105**, 84306, 2009.
[67] G. Sharma, M. V. Pishko, C. A. Grimes, *J. Mat. Sci.* **42**, 4738, 2007.

[68] S. Ijima, *Nature* **354**, 56, 1991.
[69] S. Ijima, T. Ichihasi, *Nature* **363**, 603, 1993.
[70] M. S. Dresselhaus, G. Dresselhaus, R. Saito, *Phys. Rev.* B **45**, 6234, 1992
[71] J. W. Mintmire, B. I. Dunlap, C. T. White, *Phys. Rev. Lett.* **68**, 631, 1992.
[72] J. W. G. Wildöer, L.C. Venema, A. G. Rinwler, R. E. Smalley, C. Dekker, *Nature* **391**, 59, 1998.
[73] T. W. Odom, J. L. Huang, P. Kimm, C. M. Lieber, *Nature* **391**, 62, 1998.
[74] R. H. Baughman, A. A. Zakhidov, W. A. de Heer, *Science* **297**, 787, 2002.
[75] H. J. Jeong, L. Eude, M. Gowtham, B. Marquardt, S. H. Lim, S. Enouz, C. S. Cojocaru, K. A. Park, Y. H. Lee, D. Pribat, *Nano* **3**, 3, 145, 2008.
[76] C. S. Cojocaru, D. Y. Kim, D. Pribat, J. E. Bourée, *Thin Solid Films* 501, 1-2, 227, 2006.
[77] C. H. Olk, J. P. Heremans, *J. Mat. Res.* **9**, 259, 1994.
[78] R. Saito, M. Fujita, G. Dresselhaus, M. S. Dresselhaus, *Phys. Rev.B.,* **46**,1804(1992).
[79] L. Chico, V. H. Crespi, L. X. Benedict, S. G. Louie, M. L. Cohen, *Phys. Rev. Lett.* **76**, 971, 1996.
[80] X. Blase, L. X. Benedict, E. L. Shirley, S. G. Louie, *Phys. Rev. Lett.* **72**, 1878, 1994.
[81] T. W. Ebbesen, P. M. Ajayan, *Nature* **358**, 220, 1992.
[82] A. Thess, R. Lee, P. Nikolaev, H. J. Dai, P. Petit, J. Robert, C. H. Xu, Y. H. Lee, S. G. Kim, A. G. Rinzler, D. T. Colbert, G. E. Scuseria, D. Tomanek, J. E. Fischer, R. E. Smalley, *Science* **273**, 483, 1996.
[83] C. Journet, W. K. Maser, P. Bernier, A. Loiseau, M. L. Delachapelle, S. Lefrant, P. Deniard, R. Lee, J. E. Fischer, *Nature* **388**, 756, 1997.
[84] J. Kong, H. Soh, A. Cassell, C. F. Quate, H. Dai, *Nature* **395**, 878, 1998.
[85] Z. F. Ren, Z. P. Huang, J. W. Xu, J. H. Wang, *Science* **282**, 1105, 1998.
[86] R. S. Wagner, W. C. Ellis, *Appl. Phys. Lett.*, **4**, 89, 1964.
[87] Y. Saito, *Carbon*, **33**, 979,1995.
[88] C. L. Cheung, A. Kurtz, H. Park, C. M. Lieber, *J. Phys. Chem.* B., **106**, 2429, 2002.
[89] Y. Li, W. Kim, Y. Zhang, M. Rolandi, D. Wang, H. Dai, *J. Phys. Chem.* B., **105**, 11424, 2001.
[90] Z. F. Ren, Z. P. Huang, J. W. Xu, J. H. Wang, P. Bush, M. P. Siegal, P. N. Provencio, *Science* **282**, 5391, 1105, 1998.
[91] A. Bachtold, P. Hardley, T. Nakanishi, C. Dekker, *Science* **294**, 1317, 2001.
[92] P. Avouris, Z. H. Chen, V. Perebeinos, *Nature Nanotech.* **2**, 605, 2007.
[93] M. Terrones, N. Grobert, J. Olivares, J. P. Zhang, H. Terrones, K. Kordatos, W. K. Hsu, J. P. Hare, P. D. Townsend, K. Prassides, A. K. Cheetham, H. W. Kroto, D. R. Walton, *Nature* **388**, 52,1997.
[94] M. Su, Y. Li, B. Maynor, A. Buldum, J. P. Lu, J. Liu, *J. Phys. Chem. B.,* **104**, 6505, 2000.
[95] S. J. Kang, C. Kocabas, T. Ozel, M. Shim, N. Pimparkar, M. A. Alam, S. V. Rotkin, J. A. Rogers, *Nature Nanotech*, **2**, 230, 2007.
[96] J. S. Suh, J. S. Lee, *Appl. Phys. Lett.* **75**, 2047, 1999.
[97] H. Jung, J. Kim, J. Hahn, J. S. Suh, *Chem. Phys. Lett* **402**, 535, 2005.
[98] M. R. Maschmann, A. D. Franklin, T. D. Sands, T. S. Fisher, *Carbon* **45**, 2290, 2007.
[99] H. Y. Jung, S. M. Jung, G. H. Gu, J. S. Suh, *Appl. Phys. Lett.* **89**, 13121, 2006.

[100] A. L. M. Reddy, M. M. Shaijumon, S. R. Gowda, P. M. Ajayan, *NanoLett.* **9**, 1002, 2009.
[101] K. Hata, D. N. Futaba, K. Mizuno, T. Namai, M. Yumura, S. Iijima, *Science* **306**, 1362, 2004.
[102] C. S. Cojoracu, Dissertation, Strasbourg 2003.
[103] R. W. Wood, *Phys. Rev.* **5**, 1, 1897.
[104] C. Spindt, I. Brodie, C. E. Holland, P. R. Schwoebel, in "Vacuum Microelectronics", Ed. W. Zhu, Wiley 2001.
[105] D. S. Chung, S. H. Park, H. W. Lee, J. H. Choi, S. N. Cha, J. W. Kim, J. E. Jang, K. W. Min, S. H. Cho, M. J. Yoon, J. S. Lee, C. K. Lee, J. H. Yoo, Jong-Min Kim, J. E. Jung, *Appl. Phys. Lett*. **80**, 4045, 2002.
[106] V. I. Merkulov, D. H. Lowndes, Y. Y. Wei, G. Eres, and E. Voelkl, *Appl. Phys. Lett*. **76**, 3555, 2000.
[107] K. B. K. Teo, E. Minoux, L. Hudanski, F. Peauger, J. P. Schnell, L. Gangloff, P. Legagneux, D. Dieumegard, G. A. J. Amaratunga, W. I. Milne, *Nature* **437**, 968, 2005.
[108] L. Nilsson, O. Groening, C. Emmenegger, O. Kuettel, E. Schaller, L. Schlapbach, H. Kind, J. M. Bonard, K. Kern, *Appl. Phys. Lett.* **76**, 2071, 2000.
[109] R. H. Fowler, N. L. Nordheim, *Proc. R. S. London* **A 119**, 173, 1928.
[110] I. Brodie, C. Spindt, *J. Appl. Phys.* **47**, 5248, 1976.
[111] A.-J. Guilley, Dissertation, Ecole Polytechnique, Palaiseau, 2009.
[112] S. A. Knaack, J. Eddington, Q. Leonard, F. Cerrina, M. Onellion, *Appl. Phys. Lett.* **84**, 3388, 2004.
[113] M. Nakao, S. Oku, T. Tamakura, K. Yasui, H. Masuda, *Jpn. J. Appl. Phys.* **38**, 1052, 1999.
[114] M. Jung, S. Lee, Y. M. Jhon, S. Mho, J. W. Cho, D. Woo, *Jpn. J. Appl. Phys.* **46**, 4410, 2007.
[115] Y. Kanamori, K. Hane, H. Sai, H. Yugami, *Appl. Phys. Lett.* **78**, 142, 2001.
[116] S. W. Shin, S. G. Lee, J. Lee, C. N. Whang, J. H. Lee, I. H. Choi, T. G. Kim, J. H. Song, *Nanotechnology* **16**, 1392, 2005.
[117] D. Crouse, Y. H. Lo, A. E. Miller, M. Crouse, *Appl. Phys. Lett.* **76**, 49, 2000.
[118] J. Zou, X. Qi, L. Tan, B. J. H. Stadler, *Appl. Phys. Lett.* **89**, 093106, 2006.
[119] H. Asoh, M. Matsuo, M. Yoshihama, S. Ono, *Appl. Phys. Lett.* **83**, 4408, 2003.
[120] L. Menon, K. Bhargava Ram, S. Patibandla, D. Aurongzeb, M. Holtz, J. Yun, V. Kuryatkov, *J. Elechtrochem. Soc.* **151**, 492, 2004.
[121] B. Chapman, Glow Discharge Processes, New York 1980.
[122] O. A. Popov (editor), High density plasma sources, Park Ridge, 1995.
[123] J.-M. Rax, Physique des plasmas, Paris 2005.
[124] J. H. Kim, C. J. Kang, T. H. Ahn, J. T. Moon, *Thin Solid Films* **345**, 124, 1999.
[125] H. Kawata, M. Yasuda, Y. Hirai, *Jpn. J. Appl. Phys.* **47**, 6914, 2008.
[126] K. R. Williams, K. Gupta, M. Wasilik, *J. Microelectrochem. Syst.* **5**, 256, 1993.
[127] K. R. Williams, K. Gupta, M. Wasilik, *J. Microelectrochem. Syst.* **12**, 761, 2003.
[128] E. R. Parker, B. J. Thibeault, M. F. Aimi, M. P. Rao, N. C. MacDonald, *J. Electrochem. Soc.* **152**, C675, 2005.
[129] J. Tao, Y. Chen, A. Malik, L. Wang, X. Zhao, H. Li, Z. Cui, *Microel. Eng.* **78-79**, 147, 2005.
[130] M. Schaepkens, G. S. Oehrlein, J. M. Cook, *J. Vac. Sc. & Tech. B* **18**, 848, 2000.
[131] F. Laermer, A. Schilp, US-patent 5498312, 1996.